Heat Transfer Measurements in Rotating Turbine Blade Cooling Channel Configurations using the Transient Thermochromic Liquid Crystal Technique

A thesis accepted by the Faculty of Aerospace Engineering and Geodesy of the University of Stuttgart in partial fulfilment of the requirements for the degree of Doctor of Engineering Sciences (Dr.-Ing.)

by

Dipl.-Ing. Christian Waidmann

born in Mutlangen

Committee chair:	Prof. Dr.-Ing. Jens von Wolfersdorf
Committee member:	Prof. Dr.-Ing. Stephan Staudacher
Date of defence:	8 October 2020

Institute of Aerospace Thermodynamics
University of Stuttgart
2020

Preface

This thesis resulted from my studies conducted at the Institute of Aerospace Thermodynamics (ITLR), University of Stuttgart, Germany. I would like to thank Prof. Dr.-Ing. Jens von Wolfersdorf, my supervisor and main referee. Without his guidance and untiring dedication this project would not have been possible. Furthermore, I want to thank Prof. Dr.-Ing. Stephan Staudacher for being the co-referee of this thesis and Prof. Dr.- Ing. habil. Bernhard Weigand for the possibility to start my studies at the ITLR.

The designing, constructing, setup and qualification of the new rotating test rig was a group effort. I want to thank the entire RotRig team for their commitment to the project: Rico Poser, who I regard as a personal mentor, for his consultation and readiness to share his vast knowledge; Sven Nieland for the design and assembling of the test rig and his entire assistance in operating and maintaining the rig; Michael Göhring for managing the air supply system during the experiments and also for his CFD-support; Thomas Bertnik and Uli Schwaderer of the electrical workshop, whose help and involvement far exceeded the electronics aspect; and David Gutiérrez de Arcos, the latest addition to our team.

Furthermore, I would like to give thanks to Christian Otto and Dennis Nehring of the mechanical workshop and to Susanne Stegmeier and Jasmina Radoncic of the administration department. Thanks to all colleagues for the excellent work

atmosphere in which groups such as the Frühstücksgruppe or the Fotosafari team can thrive.

My research has received funding from the European Union Seventh Framework Programme (FP7/2007-2013) under grant agreement no. 233799 (ERICKA) and from the joint research program COORETEC-turbo (AG Turbo 2020), supported by the Bundesministerium für Wirtschaft und Energie (BMWi), which is gratefully acknowledged. I also want to thank the project partners MTU Aero Engines and Ansaldo Energia for their contribution.

Finally, I wish to thank my family, especially my parents and parents-in-law for babysitting my kids, which made it possible for me to complete this thesis. I am especially grateful to my wife Simone and my daughters Helen and Hanna for their support, patience and love.

Christian Waidmann, October 2020

Contents

List of Figures **ix**

List of Tables **xiii**

List of Symbols **xv**

Abstract **xxi**

Kurzfassung **xxiii**

1 Introduction **1**
1.1 Motivation 1
1.2 State of the Art 6
1.3 Objective 9
1.4 Outline 10

2 Transient Heat Transfer Measurement **13**
2.1 Theory 13
2.2 Model and Instrumentation 17
2.2.1 Model 17
2.2.2 TLCs 20
2.2.3 Camera 24
2.2.4 Thermocouples 25

2.2.5 Pressure Sensors . . . 27
2.3 Experimental Setup . . . 28
2.3.1 Air Supply System . . . 29
2.3.2 Test Section . . . 30
2.3.3 Measurement Equipment . . . 32
2.4 Heat Transfer Evaluation . . . 36
2.4.1 Gmax Time Detection . . . 36
2.4.2 Fluid Temperature Field Interpolation . . . 39
2.4.3 Data Analysis . . . 40
2.4.4 Data Reduction . . . 43
2.5 Aspects to Consider for Rotating Experiments . . . 46
2.5.1 Mechanical Aspects . . . 47
2.5.2 Observation and Optical Aspects . . . 47
2.5.3 Thermal Aspects . . . 48
2.5.4 Aspects of Data Acquisition and Synchronization . . . 49

3 Test Rig for Rotational Effects 51
3.1 Requirements and Test Parameters . . . 51
3.1.1 Dimensionless Quantities . . . 52
3.1.2 Physical Variables . . . 53
3.2 Design of Test Rig and Facility . . . 55
3.2.1 Test Rig Overview . . . 56
3.2.2 Rotor . . . 57
3.2.3 Test Facility . . . 59
3.2.4 Fluid Temperature Step Change . . . 62
3.2.5 Test Model . . . 65
3.2.6 Optical Access and Lighting . . . 75
3.2.7 Synchronization and Data Management . . . 76
3.3 Experimental Procedure and Evaluation . . . 81
3.3.1 Test Procedure . . . 81
3.3.2 Test Parameter Evaluation . . . 83
3.3.3 Image Processing . . . 90
3.3.4 Verification Tests . . . 92

4 Results and Discussion 97
4.1 Test Parameters . . . 98
4.2 Heat Transfer Distribution . . . 99
4.2.1 Stationary Experiments . . . 99
4.2.2 Rotating Experiments . . . 102
4.2.3 Effects of Rotation . . . 104

4.3 Further Data Reduction 107
4.3.1 Histograms of Normalized Nusselt Number Ratios . . . 107
4.3.2 Line Averaging 109
4.3.3 Segment Averaging 111
4.3.4 Passage Averaging 115

5 Conclusion and Outlook **119**

Bibliography **123**

Appendix

A Uncertainty Analysis **133**

B Similarity Parameters **139**
B.0.1 Conservation Equations 139
B.0.2 Nondimensionalization 141
B.0.3 Dimensionless Numbers 142

List of Figures

1.1 The schematic of a modern gas turbine blade with common cooling techniques [20] 3
1.2 Conceptual view of rotational effects: (a) secondary flow and axial flow distribution in a rotating smooth two-pass channel, (b) effect of inertia, Coriolis and rotational buoyancy on outward and inward flows [20] 5
1.3 Nusselt number ratios over stable and unstable endwalls of channels with various cross-sectional shapes [42] 7

2.1 Temperature profile development for semi-infinite wall with surface convection 15
2.3 TLC color play [33] 20
2.4 A schematic diagram of the cholestric structure [26] 21
2.6 Principle of temperature measurements with type K thermocouples 26
2.9 Test facility for stationary tests [52] 29
2.13 Dynamic viscosity and Reynolds number development for an exemplary experiment (STAT, $Re_{targ} = 20000$) 35
2.14 Exemplary frame of cut (time) and cropped (area) videos 36
2.15 Intensity histories of RGB-channels for one exemplary pixel 37
2.16 TLC indication times 38

2.17 Fluid domain with markers for the inner boundary conditions (TC positions) for fluid temperature field interpolation (exemplary for pressure side, STAT) 39
2.18 Interpolated fluid temperature fields at selected points in time (exemplary for PS, STAT, $Re_{targ} = 20000$) 40
2.19 Results of heat transfer evaluation and data analysis 42
2.20 Evaluation domains, coordinates and illustration of warping method for line averaging, STAT 44
2.21 Line averaged normalized Nusselt numbers (STAT, $Re_{targ} = 20000$) 45
2.22 Segment numeration (STAT) 46
2.23 Segment averaged normalized Nusselt numbers (STAT, $Re_{targ} = 20000$) 46

3.1 Achievable dimensionless quantities for a channel with a hydraulic diameter of $d_h = 0.015\,\mathrm{m}$: (a) 3D-plot for Re, Ro, Bo, (b) 2D-plot for Re, Ro, (c) 2D-plot for Ro, Bo, (d) 2D-plot for Re, Bo 55
3.4 Floor plan and main infrastructure of facility 60
3.5 Schematic diagram of cooling air supply system 60
3.7 Internal routing of heat exchanger pipes 63
3.9 Exemplary fluid temperature step changes for different mass flow rates, measured at the model inlet (T01) 65
3.15 Telemetry measurement chain 70
3.20 Delay measurement between trigger and sync-LED response 78
3.21 Detection of fluid temperature change for synchronization of video and fluid temperature data 78
3.22 Data flow and logging procedure of auxiliary measurement data . . 80
3.23 Video frame of rotating experiment with measurement data overlay 83
3.24 Main control and measuring points of test air 84
3.25 Direct measurements 85
3.26 Derived parameters 87
3.27 Derived dimensionless quantities 89
3.28 Correction of wide angle distortion (exemplary for PS) 92
3.29 Perspex thermocouple positions (ROT-A) 93
3.30 Temperature development at different depths inside the solid . . . 94
3.31 Normalized Nusselt number distribution (Nu/Nu_0) 96
3.32 Segment averaged normalized Nusselt number (Nu/Nu_0) 96

4.1 Dimensionless quantities of measurements 99
4.2 Normalized Nusselt number Nu/Nu_0, $Ro = 0$ 100
4.3 Segment numeration (ROT-B) 101
4.4 Segment averaged normalized Nusselt numbers Nu/Nu_0, $Ro = 0$. 101

4.5 Normalized Nusselt number Nu/Nu_0, $Re_{targ} = 15000$ 103
4.6 Normalized Nusselt number ratio *NNNR*, $Re_{targ} = 15000$ 106
4.7 Histograms of *NNNRs*, $Re_{targ} = 15000$ 108
4.8 Line averaging procedure (ROT-B) 109
4.9 Line averaged normalized Nusselt numbers, $Re_{targ} = 15000$ 110
4.10 Line averaged *NNNR*, $Re_{targ} = 15000$ 111
4.11 Segment averaged normalized Nusselt numbers and *NNNRs*, $Re_{targ} = 15000$ 112
4.12 Segment averaged *NNNRs* vs. rotation number 114
4.13 Passage averaged *NNNRs* 116

A.1 Dimensionless equivalent temperature distribution Θ_{eq} 135
A.2 Relative uncertainty of the heat transfer coefficient s_h/h 136

B.1 Cooling channel under system rotation 140

List of Tables

2.1 STAT model parameters 19

3.1 Ranges of test parameters 54
3.2 ROT-B model parameter 66
3.3 Target parameters 84
3.4 Mean values of measured and derived test parameters 90
3.5 Material properties of Perspex 94
3.6 Test parameters for verification tests 95

4.1 Mean values of dimensionless quantities for $Re_{targ} = 15000$ 102

A.1 Parameters for uncertainty analysis 133

List of Symbols

Latin Characters

Symbol	Description	Unit
a	thermal diffusivity	m^2/s
a	acceleration	m/s^2
A	area	m^2
b	rib width	m
B	blue	-
c	specific heat capacity	$\mathrm{J}/(\mathrm{kg\,K})$
c	speed of sound	m/s
d	diameter	m
D	wall thickness	m
e	rib height	m
E	energy	J
F	force	N
G	green	-
h	heat transfer coefficient	$\mathrm{W}/(\mathrm{m}^2\,\mathrm{K})$
i	transmission ratio	-
k	thermal conductivity	$\mathrm{W}/(\mathrm{m\,K})$
L	length	m
m	mass	kg

Symbol	Description	Unit
$\dot{m}$	mass flow rate	kg/s
n	rotational speed	rpm
n	parameter	-
$\bar{n}$	mean refractive index	-
N	counting parameter	-
p	pressure	Pa
p	rib pitch	m
p	pitch length of liquid crystal molecular director helix	m
P	momentum	kg m/s
R	model radius	m
R	red	-
R	specific gas constant	J/(kg K)
s	stream wise coordinate	m
s	standard deviation	-
T	temperature	K
t	time	s
u	flow velocity	m/s
v	circumferential velocity	m/s
w	distance	m
x	spatial coordinate	m
y	spatial coordinate	m
z	spatial coordinate (depth)	m

Greek Characters

Symbol	Description	Unit
α	model angle	$^\circ$
β	parameter	-
ϕ	displacement angle	$^\circ$
γ	rib angle	$^\circ$
Γ	dimensionless density	-
κ	isentropic exponent	-
λ	wavelength of light	m
μ	dynamic viscosity	Pa s
ν	kinematic viscosity	m^2/s
ν	frequency	Hz
ρ	density	kg/m^3
σ	ultimate tensile strength	Pa
Θ	dimensionless temperature	-
τ	time	s
Ω	angular velocity	rad/s

Subscripts

Symbol	Description
0	initial
0	reference
b	bulk
c	critical
$Coriolis$	Coriolis
$centrif$	centrifugal
end	end
eq	equivalent
exp	exposure
f	fluid
fps	frames per second
ftc	fluid temperature change
$Gmax$	maximum green intensity
h	hydraulic
i	inlet
kin	kinetic
max	maximal
$mean$	mean
min	minimal
nom	nominal
opt	optimal
p	constant pressure
ref	reference
ROT	rotating
$STAT$	stationary (non-rotating)
$targ$	target
TLC	thermochromic liquid crystal
w	wall

Dimensionless Quantities

Symbol	Description	Definition
Bo	Buoyancy number	$Bo = \frac{\Delta\rho}{\rho} Ro^2 \frac{R}{d_h}$
Ec	Eckert number	$Ec = \frac{u^2}{c_p(T_w - T_i)}$
Gr	Grashof number of rotation	$Gr = \frac{\rho_w - \rho_i}{\rho_w} \frac{\Omega^2 R d_h^3}{\nu^2}$
Ma	Mach number	$Ma = \frac{u}{c}$
Nu	Nusselt number	$Nu = \frac{h d_h}{k_f}$
Nu_0	reference Nusselt number [79]	$Nu_0 = 0.023 Re^{0.8} Pr^n$
Pr	Prandtl number	$Pr = \frac{\nu}{a} = \frac{\mu c_p}{k}$
Re	Reynolds number	$Re = \frac{u d_h}{\nu} = \frac{\dot{m} d_h}{A\mu}$
Ro	Rotation number	$Ro = \frac{\Omega d_h}{u}$

Abbreviations

Abbrevation	Description
1D	One Dimensional
2D	Two Dimensional
A/D	Analog/Digital conversion
Bmax	Intensity Peak of Blue Color Channel History
CAD	Comput-Aided Design
CFD	Computational Fluid Dynamics
CNC	Computer Numerical Control
D/A	Digital/Analog conversion
Gmax	Intensity Peak of Green Color Channel History
IR	Infrared
ITLR	Institut für Thermodynamik der Luft- und Raumfahrt
LE	Leading Edge
LED	Light-Emitting Diode
NNNR	Normalized Nusselt Number Ratio
PLC	Programmable Logic Controller
PS	Pressure Side
PXI	PCI eXtensions for Instrumentation
RGB	Red Green Blue color space
Rmax	Intensity Peak of Red Color Channel History
ROI	Region Of Interest
RTD	Resistance Temperature Device
SS	Suction Side
SSA	Sensor Signal Amplifier
TE	Trailing Edge
TLC	Thermochromic Liquid Crystal
TTL	Transistor-Transistor Logic
VRE	Versuchsstand REchner (test rig measurement computer)

Abstract

The turbine blades of modern gas turbine engines are equipped with sophisticated cooling schemes. Cooling air is bled from the compressor and passed through internal convective cooling channels with the aim to keep the blade metal temperatures within safe limits. In an effort to increase overall engine performance and efficiency, turbine inlet temperatures are being steadily increased while simultaneously the cooling air consumption is reduced. A reduction in cooling air mass flow however increases the effects of rotation on the internal flow structures and thus the heat transfer distribution of a rotating cooling channel. These effects are Coriolis forces and rotational buoyancy forces that may increase heat transfer significantly at one surface compared to the non-rotating case, while simultaneously the heat transfer may drastically be reduced at the opposite surface.

For future cooling scheme developments it is vital to understand the influence of these rotational effects on the heat transfer distribution in order to derive resulting temperature distributions inside the turbine blade. A well established measurement technique is the transient thermochromic liquid crystal (TLC) technique that is applied in various investigations of non-rotating cooling channels to evaluate locally resolved heat transfer data. The aim of this thesis is to apply this measurement method for the investigation of rotating cooling channels in order to assess the influence of the rotational effects on the heat transfer distribution.

In order to do so a test rig has been developed that was specifically designed to apply the transient TLC measurement method to rotating cooling channels. Several challenges had to be mastered in the process. First of all, the test

model and all rotating components had to be designed or selected to withstand the specified centrifugal forces. Second, a new co-rotating camera unit had to be developed to allow the TLC signal to be captured during rotation.

The transient measurement method requires the cooling channel to be exposed to a sudden fluid temperature change. This is achieved with a stationary bypass valve unit that allows pre-conditioning of the test model as well as pre-cooling of all cooling air supply lines before the start of the experiment. Cooling air is provided by an air supply system that is based on a liquid nitrogen operated heat exchanger. During the experiment fluid temperature and pressure measurement data are acquired and transmitted to the stationary system with a radio telemetry system.

Finally, a test campaign with a total of 32 experiments could be conducted. Exemplary results of this campaign are discussed. The results are presented as locally resolved distributions of Nusselt number ratios as well as line and area averaged data. Furthermore, for each rotating experiment also a corresponding stationary experiment was conducted. This allowed a direct visualization of the rotational effect on the heat transfer distribution by calculating the local normalized Nusselt number ratio between the rotating and the non-rotating experiment.

Kurzfassung

Die Turbinenschaufeln moderner Gasturbinentriebwerke sind mit anspruchsvollen Kühlsystemen ausgestattet. Die Kühlluft wird aus dem Kompressor abgezogen und durch interne konvektive Kühlkanäle geleitet, mit dem Ziel, die Temperaturen des Schaufelmaterials innerhalb sicherer Grenzen zu halten. Um die Gesamtleistung und den Wirkungsgrad des Triebwerks zu erhöhen, wird die Turbineneintrittstemperatur kontinuierlich erhöht während gleichzeitig der Kühlluftverbrauch reduziert wird. Eine Reduzierung des Kühlluftmassenstroms erhöht jedoch die Auswirkungen der Rotation auf die inneren Strömungsstrukturen und damit die auf die Wärmeübergangsverteilung eines rotierenden Kühlkanals. Diese Effekte sind Coriolis-Kräfte und Rotationsauftriebskräfte, die den Wärmeübergang an einer Oberfläche im Vergleich zum nicht rotierenden Gehäuse deutlich erhöhen können, während gleichzeitig der Wärmeübergang an der gegenüberliegenden Oberfläche drastisch verringert sein kann.

Für zukünftige Kühlsystementwicklungen ist es wichtig, den Einfluss dieser Rotationseffekte auf die Wärmeübergangsverteilung zu verstehen, um daraus resultierenden Temperaturverteilungen innerhalb der Turbinenschaufel ableiten zu können. Eine etablierte Messtechnik ist die transiente thermochromatische Flüssigkristall (TLC) Messtechnik, die in zahlreichen Untersuchungen nichtrotierender Kühlkanäle zur Bestimmung lokal aufgelöster Wärmeübergangsdaten eingesetzt wird. Das Ziel dieser Arbeit war es, diese Messmethode für die Untersuchung von rotierenden Kühlkanälen anzuwenden, um den Einfluss der Rotationseffekte auf die Wärmeübergangsverteilung zu beurteilen.

Hierfür wurde ein Versuchsstand entwickelt, der speziell für die Anwendung der transienten TLC-Messtechnik auf rotierende Kühlkanäle konzipiert wurde.

Dabei galt es, mehrere Herausforderungen zu bewältigen. Zunächst mussten das Versuchsmodell und alle rotierenden Komponenten so ausgelegt oder ausgewählt werden, dass sie den auftretenden Zentrifugalkräften standhalten. Zweitens musste eine neue mitrotierende Kameraeinheit entwickelt werden, damit das TLC-Signal während der Rotation erfasst werden kann.

Für die transiente Messmethode muss der Kühlkanal einer plötzlichen Fluidtemperaturänderung ausgesetzt werden. Dies wird durch eine stationäre Bypassventileinheit erreicht, die eine Klimatisierung des Versuchsmodells sowie eine Vorkühlung aller Kühlluftzufuhrleitungen vor Beginn des Experiments ermöglicht. Die Kühlluft wird durch ein Kaltluftsystem bereitgestellt, das auf einem mit flüssigem Stickstoff betriebenen Wärmetauscher basiert. Während des Experiments werden Temperatur- und Druckmessdaten erfasst und mit einem Funk-Telemetriesystem an das stationäre System übertragen.

Schließlich konnte eine Testkampagne mit insgesamt 32 Experimenten durchgeführt werden. Beispielhafte Ergebnisse dieser Kampagne werden diskutiert. Die Ergebnisse werden als lokal aufgelöste Verteilungen von Nusseltzahlenverhältnissen sowie als linien- und flächengemittelte Daten dargestellt. Darüber hinaus wurde für jedes Rotationsexperiment auch ein entsprechendes nicht-rotierendes Experiment durchgeführt. Dies ermöglichte eine direkte Visualisierung des Rotationseffekts auf die Wärmeübergangsverteilung durch Berechnung der lokalen Verhältnisse der normalisierten Nusseltzahlen zwischen rotierendem und nicht-rotierendem Experiment.

CHAPTER 1

Introduction

1.1 Motivation

In an effort to improve the overall performance of gas turbine engines, the pressure ratio and the turbine inlet temperature have been steadily increased. Modern gas turbine engines operate at pressure ratios of over 40:1 and employ turbine inlet temperatures above 1500 °C. An increase of 100 °F (55.6 K) in turbine inlet temperature can provide a corresponding increase of 8 % to 13 % in output and 2 % to 4 % improvement in simple-cycle efficiency [8]. The turbine inlet temperature of advanced gas turbines are far higher than the softening point of the blade material [22]. The development of superalloys and advanced casting processes to produce single-crystal blades as well as the application of ceramic thermal barrier coatings (TBC) improve the temperature resistance of the turbine blades.

However, present high turbine inlet temperatures are only possible when employing highly sophisticated cooling techniques to reduce the heat load, thus keeping the metal temperature of the turbine blades within safe limits. The airfoils are cooled externally and internally with cooling air that is extracted form the high-pressure compressor. The temperature of this cooling air is in

the order of 600 °C. Since this cooling air bypasses the combustion process, it is partially lost for power conversion in the turbine and therefore constitutes a penalty to the thermal efficiency. Thus, next to the increase of the turbine inlet temperature, the aim of modern gas turbine development is to reduce the cooling air consumption, with the disadvantage that the cooling air temperature itself is steadily increasing with increasing pressure ratios. Further advancements in this regard are therefore only possible with a detailed knowledge of the heat transfer distribution provided by the different applied cooling schemes in order to asses the temperature distribution in the turbine blade. High temperature gradients inside the blade cause mechanical stresses and must be avoided. The blade life may be reduced by half if the blade metal temperature prediction is off by only 50 °F (27.8 K) [22].

Some state of the art turbine blade cooling techniques are illustrated by Han [20], see figure 1.1. External cooling is implemented as film cooling, which directly protects the airfoil against the hot combustion gases. The cooling air is lead though internal passages and then injected into the mainstream through discrete holes or slots. This way a protective film is formed near and downstream of the holes which reduces the heat load into the blade surface.

Internal convective cooling is achieved by passing the cooling air through serpentine passages inside the blade. For excessively high thermal loads, such as the leading edge region, impingement cooling is used. The cooling air is ejected from an array of holes or slots and impinges as high-velocity jets onto the internal heat transfer surface. Jet impingement has a very high capability to increase the local heat transfer. The implementation of this cooling scheme however weakens the structural integrity and can therefore only be applied at regions with a suitable thick cross-section at the respective part of the airfoil.

In the mid chord section rib turbulators are commonly used to augment heat transfer in the multi-pass channels. They disturb the near wall flow as they cause the boundary layer to separate upstream and downstream of the ribs. A reattaching boundary layer at the surface between the ribs increases heat transfer significantly. Furthermore, the ribs enhance turbulent mixing which increases the heat dissipation from the near-surface fluid to the channel core flow. Ribs that are angled with respect to the main flow direction induce secondary flows in the direction of the rib angle, which additionally shape the heat transfer distribution on the surface. Finally, ribs increase the heat transferring area. Ribs mostly disturb only the near-wall flow, so that the rib induced pressure loss is still acceptable and the heat transfer enhancement outweighs this adversary effect.

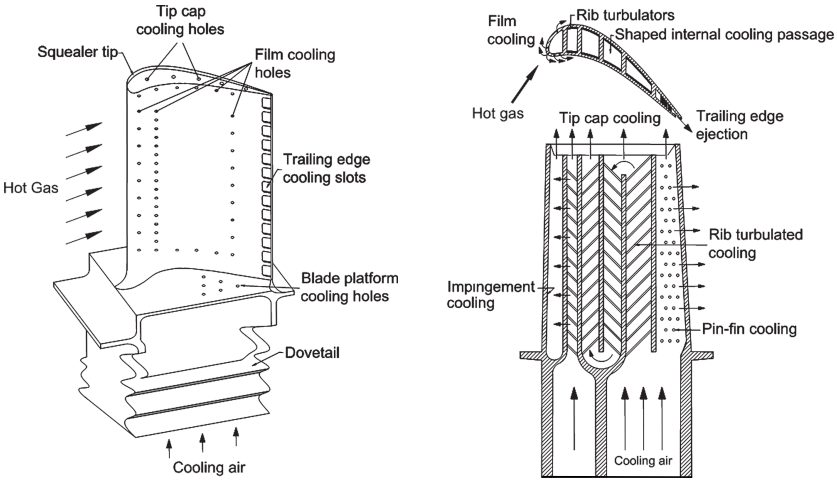

Figure 1.1: The schematic of a modern gas turbine blade with common cooling techniques [20]

An overview of internal cooling techniques is given for example by Weigand et al. [77], Ligrani et al. [35] and Han and Huh [21]. An extensive compilation of experimental research into internal turbine blade cooling is given by Han et al. [22]. Most investigations are conducted using stationary (non-rotating) test channels. In recent years, however, more and more efforts have been made to investigate rotating cooling channels. This is because with a decreasing cooling air mass flow the effects of rotation on the flow structure inside the cooling channels and thus the heat transfer distribution increases. The effects of rotation on the heat transfer distribution can therefore no longer be neglected.

For a rotating cooling channel two additional forces have to be taken into account: the Coriolis force and the centrifugal force. The Coriolis acceleration described in a rotating frame of reference is

$$\vec{a}_{Coriolis} = -2\left(\vec{\Omega} \times \vec{u}\right) \tag{1.1}$$

where $\vec{\Omega}$ is the angular velocity vector describing the rotational speed of the rotating reference frame relative to the inertial frame and $\vec{u}$ is the flow velocity vector relative to the rotating reference frame. The resulting Coriolis force is perpendicular to both the rotational axis and to the flow direction and this

way induces secondary flows which distribute the core flow asymmetrically in the channel. The centrifugal acceleration

$$\vec{a}_{centrif} = -\vec{\Omega} \times \left(\vec{\Omega} \times \vec{R}\right) \tag{1.2}$$

is independent from the flow velocity and only depends on the angular velocity vector $\vec{\Omega}$ and the position vector $\vec{R}$ relative to the rotating reference frame. Centrifugal forces increase with the normal distance from the rotational axis and are always directed radially outwards perpendicular to the rotational axis. The influence of centrifugal acceleration is most pronounced if there are high temperature gradients and thus high density gradients inside the fluid flow. Neighboring fluid parts with differing densities experience different centrifugal forces. This rotational buoyancy effect changes the velocity and temperature profiles compared to a non-rotating case.

The schematic secondary flow and axial flow distribution in a rotating smooth two-pass channel is illustrated in figure 1.2a. The direction of the Coriolis force depends on the flow direction. For a radial outward flow the Coriolis force acts towards the trailing wall (pressure side). Downstream of the 180° bend, where the flow is directed radially inwards, the Coriolis force acts towards the leading wall (suction side). The induced secondary flows illustrated in the cross-sections (see figure 1.2a) show two counter rotating vortices. The orientation of this vortex pair depends on the main flow direction (inward or outward). The net effect of the Coriolis force is to sustain a double helix type of flow structure [44].

The corresponding effect on the axial velocity profile is illustrated in the mid row of figure 1.2b. When only Coriolis forces are considered the colder core flow is shifted towards the trailing wall in the first channel and towards the leading wall in the second channel. Near these surfaces the Coriolis induced secondary flows cause flow unstabilization, meaning turbulence enhancement. These walls are therefore designated *unstable*. Near the opposite walls (leading wall in the first channel and trailing wall in the second channel) the flow is stabilized, meaning that here turbulent fluctuations are reduced with rotation. Therefore, these walls are designated *stable*.

The effect of additional centrifugal buoyancy forces on the velocity profiles is illustrated in the bottom row of figure 1.2b. In the first channel the rotational buoyancy forces enhance the effects of the Coriolis forces, as the centrifugal acceleration on the colder core flow further skews the profile towards the trailing side. In the second channel however the buoyancy forces act against the effects of the Coriolis forces. Here the centrifugal acceleration on the colder core flow

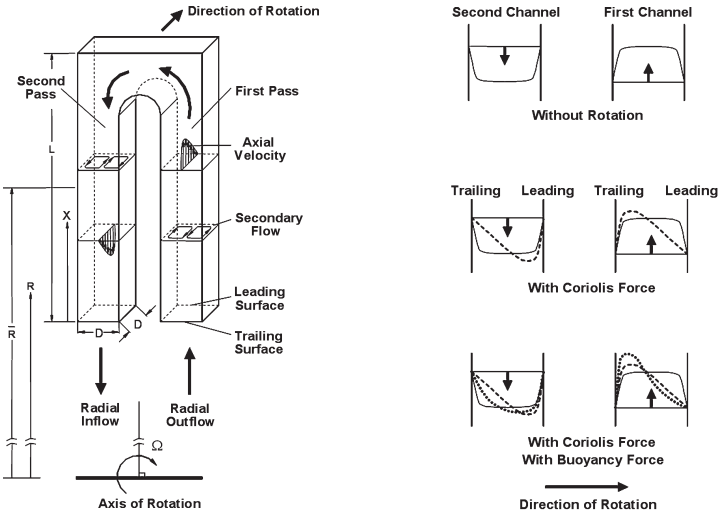

(a) (b)

Figure 1.2: Conceptual view of rotational effects: (a) secondary flow and axial flow distribution in a rotating smooth two-pass channel, (b) effect of inertia, Coriolis and rotational buoyancy on outward and inward flows [20]

reduce the Coriolis induced deformation of the velocity profile resulting in a more uniform flow distribution.

A shift of the velocity profile, as illustrated in figure 1.2b, meaning faster moving colder fluid near one wall (resulting in a thinner boundary layer) and slower moving warmer fluid near the opposite wall (thicker boundary layer), changes of course the local heat transfer for both walls. In the first channel in general an increase in heat transfer can be expected for the trailing wall (PS) and a decrease at the leading wall (SS). In the second channel heat transfer can be expected in general to decrease at the trailing wall (PS) and to increase at the leading wall (SS) compared to the non-rotating case. However, due to the interdependent effects of Coriolis and rotational buoyancy the results depend on the combination of rotational speed and fluid density ratio (or temperature ratio between wall and cooling fluid, respectively). Additionally, if the cooling channel is equipped with angled rib turbulators the flow is also strongly influenced or even dominated by rib induced secondary flows. Finally, flow separation and reattachment caused by the 180° bend also shape the flow

structure and heat transfer distribution in the second channel downstream of the bend. Investigations of the flow field inside rotating cooling channels have been performed using particle image velocimetry (PIV), for example [7, 12, 15, 57] and using laser doppler velocimetry (LDV), for example [11, 23, 38–40, 62].

1.2 State of the Art

Test rigs for the experimental investigation of rotational effects on the heat transfer in cooling channels exist in various research facilities. The design philosophies and principles in designing a rotating rig, together with the identification and description of the relevant dimensionless quantities, are given by Davenport [13] and Morris [45]. Rowbury et al. [58] give some short descriptions of a few rotating rigs used in a collaborative research program (industry and academia). Recent rotating test rig setups are presented by Mathison and Dunn [43], Pagnacco et al. [47], and Waidmann et al. [75]. Overviews of achievable test parameters for different international studies regarding heat transfer in rotating cooling channels are given by Chang et al. [10] and Ligrani [36].

In the 1990s extensive and systematic investigations have been conducted by Wagner et al. [71–73] and Johnson et al. [29, 30]. They used a serpentine four-pass test channel with a quadratic cross-section. The channel comprises several insulated copper segments which can be heated individually. By measuring the mean temperature of the copper segments using thermocouples, mean heat transfer data for each copper segment can be evaluated. A similar method was also applied by Al-Hadhrami and Han [2], Han and Zhang [18], and Han et al. [19].

Liou et al. [41] compared the mean Nusselt number ratios over stable and unstable endwalls of different investigations with various cross-sectional shapes (see figure 1.3). At the unstable walls heat transfer can increase by more than 100 % with increasing rotation numbers ($Ro = \frac{\Omega d_h}{u}$) compared to the non-rotating case. Whereas at stable walls the heat transfer can decrease to minimum values as low as 40 % or even lower, before the values in general tend to increase again with increasing rotation numbers.

For future cooling scheme developments the evaluation of mean heat transfer data over complete passage walls is no longer sufficient. With regard to the strong influences of the rotational effects it becomes more and more important to understand the change in heat transfer distribution with rotation, i.e. spatially resolved heat transfer data are required. This knowledge would for example

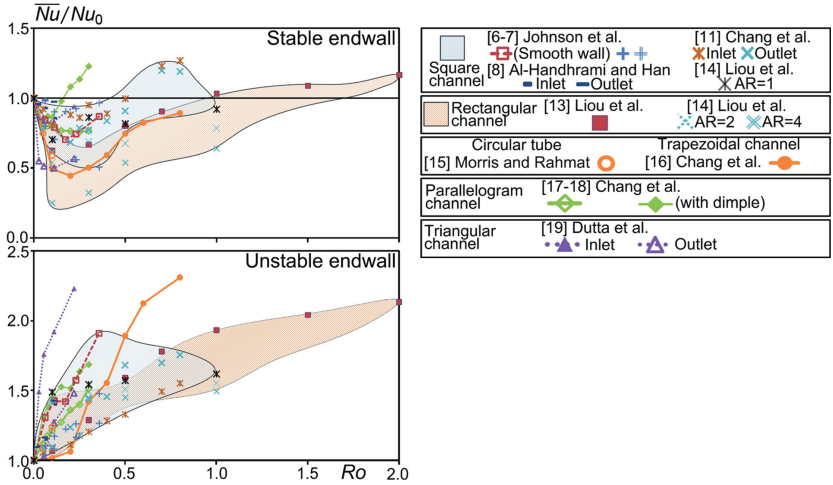

Figure 1.3: Nusselt number ratios over stable and unstable endwalls of channels with various cross-sectional shapes [42]

allow the development of cooling features to address local hotspots, which cannot be detected with a globally evaluated heat transfer information.

One possible measurement method to obtain heat transfer distributions is the napthalene sublimation technique, which uses the analogy between heat and mass transfer. With this analogy the local sublimation rate of naphthalene from the wall into the fluid can be evaluated for the local Sherwood number which can then be translated into local Nusselt numbers. This method was applied for the investigation of rotating channels, for example by Acharya et al. [1], Eliades et al. [16], Kloss [31], Rathjen et al. [55], and Rathjen [56]. The main advantage of this method is that optical access to the test section is not required during the experiment. However, the effects of rotational buoyancy due to density differences in the fluid cannot be captured, since differences in naphthalene concentrations rather than differences in temperature are the driving factor for the transport processes in this method.

Another measurement method is infrared (IR) thermography to obtain locally resolved wall temperatures. The required heat flux for this method is generated for example by thin electrical heater foils that are adapted to the heat transfer surface. The local Nusselt number can then be evaluated from the measured wall and fluid bulk temperatures in combination with an energy balance that

also accounts for all relevant heat losses in this steady-state measurement method. Gallo et al. [17] applied this method to investigate the bend region of a rotating two-pass square channel. They used water as cooling fluid and a stationary IR camera that was synchronized with the rotational speed. Liou et al. [42] used an IR camera that was rotating with the test model, a two-pass parallelogram ribbed channel that was forged from two 0.1 mm thick stainless steel foils. This method requires optical access to the test model where any possible windows need to be transmissive for IR. Furthermore, due to the requirement of a electrically heated wall, this method is particularly suitable for flat or slightly curved test surfaces and less for complex geometries.

Locally resolved wall temperatures can also be obtained using thermochromic liquid crystals (TLCs) that are applied onto the investigated heat transfer surface. Taslim et al. [68] used this method for the investigation of a rotating ribbed square channel. The channel consisted of three clear Perspex walls to allow optical access to the fourth wall made of pinewood. To this wall electrical foil heaters and a TLC foil were mounted. After reaching steady-state conditions pictures of the TLCs were taken using a co-rotating programmable camera.

TLCs can also be used as surface temperature sensors in a transient measurement method, where the measured wall temperature response after an imposed sudden change of the fluid temperature is used to evaluate local heat transfer data, compare [14, 26, 27, 53]. As here electrical heater elements are not required, complex cooling channel geometries can be investigated. For this the TLCs are directly applied to the heat transfer surfaces using an airbrush system. Blair et al. [6] applied this method to investigate the rotating four-pass channel presented by Wagner et al. [71]. They captured the TLC color play using a stationary video camera and a strobe flash illumination that was synchronized with the rotational speed. The pre-test procedure consisted of heating the air flowing through the coolant passages until the acrylic test model reached isothermal conditions. The experiment was then started by switching off the power to the coolant power inlet heater. This way a fluid temperature change was generated where the fluid is colder than the test channel walls in order to replicate the correct sense of the buoyancy forces.

Pearce et al. [50] investigated a ribbed three-pass channel with a rectangular cross-section and used the rotating rig described by Davenport [13]. They used CCD cameras and LED lighting that were embedded within the perspex test model. Pagnacco et al. [47–49] investigated a three-pass cooling channel where the fist two passages are equipped with rib turbulators and the third passage with cylindrical pin fins. They used a heat exchanger operated with

liquid nitrogen to generate cooling air with temperatures as low as −80 °C. Furthermore, they applied a mixture of two types of TLCs with different indication temperatures to guarantee that in all three passages at least one TLC indication occurred within a suitable time frame.

Mathison and Dunn [43] presented a new rotating test facility that is capable of both, the constant wall temperature method using individually heated copper panels, and the transient TLC method. For the latter co-rotating commercial action cameras[1] are used to capture the TLC color play. A similar approach with adapted commercial action cameras is made by Waidmann et al. [74]. The corresponding rotating test rig and its application is presented in this thesis.

1.3 Objective

The transient TLC method is a well established measurement method for the evaluation of local heat transfer distributions and has been applied for the investigation of non-rotating cooling channels in various studies. TLCs are easily applicable to curved surfaces which allows the investigation of complex and realistic cooling channel geometries. The aim of this thesis is to transfer and adapt this method for the investigation of rotating cooling channels at engine representative operating conditions characterized by Coriolis and buoyancy force effects on the cooling air flow.

A new rotating test rig was designed with a special focus on the requirements of the transient TLC heat transfer measurement method. Several challenges had to be overcome. First of all, the limited space makes it necessary to reduce the size of the rotational models compared to the stationary models. The limits are set by the specified maximum rotor diameter and the employed model housing. The housing protects the model from external airstreams during rotation and additionally allows the model to be pressurized in order to reach high operating pressures. This is desirable, as high operating pressures promote the investigated rotational effects, so that the required test parameters can be reached within the rotational speed limitations of the rig. In contrast to this, for stationary experiments mostly operating pressures near 1 bar are chosen to minimize possible leakage.

While at a stationary experiment cameras and lighting can be freely positioned and adapted till interfering reflections are eliminated, the co-rotating cameras and lighting LEDs of a rotating experiment must be positioned very near to

[1] from GoPro type Hero4 Black

the model within the model housing. Later adjustments of camera and lighting positions are very difficult or nearly impossible. The camera position requires the use of a wide angle lens in order to capture the complete test channel, which results in a prominent wide angle distortion in the video footage. Additional post-processing procedures are required to correct this distortion.

In a stationary experiment the temperature and pressure data can be obtained using standard sensors and standard data acquisition devices. Furthermore, the instrumentation of the model is much easier and also allows later adjustments if needed. In contrast, for a rotating experiment special robust sensors and a telemetry system to transmit the measurement data to the stationary system are required. All rotating devices must be selected to withstand the specified centrifugal forces. All cables must be routed and equipped with strain relief.

Finally, the required fluid temperature step that is needed for this measurement method is much simpler to realize for a stationary experiment. Here, even heated air can be used as fluid, as in a stationary experiment the buoyancy effects are negligible. The direction of the heat transfer would then be from hot fluid to cold wall in contrast to real engine conditions. The fluid temperature change can be generated by switching on an electrical heater or by using a pre-heated bypass valve system that switches the heated air instantly into the test model. For a rotating experiment the direction of heat transfer needs to be from hot wall to cold fluid to simulate real engine conditions. Only in this way the correct working direction of the buoyancy forces can be replicated. Therefore a rotating experiment needs cooled air and a pre-conditioning of the air supply passages.

1.4 Outline

In chapter 2 the fundamentals of the transient measurement method are described. All required sensors are presented, with a special focus on the properties of thermochromic liquid crystals that are used to determine surface temperatures. Subsequently, the measuring principle and the experimental procedure are presented, first for a non-rotating model and experiment. After that the post processing and evaluation procedure of the transient heat transfer experiment is explained, presenting exemplary intermediate results for each evaluation step. The chapter closes with a summary of the aspects that need to be considered when applying the transient TLC measurement method in a rotating experiment.

In chapter 3 the relevant dimensionless quantities for a rotating cooling channel are introduced. The requirements and limitations of the rig are defined based on the desired ranges of these dimensionless quantities that should be achievable with the rotating rig. Subsequently, the design of the rig and the corresponding infrastructure such as the cooling air supply system and safety installations are presented. After that the principle for generating the fluid temperature step change is explained. Then the geometry, instrumentation and housing of the test model, as well as the telemetry system are presented. After the introduction of the co-rotating camera unit, the procedure to synchronize the video footage with the telemetry data is described in detail. Subsequently, the test procedure for a typical rotating experiment is explained. After that additional post-precessing and evaluation steps such as wide angle distortion correction or the evaluation of the dimensionless quantities (rotation number and buoyancy number) are presented. Finally, the results of two verification tests are discussed. The first test verified that an assumption underlying the measurement method had been fulfilled, and the second test regarded repeatability.

Chapter 4 contains exemplary heat transfer results from a measurement campaign with a total of 32 evaluated experiments with varying Reynolds numbers and rotation numbers. The influence of rotation on the heat transfer distribution can be clearly seen in these results. Presented are locally resolved distributions of Nusselt number ratios, as well as line averaged, segment averaged and finally passage averaged data. It is shown that depending on the orientation of the heat transfer surface with respect to flow direction and rotational axis, heat transfer can be significantly enhanced or diminished with rotation.

CHAPTER 2

Transient Heat Transfer Measurement

In this chapter the theory of the transient heat transfer measurement method using Thermochromic Liquid Crystals is explained briefly. Then the investigated test model and the different measurement sensors and their applications are introduced. After that the test facility for non-rotating experiments is presented. Subsequently, the evaluation procedure is explained in detail and exemplary intermediate results for each evaluation step are given. Finally, the aspects that have to be considered to transfer the presented measurement method to a rotating system are discussed.

2.1 Theory

The aim of the presented transient measurement method is to evaluate the heat transfer distribution on a heat transfer surface, e.g. to determine the 2D-Nusselt number distribution on cooling channel walls. The principle of this method is to expose the surface to a defined fluid reference temperature and to measure the surface temperature response. With these measurements, together with the known material properties of the wall, the heat transfer coefficient h can be determined locally.

The evaluation is based on Fourier's transient heat conduction equation for a solid without heat sources or heat sinks [46].

$$\nabla \cdot k \nabla T = \rho c \frac{\partial T}{\partial t} \tag{2.1}$$

where T is the temperature, k the heat conductivity, ρ the density and c the specific heat capacity of the solid per unit mass. A representation of this equation in Cartesian coordinates is

$$\frac{\partial}{\partial x}\left(k\frac{\partial T}{\partial x}\right) + \frac{\partial}{\partial y}\left(k\frac{\partial T}{\partial y}\right) + \frac{\partial}{\partial z}\left(k\frac{\partial T}{\partial z}\right) = \rho c \frac{\partial T}{\partial t} \tag{2.2}$$

If the heat conduction is only *one-dimensional* (in z-direction) and the heat conductivity k is constant, equation (2.2) reduces to

$$\frac{\partial^2 T}{\partial z^2} = \frac{1}{a}\frac{\partial T}{\partial t} \tag{2.3}$$

where the material properties of the solid are combined in the thermal diffusivity parameter

$$a = \frac{k}{\rho c} \tag{2.4}$$

The solution of the partial differential equation (2.3) describes the temperature variation in both time t and spatial coordinate z. For some particular problems analytical solutions can be found.

One example is the idealized case of the semi-infinite wall with surface convection. A semi-infinite wall is characterized by a single surface with the solid extending to infinity in all but one direction. Considering uniform conditions at the surface, heat conduction can be assumed to occur only in one dimension. In order to solve for $T(z,t)$ we have to define the initial and boundary conditions. We are interested in the development of the temperature distribution inside an initially isothermal wall after a sudden change of the surface condition at $t = 0$. The initial condition is therefore

$$T(z,0) = T_0 \tag{2.5}$$

where T_0 is the start temperature. In a depth z far away from the surface the temperature remains unchanged, independent from temperature changes at the surface. The interior boundary condition is therefore

$$T(z \to \infty, t) = T_0 \tag{2.6}$$

A sudden exposure of the surface ($z = 0$) to a fluid with the reference temperature T_{ref} yields the exterior boundary condition

$$-k\frac{\partial T}{\partial z}\bigg|_{z=0} = h\left[T_{ref} - T\left(0,t\right)\right] \tag{2.7}$$

The left hand side of this equation describes the heat conduction from the surface into the solid, according to Fourier's law. The right hand side represents the heat transfer from fluid to the wall, which depends on the heat transfer coefficient h in accordance with Newton's law of cooling.

A solution for these conditions is given in Incropera et al. [24]

$$\frac{T(z,t) - T_0}{T_{ref} - T_0} = \operatorname{erfc}\left(\frac{z}{2\sqrt{at}}\right) - \left[\exp\left(\frac{hz}{k} + \frac{h^2 at}{k^2}\right)\right]\left[\operatorname{erfc}\left(\frac{z}{2\sqrt{at}} + \frac{h\sqrt{at}}{k}\right)\right] \tag{2.8}$$

The schematic temperature profile development for this case is illustrated in figure 2.1.

In the presented heat transfer measurement method only the surface temperature (at $z = 0$) is evaluated. With $T_w(t) = T(0,t)$ equation (2.8) simplifies to

$$\frac{T_w(t) - T_0}{T_{ref} - T_0} = 1 - \exp\left(h^2\frac{t}{\rho ck}\right)\operatorname{erfc}\left(h\sqrt{\frac{t}{\rho ck}}\right) \tag{2.9}$$

This equation describes the surface temperature development after an ideal fluid temperature step change as given by $(T_{ref} - T_0)$. However, in a real experiment such an ideal instant change cannot be achieved. Due to heat losses or gains

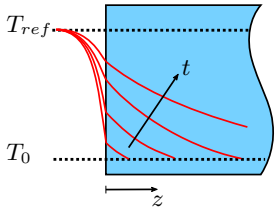

Figure 2.1: Temperature profile development for semi-infinite wall with surface convection

the temperature development is smoothed. Using Duhamel's superposition principle [66], the real fluid temperature history can be approximated by a series of ideal temperature steps

$$T_w(t) - T_0 = \sum_{j=1}^{N} \left[1 - \exp\left(h^2 \frac{t - \tau_j}{\rho c k} \right) \operatorname{erfc}\left(h \sqrt{\frac{t - \tau_j}{\rho c k}} \right) \right] \cdot \Delta T_{f(j,j-1)} \tag{2.10}$$

where $T_f(\tau_j)$ is the reference fluid temperature at discrete points in time. This equation can numerically be solved for the heat transfer coefficient h if one combination of the surface temperature $T_w(t^*)$ and the corresponding time t^*, as well as the fluid temperature history up to this point in time are known. For every x,y-position on the surface, equation (2.10) has to be evaluated separately to obtain the 2D-distribution of the heat transfer coefficients $h(x,y)$.

Several assumptions have to be fulfilled to apply equation (2.10) for the evaluation of experimental tests:

- the heat transfer coefficient h is constant in time
- the heat conduction is one-dimensional
- the test model wall is semi-infinite
- the material properties of the test model are constant

This gives rise to a number of limitations and requirements:

- potential variations of the heat transfer coefficient h during a transient experiment cannot be measured
- possible effects of lateral heat conduction cannot be detected. Therefore, increased measurement uncertainties have to be expected at regions with a high temperature gradient with respect to the model surface (e.g. on or in the vicinity of rib-turbulators)
- the test model wall has to be thick enough to be considered semi-infinite. A relation between the maximum test duration t_{max}, thermal diffusivity a and wall thickness D, for which the semi-infinite wall assumption for a transient TLC experiment is valid, is given in [69]

$$D > \sqrt{\frac{a\, t_{max}}{0.25}} \tag{2.11}$$

- heat transfer cannot be evaluated on small-scale structures on the heat transfer surface like rib-turbulators, as in this case both assumptions (1D-heat conduction and semi-infinite wall) are not fulfilled

2.2 Model and Instrumentation

The test model is instrumented with several sensors. In order to apply equation (2.10) for the heat transfer evaluation, the surface temperature needs to be measured at least at one point in time. For this, Thermochromic Liquid Crystals (TLC) are used. Their color play is captured with a digital video camera to obtain the TLC indication times. Additionally the measurement of the fluid temperature history is required. This is achieved by several thermocouples along the test channel to obtain location- and time-resolved fluid temperature data. Furthermore, the test model is equipped with pressure tabs to measure time-resolved fluid pressure data that are needed to determine the experimental boundary conditions and relevant test parameters.

2.2.1 Model

Geometry

The investigated test model (STAT) is a generic low-pressure turbine blade forward cooling scheme. The inlet passage (pass 1) represents a leading edge cooling channel with a radial outward flow and has a trapezoidal cross-section. A 180° bend connects pass 1 with the outlet passage (pass 2). This passage has a rectangular cross-section and a radial inward flow. The total length of each passage is 400 mm. Figure 2.2a shows the CAD model of the fluid domain.

Pressure and suction sidewalls are equipped with 60° skewed ribs. In pass 1 there are 18 ribs on the suction sidewall and 17 ribs on the pressure sidewall. Pass 2 has 15 ribs on the suction sidewall and 14 ribs on the pressure sidewall. The rib cross-section is rectangular and the rib sidewalls are perpendicular to the channel walls. The rib arrangement is staggered with an offset of $0.5\,p$ (rib pitch) between the ribs of the suction side and pressure side. A listing of the main model parameters is given in table 2.1

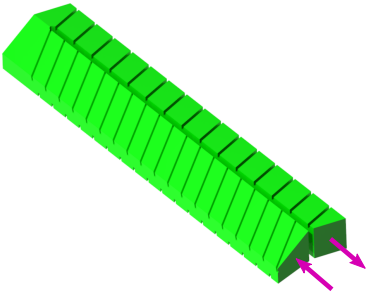

(a)

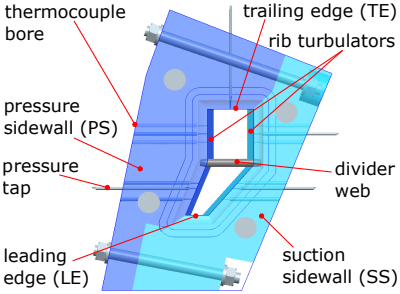

(b)

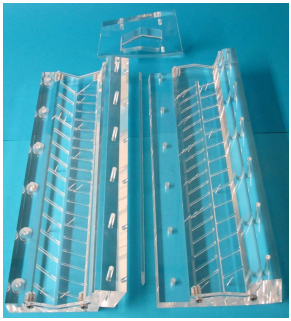

(c)

(d)

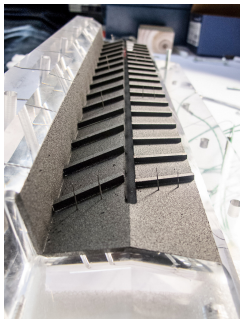

(e)

(f)

Figure 2.2: STAT model for stationary experiments: (a) CAD model of fluid domain, (b) CAD design based on two Perspex half shells (top view), (c) Perspex model parts, (d) assembled model on base block, (e) coated pressure sidewall, (f) coated suction sidewall

Table 2.1: STAT model parameters

	pass 1	pass 2
shape of cross-section	trapezoidal	rectangular
hydraulic diameter d_h (mm)	19.75	26.19
length of passage L (mm)	400	400
rib angle γ	60°	60°
rib pitch p / hydraulic diameter d_h	1.0	1.0
rib height e / hydraulic diameter d_h	0.1333	0.1333
rib width b / hydraulic diameter d_h	0.1	0.1
rib offset between SS and PS / rib pitch p	0.5	0.5
number of SS ribs	19	15
number of PS ribs	18	14

Properties

The model is made of Perspex and consists of four main parts: the ribbed pressure sidewall, the ribbed suction sidewall, the divider web, and the tip wall, as shown in figure 2.2c. Perspex has very good optical properties and allows the observation of the inner channel wall surfaces through the Perspex solid. Furthermore, the thermal diffusivity of Perspex is comparatively low, making it suitable for transient heat transfer experiments. The walls have a minimum thickness of $D = 20\,\text{mm}$. Considering a maximum test duration of $t_{max} = 90\,\text{s}$ and the material properties of Perspex[1]the walls can safely be regarded as semi-infinite, according to equation (2.11).

The robust model design allows a maximum inlet pressure of 2.4 bar (absolute pressure). The design comprises bolts to connect the two Perspex half shells. Small areas of the leading edge are obstructed by these bolts. The contact surfaces of the two Perspex sidewalls are designed to minimize interference for the heat conduction in the wall. The tip wall is inserted at the top of the model and screwed to the half shells. A temperature-resistant adhesive bonding compound[2] is applied to all contact surfaces of all model parts to seal the complete model.

The model is mounted on top of a polyamid[3] base block, which connects the model to the air supply system. Figure 2.2d shows the assembled model mounted on the base block.

[1] $k_{\text{Perspex}} = 0.19\,\text{W/(m K)}$, $\rho_{\text{Perspex}} = 1190\,\text{kg/m}^3$, $c_{\text{Perspex}} = 1470\,\text{J/(kg K)}$
[2] from Hylomar Ltd. type Hylomar M
[3] from KTK Kunststofftechnik Vertriebs GmbH type PA6G natur

2.2.2 TLCs

Fundamentals

Thermochromic liquid crystals (TLCs) are optically active mixtures of organic chemicals. Their optical properties are temperature-dependent. TLCs can therefore be used as temperature sensors and allow the thermal mapping of surfaces. In this thesis they are applied on heat transfer surfaces to indicate the wall temperature of turbine blade cooling channel models during transient heat transfer experiments.

TLCs show colors by selectively reflecting incident white light. They initially appear colorless (or black when coated on a black surface). At a given temperature they start to reflect red light. With increasing temperatures the reflected light passes through the visible spectrum (red, orange, yellow, green, blue) before the TLCs turn colorless (black) again, as shown in figure 2.3. The color changes are reversible. Therefore, cooling back down shows a reversed sequence of the color play. The secret of these properties stems from the chiral (twisted) molecular structure within the liquid crystal. The liquid crystalline (or mesomorphic) state is intermediate between that of a crystalline solid and an isotropic liquid [32]. The optically-active temperature range corresponds to the transition between the solid and liquid state [26].

The TLCs used in this thesis are classified as cholestric or chiral nematic liquid crystals. In the optically-active phase the molecules are arranged in planes. Inside these planes the long and thin (cigar-shaped) molecules align themselves in a distinct direction, denoted as the molecular director, as shown in figure 2.4 [26]. Between the individual layers the director is rotated by a

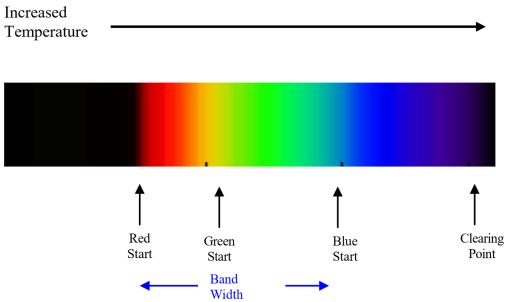

Figure 2.3: TLC color play [33]

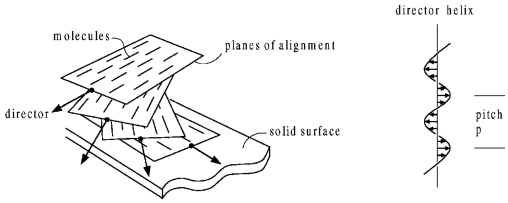

Figure 2.4: A schematic diagram of the cholestric structure [26]

distinct angle (called displacement angle) with regard to the planar normal direction. As shown on the right hand side of figure 2.4 the molecular director traces out a helix in space. The longitudinal distance between two layers, between which the director makes one complete 360° revolution, is called the pitch length p. When the pitch length is in the order of the wavelength of visible light, the color play can be observed. Applied as thin films, the TLCs selectively reflect bright, almost pure colors. These characteristic iridescent colors can be explained by Bragg scattering effects (as observed in crystalline solids with shorter wavelength X-Rays) [32]. The wavelength λ_0 of the reflected light can be approximately described by the Bragg diffraction equation

$$\lambda_0 = p\,\bar{n}\sin\phi \tag{2.12}$$

where p is the cholestric helical pitch length, $\bar{n}$ the mean refractive index and ϕ the angle of incidence normal to the surface. There are two main effects of how a change in temperature influences the pitch length. The first one tends to increase the distance between adjacent molecular layers with rising temperatures due to an increase of the thermal motion of the molecules. This would mean an increase of the pitch length and thus a shift of the reflected light towards longer wavelengths. However, the second effect counteracts against the first one by increasing the displacement angle between adjacent layers. This decreases the pitch length, as now fewer layers are needed for a full 360° revolution of the molecular director. Since the second effect usually dominates over the first one, the reflected light is in general shifted towards shorter wavelengths with increasing temperatures. The pitch lengths and temperature dependencies are varying with different cholestric compounds. Therefore it is possible to chose from a wide variety of liquid crystal formulas with suitable properties for the respective measurement problem. The red start temperatures range from $-30\,^{\circ}\mathrm{C}$ to $120\,^{\circ}\mathrm{C}$, while the color play bandwidths (temperature difference between red start and blue start) range from 0.5 K to 20 K [63].

In addition to temperature sensitivity, the optical properties of TLCs can also be influenced by pressure, shear stress and electric and magnetic fields. Furthermore TLCs are very susceptible to degradation especially by UV light and certain organic chemicals, e.g. greases and common solvents. An effective and common way to protect the TLCs is microencapsulation, where tiny droplets of liquid crystal are surrounded with a continuous polymer coating. The resulting microcapsules have diameters between a few microns and a few millimeters, depending on the manufacturing process. Microencapuslation isolates the TLCs from the atmosphere and this way suppresses the influence from shear stress and pressure effects. Furthermore the handling is improved as in this form the TLCs can be used as pigments in water-based coating formulations and applied onto surfaces using an airbrush. Despite the protective encapsulation TLCs can easily be damaged. For example if they are exposed to temperatures far away from their indication temperature or by exposure to UV light. When used as temperature sensors hysteresis [3] and aging effects [34] also have to be considered.

Application

TLCs are widely used in transient heat transfer experiments, see e.g. Chambers et al. [9], Talib et al. [67], Ekkad and Han [14], Poser and von Wolfersdorf [53]. In these kinds of experiments the delay between an induced fluid temperature change and the resulting wall temperature change, indicated by the TLC color play, is measured. It is therefore important to assess, how fast the TLCs are reacting to a temperature change. Ireland and Jones [25] determined the response time of encapsulated TLCs to be in the order of 3 ms. Considering the frame rates of common video systems that are used to capture the TLC color play, the response times can be neglected.

In this thesis microencapsulated narrow band TLCs with capsule diameters in the range of 10 µm to 15 µm and a bandwidth of 1 K are used. They are applied to the inner test channel walls with an airbrush system providing a total TLC layer thickness of approximately 40 µm to 100 µm. On top of the TLCs several layers of black contrast paint are applied. This allows the observation of the TLC colorplay from outside through the Perspex wall. Figures 2.2e and 2.2f show the inner channel walls of the test model coated with TLCs[4] and black contrast paint[5].

[4] from LCR Hallcrest Ltd. type SPNR38C01W250G
[5] from LCR Hallcrest Ltd. type SPBB500G

Calibration

The manufacturer provides calibration certificates for every batch of delivered TLC type, stating the temperatures for: visual start, red start, green start and blue start. However, an independent calibration of the complete measurement chain is advised, as the calibration result may also strongly depend on the lighting conditions and camera system in use. Furthermore, for the transient measurement method we need a distinct, easily identifiable feature inside the measured temporal TLC signal that can be used as calibration point. For this, the maximum intensity of the green RGB color channel (G_{max}) was selected. The calibration process for the TLCs is described in detail by Poser [54].

The TLCs are coated on top of black contrast paint onto a copper plate, see figure 2.5a. The plate is well insulated in all directions and covered with a Perspex plate to ensure optical access to the coated surface. With the coolant flow from a cryostatic temperature controller at one end and a heated flow at the other end, a linear temperature profile can be achieved along the plate. Ten thermocouples type T are positioned equidistantly along the centerline directly below the surface of the plate to measure the temperature profile.

The copper plate is tempered for several hours to ensure steady-state conditions. For the calibration, the same camera type, camera settings and lighting conditions should be used as in the actual experiments. A video with a duration of several seconds is captured of the TLC color gradient. Simultaneously the thermocouple data are recorded. In post processing the video frames are averaged, so that a single mean image is obtained. From this image a region of

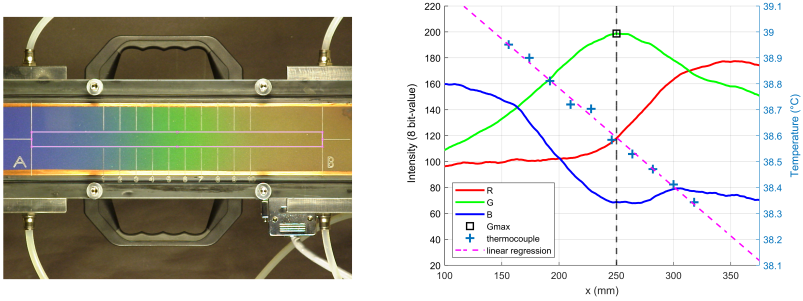

(a) Calibration plate with TLC color gradient and ROI indicator

(b) RGB intensity profiles and temperature profile

Figure 2.5: TLC calibration

interest (ROI) along the center line is selected as shown in figure 2.5a. For each of the RGB color channels the intensity values are then line-averaged lateral to the main axis to obtain RGB intensity profiles along the main axis. The thermocouple data are also time-averaged. Using a linear regression analysis the temperature profile along the main axis can be determined. RGB intensity profiles together with the temperature profile are shown in figure 2.5b.

For the actual evaluation the in-house tool ProTeIn[6] by Poser [54] is used. ProTeIn evaluates the T_{Rmax}, T_{Gmax} and T_{Bmax} temperatures. Additionally, it provides information on the uncertainties of the evaluated color vs. temperature mappings. The standard deviations of stationary TLC calibrations were evaluated between 0.05 K to 0.10 K for frequently used narrow band TLCs with a temperature bandwidth of 1 K. In this thesis only the Gmax temperature was used for the heat transfer evaluation. In the following, it is referred to as the TLC indication temperature $T_{TLC} = T_{Gmax}$.

2.2.3 Camera

The TLC colorplay is captured via a digital color video camera[7] providing a progressive scan resolution of 1024 x 768 pixels at a frame rate of $\nu_{fps} = 15$ fps. This camera utilizes a 1/3-inch-type CCD sensor. In order to minimize optical distortion, a suitable combination of telephoto lens[8] and long operating distance of 3 m to 4 m was selected.

The camera is directly connected to a personal computer via a FireWire 400 interface link. Configuration of the camera settings and video recording are performed with a program written in LabVIEW[9]. The uncompressed video data is directly stored on the local hard drive.

Two fluorescent lamps[10] are used for illumination. Since they are operated with alternating current, their lighting intensity fluctuates with a frequency of 100 Hz (twice the power line frequency). To avoid flickering in the video recording, the exposure time was set to $t_{exp} = 0.06$ s. This is the highest possible integer multiple of the period duration of the lighting fluctuations that fits inside the maximum possible exposure time of $t_{\exp,max} = \nu_{fps}^{-1} = 0.066$ s. Thus, the accumulated lighting intensity remains constant between each video frame.

[6] Program for Temporal Indication Analysis
[7] from Sony type DFW-X710
[8] from Fujinon type HF35HA-1B (1:1.6/35mm)
[9] from National Instruments incl. NI-IMAQdx driver software package
[10] from Osram type Lumilux De Luxe Warm White (930)

Taking into account the fixed lighting settings and the fixed exposure time, the correct video exposure can finally be set via the lens aperture. This setting was determined iteratively with preliminary tests. Best results are achieved when the 8 bit-range of the RGB-channels are covered as well as possible. However, overexposure (over saturation) has to be avoided by all means, i.e. all values should be well below 255. Overexposure would directly lead to measurement errors for the indication time in a transient TLC experiment.

2.2.4 Thermocouples

Fundamentals and Properties

Thermocouples consist of two different electrical conductors that are connected at one end. They produce a temperature-dependent voltage as a result of the thermoelectric effect and can therefore be used as temperature sensors. Type K thermocouples are based on a NiCr/Ni material combination and are the most common type. In this thesis type K thermocouples[11] with a mantle are used. The two conductors are protected inside a sheath with an outer diameter of only 0.5 mm. At the tip the outer diameter is reduced to 0.25 mm on a length of 3 mm. These very thin thermocouples have a fast response time and thus allow a fast tracking of the measured temperature as required for the transient heat transfer experiment.

Type K thermocouples have a sensitivity of approximately 40 µV/K. For the acquisition of the thermoelectric voltages three multiplex scanners[12], each with a 16-channel multiplexer card[13], are used. The data are acquired with a sample rate of approximately 2 samples/s. Because of the multiplexers sequential data acquisition, the temperature data are resampled in post processing onto a common time base with a virtual sample rate of 5 samples/s.

Cold junction compensation is realized with an isothermal block inside which the junctions between thermocouple material and copper wiring are located, see figure 2.6. The reference temperature T_0 inside the block is measured using a four-wire RTD[14] and provided as input for the multiplex scanner. The measurement temperature T_1 is then determined from the measured voltage, taking the reference temperature at the cold junction into account.

[11] from Thermocoax type 2ABAc05/200/TMS025-3mm/D30/2AB21T/2m
[12] from Agilent type 34970A
[13] from Agilent type 34902A
[14] type Pt100, electrical resistance $R_0 = 100\,\Omega$ at $T = 0\,°C$

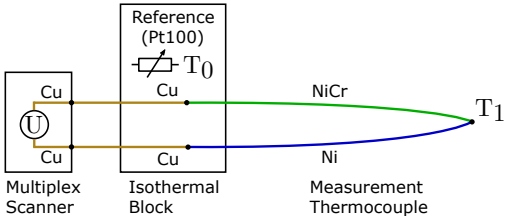

Figure 2.6: Principle of temperature measurements with type K thermocouples

Application

For internal flows, the fluid bulk temperature is a commonly used reference temperature for the evaluation of convective heat transfer. It represents a mass-averaged mean temperature per channel cross-section, compare Baehr and Stephan [5], and is defined as

$$T_b = \frac{\int_A u\rho c_p T_f \, \mathrm{d}A}{\int_A u\rho c_p \, \mathrm{d}A} \tag{2.13}$$

where T_f is the local fluid temperature. The fluid bulk temperature T_b cannot be measured directly in an experiment. However, Jenkins et al. [28] showed that for highly mixed internal flows the centerline temperature is a satisfactory approximation of the bulk temperature. In this thesis the fluid temperature history is measured with thermocouples at several stream wise positions along the channel, as shown in figure 2.7a. At each position there is either a single thermocouple (red) or a thermocouple pair (green). They are inserted into boreholes from outside and fixated with hot-melt adhesive that is also used to seal the borehole. The tip of a single thermocouple is positioned in the centroid of the cross-section area. With the exception of thermocouples T10 and T11 the tips of the thermocouple pairs are positioned inside planes parallel to the ribs. In the projected view normal to the cross-section their tips are located at 1/3 and 2/3 the distance w_1 between leading edge and divider web (pass 1) and respectively at 1/3 and 2/3 the distance w_2 between back wall and divider web (pass 2), see figure 2.7b.

Thermocouple pairs were chosen especially for pass 1 to detect possible uneven temperature distributions inside the trapezoidal cross-section. In previous investigations an unfavorable inlet geometry caused a strong shift of the core flow towards the leading edge. Here a single centerline thermocouple would misrepresent the fluid bulk temperature and lead to exaggerated heat transfer

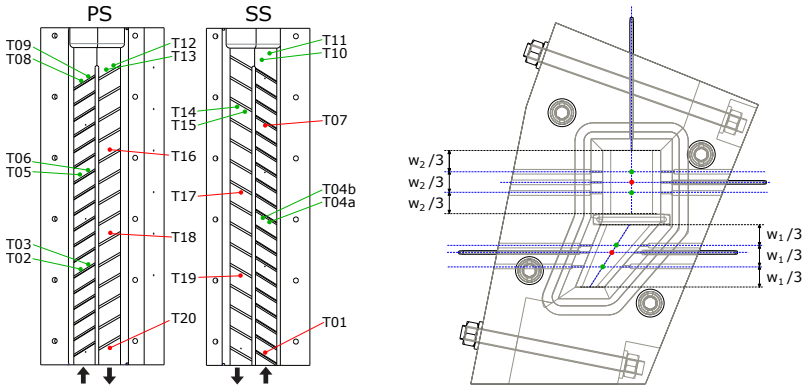

(a) Stream wise position (b) Cross-section position

Figure 2.7: Thermocouple instrumentation

values. Thermocouple pairs are also positioned in pass 2 directly after the bend to account for possible effects of the bend on the temperature profile inside the cross-section. For the heat transfer evaluation a mean value is calculated for the thermocouple pairs.

2.2.5 Pressure Sensors

During the transient experiment the static fluid pressure is measured at several stream wise positions, see figure 2.8. Stainless steal tubes with an outer diameter of 1.6 mm and an inner diameter of 1.4 mm are pressed from the outer surface into boreholes. These pressure tabs are connected to the test channel with boreholes with a diameter of only 0.7 mm. The boreholes are perpendicular to the main flow axis to avoid the influence of any dynamic pressure component. Polyamide pressure measurement tubes with an inner diameter of 1.4 mm connect the pressure taps to a rack-mounted digital sensor array[15] with a 30 psid ($\approx$ 2.1 bar) measurement module. The pressure data are acquired with a sample rate of approximately 2 S/s. In post processing they are resampled with 5 S/s onto the same time base as the thermocouple data.

The pressure and temperature measurements at the channel inlet (P01 and T01) are used to calculate the relevant test parameters and boundary conditions, e.g. the test Reynolds number.

[15] from Scanivalve Corp. type DSA 3016

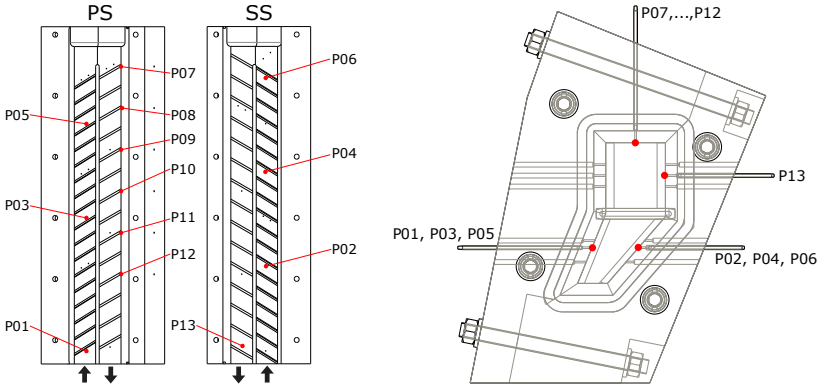

(a) Stream wise position (b) Cross-section position

Figure 2.8: Pressure tap instrumentation

2.3 Experimental Setup

For the execution of the experiments an already existing test facility as presented by Poser [54] could be employed. This facility uses an electric heater and a bypass valve configuration to generate the required fluid temperature step change. Furthermore, a regenerator heat exchanger operated with liquid nitrogen can be used to also produce a cooled down test fluid. A schematic illustration of the test facility is given in figure 2.9. It can be divided into three functional units: air supply system, test section frame and measurement equipment.

Prior to the investigations with the presented model STAT, the bypass valve configuration was extended with a compact bypass valve unit, positioned directly underneath the model. With this unit the fluid temperature step change could be improved by reducing heat losses in the air supply passages upstream of the model. In the following section the test facility is described and a comparison between the previous and the improved temperature change is given. Finally, the procedure for controlling and measuring the mass flow rate and how the Reynolds number is derived from it are explained.

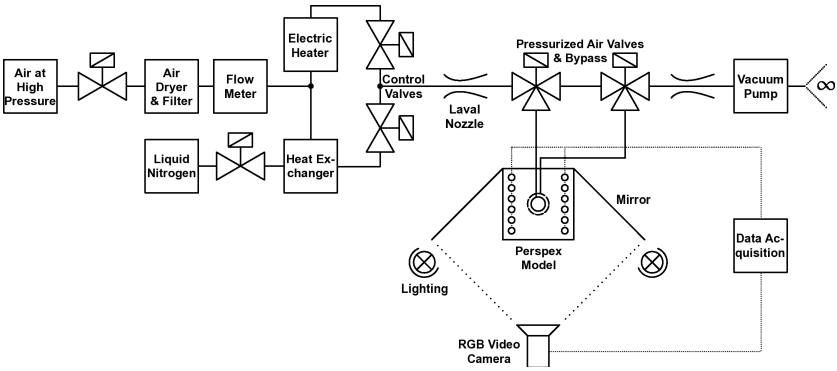

Figure 2.9: Test facility for stationary tests [52]

2.3.1 Air Supply System

For the transient heat transfer experiments the air supply system needs to provide test air with defined conditions such as mass flow rate, temperature and pressure. The air is taken from four 100 bar pressure tanks. The pressure is then gradually reduced with pressure regulators and set by a pressure control valve before the air is lead into a dryer and filter system. Subsequently, the total mass flow rate is measured by a digital flow meter. The facility allows positive fluid temperature step changes with heated air, but also negative fluid temperature step changes where the air is cooled down via a heat exchanger. For this purpose the air can be split and divided between a hot and a cold pass using manual valves. For experiments with a positive step change the cold pass is completely shut off, so that the total air flow is lead through the electrical heater.

For experiments with a negative step change the regenerator heat exchanger is cooled down with liquid nitrogen prior to the experiment. However, during the conditioning phase and experiment, the heat exchanger warms up so that its exit temperature cannot be kept constant. Therefore, both passages are open and the air from the cold and hot passages are mixed to the required temperature. Two sliding gate control valves[16] are used to maintain a constant fluid temperature. A pair of Laval nozzles, one upstream and one downstream of the test section, set the pressure level for the model. Their critical diameters are selected to assure a choked flow. This way also the mass flow rate can be

[16] from Schubert & Salzer

set to a defined value and metered at both Laval nozzles. A vacuum pump at the outlet allows critical pressure ratios for the rear nozzle when test model pressures near ambient pressure is required.

2.3.2 Test Section

The test model with its base block is mounted inside an aluminum framework. They are fixed onto a base plate as shown in figure 2.11b. A newly developed bypass valve unit is located directly underneath the base plate.

Observation Concept

The model can be rotated on the base plate together with the valve unit to allow different viewing angles onto the model. The camera is positioned in a distance of 3 m to 4 m in front of the model with a direct view on the leading edge. The pressure side and suction side are captured via mirrors as shown in figure 2.10a. The mirrors are coated with aluminum without an additional glass layer to provide a high optical quality and to avoid polarization and double reflection issues. They are gimbal-mounted to the aluminum framework and can be adjusted very precisely. An exemplary video frame of an experiment is shown in figure 2.10b.

Bypass Valve Unit

The bypass valve concept plays an important part in generating the temperature change for the transient heat transfer experiments. The idea is to condition the test air and to temper the air supply passages before the start of the experiment. By switching the test air from bypass into the model section a fluid temperature step change can be generated. The best approximation of an ideal step change can be achieved when heat losses in the pipework between tempered bypass section and test channel inlet are minimized.

A bypass valve unit was designed that consists of three switching valves[17] integrated in a stainless steel block, see figure 2.11. This unit can be positioned very near to the test model. The passage length between inlet valve and base block is only 168 mm. Furthermore, this passage is thermally insulated with a Perspex sleeve. At the end of the passage a flow straightener[18] is fitted

[17] from Schubert & Salzer type 8041
[18] from Tubus Bauer, $d_{tube} = 2.5\,\text{mm}$, $L = 40\,\text{mm}$

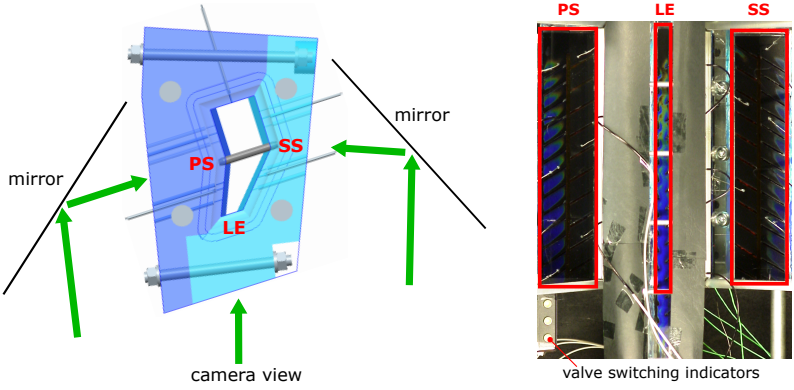

(a) (b)

Figure 2.10: Observation concept: (a) illustration of camera view on model, (b) exemplary video frame of experiment

directly underneath the base block. The valve unit is connected to the air supply system via flexible tubes.

The valves are pneumatically operated. The default position is *open* for the bypass valve and *closed* for the inlet and outlet valves. This default state is used during the conditioning phase where the required mass flow rate and temperature is set for the test air. The temperature is monitored with a thermocouple directly upstream of the inlet valve. When constant test conditions are reached the experiment can be started by switching all three valves simultaneously. The bypass valve closes and the inlet and the outlet valves open to allow the test air to flow through the model.

The resulting fluid temperature change for an exemplary experiment with the model STAT is shown in figure 2.12. Here the temperature upstream of the inlet Laval nozzle was 74 °C and upstream of the inlet valve it was 65 °C at the start of the experiment. The isothermal start temperature of the model was 23 °C.

With the bypass valve unit a good approximation of the ideal fluid temperature step change can be achieved, especially at the channel inlet. Further downstream the temperature histories are more and more smoothed as a result of the heat transfer between test fluid and channel wall.

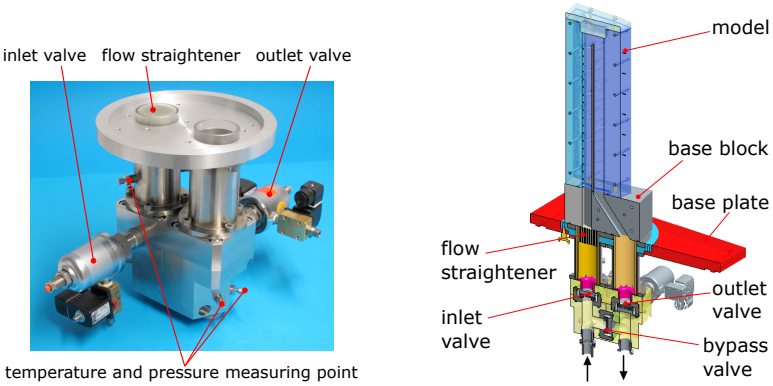

(a) Bypass valve unit (b) CAD cross-section

Figure 2.11: Bypass valve unit for improved fluid temperature step change

2.3.3 Measurement Equipment

The test facility is equipped with several temperature and pressure measuring points. The total mass flow rate is measured with a digital flow meter. During the warm-up and conditioning phase the current values are monitored and used to assess the suitable starting conditions for the experiment.

Temperature and Pressure

For temperature measurements the same type of thermocouple and data acquisition system as described in section 2.2.4 are used. Especially due to the choked Laval nozzles that require a certain pressure ratio the pressures of the test facility can be much higher than the test model pressures and exceed the range of a 30 psid module significantly. Therefore, a pressure measurement module with a differential pressure range of 100 psid (≈ 6.9 bar) is applied. At most monitoring points both temperature and pressure are measured. Some important measuring points are for example: upstream of the Laval nozzles, upstream of the inlet valve, and upstream of the flow straightener. Some auxiliary measuring points are upstream of the electric heater and downstream of the outlet valve. Additionally, the pressures at the vacuum pump and inside the heat exchanger are measured.

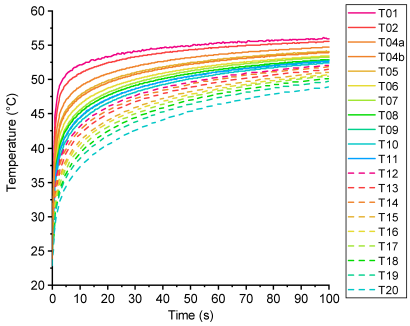

Figure 2.12: Fluid temperature histories (STAT)

Mass Flow Rate

The total mass flow rate is measured with a digital flow meter[19], which is calibrated for dry air at a nominal temperature of 20 °C. Mass flow rates for the investigation of STAT range from 5 g/s (corresponding to a Reynolds number of $Re = 10000$) to 20 g/s (corresponding to a Reynolds number of $Re = 40000$). The data are acquired with a sample rate of approximately 2 samples/s. Just like the pressure data they are resampled with 5 samples/s onto the same time base as the thermocouple data.

In post processing the mass flow rate is additionally determined at the Laval nozzles. The mass flow through a Laval nozzle can be increased by increasing the nozzle pressure ratio. However, at a certain pressure ratio the flow velocity in the critical cross-section reaches sonic conditions. This is called a choked flow. The mass flow rate becomes independent from the outlet conditions and cannot be further increased by reducing the downstream pressure. Assuming ideal gas behavior and an adiabatic and isentropic nozzle flow this critical pressure ratio is

$$\frac{p^*}{p_0} = \left(\frac{2}{\kappa + 1}\right)^{\frac{\kappa}{(\kappa-1)}} \tag{2.14}$$

where p^* is the critical downstream pressure below which choking occurs, p_0 is the total (stagnation) upstream pressure, and κ is the isentropic exponent. For air with an isentropic exponent of $\kappa = 1.4$ the critical downstream pressure is $p^* = 0.528\, p_0$. The test parameters are chosen so that critical conditions for

[19] from HASTINGS type HFM-305D, max. 2500 slpm flow rate

both Laval nozzles are assured. Additionally, the pressure ratios are determined in post processing for validation.

For a choked flow the velocity in the critical cross-section reaches sonic speed and can therefore be calculated for an ideal gas as

$$u_c = \sqrt{\kappa R T_c} \tag{2.15}$$

where T_c is the static temperature in the critical cross-section and R is the specific gas constant. The mass flow rate in the critical cross-section is then

$$\dot{m} = \rho_c A_c u_c = \frac{p_c}{R T_c} \frac{\pi}{4} d_c^2 \sqrt{\kappa R T_c} \tag{2.16}$$

where p_c is the static pressure in the critical cross-section with the area A_c and d_c is the critical diameter. The unknown parameters T_c and p_c are determined from the measured static temperature T_1 and static pressure p_1 at the Laval nozzle's inflow section, assuming isentropic nozzle flow.

Reynolds Number

The Reynolds number is derived from the mass flow rate

$$Re(t) = \frac{\dot{m}(t)\ d_{h1}}{A_1\ \mu(t)} \tag{2.17}$$

where the hydraulic diameter d_{h1} of the inlet passage is the characteristic length, A_1 is the cross-section area of the inlet passage and μ is the dynamic viscosity. An empirical equation based on Sutherland [64] is used to determine the dynamic viscosity from the fluid temperature measurement (thermocouple T01) at the channel inlet

$$\mu(t) = \frac{0.000001458 \cdot T_f(t)^{1.5}}{T_f(t) + 110.4} \qquad T \text{ in K},\ \mu \text{ in Pa s} \tag{2.18}$$

Figure 2.13 shows the developments of the dynamic viscosity and the Reynolds number for an exemplary experiment with a target Reynolds number of $Re_{targ} = 20000$. While the mass flow rate can be kept constant quite well, the dynamic viscosity is rising during the experiment. This is caused by the fluid temperature change (see figure 2.12), which is, however, fundamental for the transient measurement method and therefore cannot be avoided. Thus, also the Reynolds number cannot be kept constant and decreases during the experiment. Figure 2.13 shows that the target Reynolds number of $Re_{targ} = 20000$ was

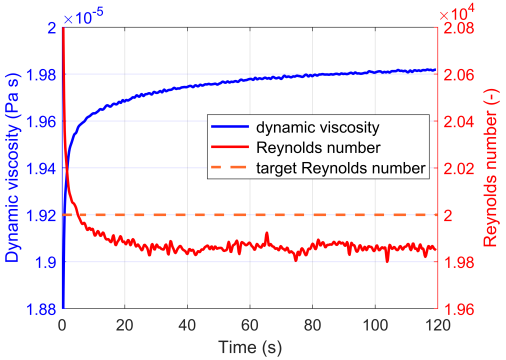

Figure 2.13: Dynamic viscosity and Reynolds number development for an exemplary experiment (STAT, $Re_{targ} = 20000$)

not reached perfectly. The mean value (averaging between 0 s to 90 s) was determined to $Re_{mean} = 19892$.

2.4 Heat Transfer Evaluation

Heat transfer evaluation is performed as described in detail by Poser [54]. With the in-house tool ProTeIn the acquired video is processed and analyzed to detect the TLC indication times. The fluid temperature measurements are provided as input for ProTeIn as basis for the interpolation of 2D-fluid temperature fields. Subsequently, the heat transfer distribution is determined by evaluating equation (2.10) as described in section 2.1. The results are presented as 2D-Nusselt number plots. Finally, data reduction techniques to obtain segment- and line-averaged heat transfer data are presented.

2.4.1 Gmax Time Detection

Figure 2.10b shows an exemplary frame of the original video. The start of the experiment is indicated by valve switching indicators that are visible in the video. By cutting the video at the first appearance of the valve switching signal, the start of the video is synchronized with the start of the experiment. Subsequently, the video is cropped to the relevant heat transfer surfaces, as marked by the red rectangles in figure 2.10b. This way three individual videos for PS, LE and SS are obtained. Figure 2.14 shows exemplary frames of the cut and cropped videos. Each of these videos is analyzed separately.

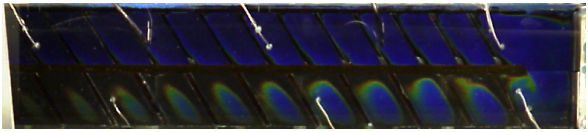

(a) PS

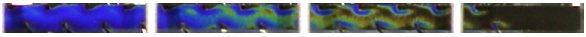

(b) LE

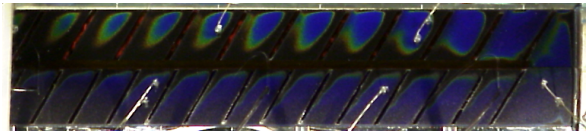

(c) SS

Figure 2.14: Exemplary frame of cut (time) and cropped (area) videos

The first step in ProTeIn is preprocessing of the raw RGB-signals. For each pixel, the three RGB color signals are noise filtered in the time domain. A discrete wavelet transformation filter employing the FBI wavelet is used for this purpose [52]. Wavelet filtering has several advantages compared to other filtering methods. The most important one is the ability to retain the temporal tendency of the signal so that the positions of peaks are not shifted in time, like e.g. for moving average filtering. Since the evaluation method relies on peak-detection in order to find the TLC indication times, this characteristics is essential. Furthermore, it is less time-consuming than e.g. a Savitzky-Golay filter, considering the computational load of filtering the signal of every pixel of the video individually. The raw video has a 24 bit RGB color encoding. During the filtering process the 8 bit intensity value of a single color channel is converted to a floating point value. This way the available digital bandwidth is increased for the filtered signal.

The second step is adaptive normalization for each color channel, where the base-level of the signal corresponds to zero, and the maximum value corresponds to one. Figure 2.15a shows the intensity histories for the raw RGB signal for one exemplary pixel. The respective filtered and normalized signals are shown in figure 2.15b. For the green color channel the position of the maximum intensity (Gmax) is marked by a black square. The corresponding time (t_{Gmax}) is indicated by a dashed black line. This is the TLC indication time we were looking for. At this point in time the wall reached the TLC indication temperature ($T_{TLC} = T_{Gmax}$) that was determined in a stationary calibration as described in section 2.2.2.

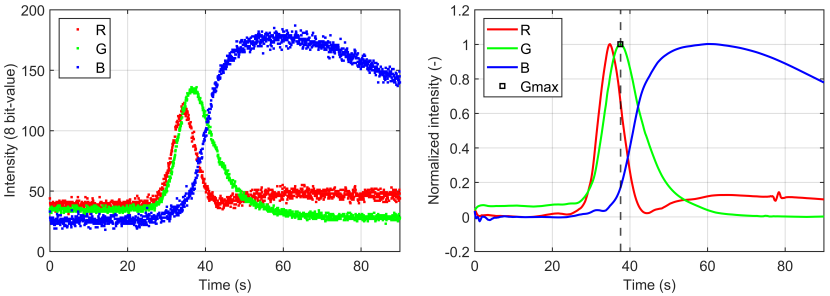

(a) Raw signal (b) Filtered and normalized signal

Figure 2.15: Intensity histories of RGB-channels for one exemplary pixel

By analyzing the whole video domain in the same way we obtain contour plots of the local TLC Gmax time distribution as shown in figure 2.16a. Here the results of the three individually analyzed videos are combined into a single plot, which was created with the data visualization software Tecplot®. Since the PS and SS were acquired via mirrors, the respective contour plots have also been mirrored in order to align them with the LE. This allows an unfolded view on the channel walls. Areas where the heat transfer cannot be evaluated are blanked out. These are for example the ribs, the divider web or the three bolts that block the view on the leading edge.

Regions where thermocouples and pressure tubes obstruct the view on the TLC coated surfaces can be detected in the contour plot, as these show a

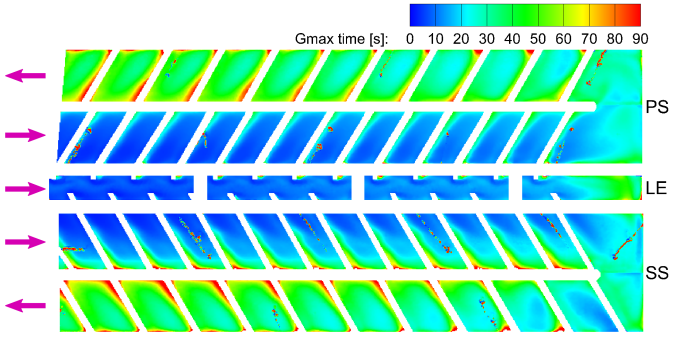

(a) Original Gmax time

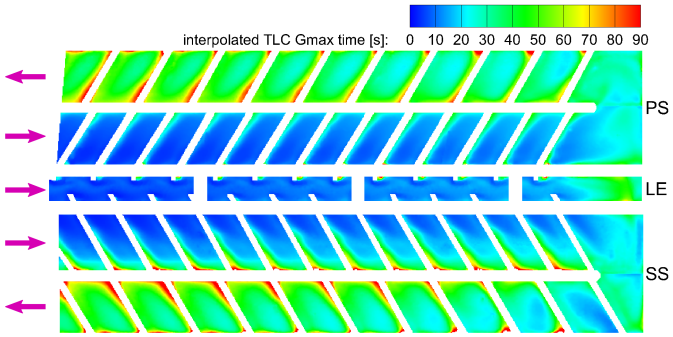

(b) Interpolated Gmax time

Figure 2.16: TLC indication times

distinguishable pattern. Of course here the intensity signal does not contain a definite peak, so filtering, normalization and peak detection leads to meaningless t_{Gmax} values. ProTeIn uses an artificial neural network to detect these areas where the measured intensity signal clearly differs from a genuine TLC signal. The corresponding data are omitted and the resulting gaps filled using a 2D interpolation algorithm. The result is shown in figure 2.16b.

2.4.2 Fluid Temperature Field Interpolation

In order to evaluate the heat transfer for every pixel of the investigated surface, the fluid temperature histories at the position of these pixels have to be known. However, since the thermocouple measurements only provide data at certain points along the channel, the remaining unknown data have to be interpolated. Based on the video, a 2D sketch of the fluid flow boundaries is generated. Figure 2.17 shows this 2D fluid domain exemplary for the pressure side.

Inside this region the positions of the thermocouples are marked manually as green lines. At these markers the thermocouple data are set as inner boundary conditions for the interpolation. It has proved advantageous for the interpolation to set the temperature markers not as a single point, but as a line in the cross-section, at the position of the thermocouple tip. For thermocouple pairs (e.g. T02 and T03) one marker is set in the middle between both thermocouples. Here their mean value ($\overline{\text{T02T03}}$) is used to set the boundary condition.

The two-dimensional interpolation method is based on the Laplace equation, which is used here as a diffusion model to calculate the 2D fluid temperature field.

$$0 = \frac{\partial^2 T_f}{\partial x^2} + \frac{\partial^2 T_f}{\partial y^2} \tag{2.19}$$

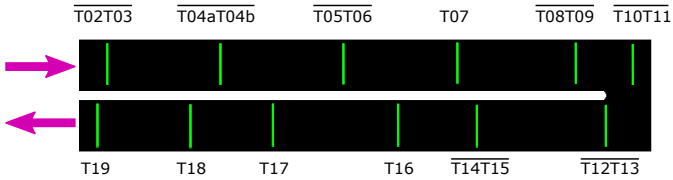

Figure 2.17: Fluid domain with markers for the inner boundary conditions (TC positions) for fluid temperature field interpolation (exemplary for pressure side, STAT)

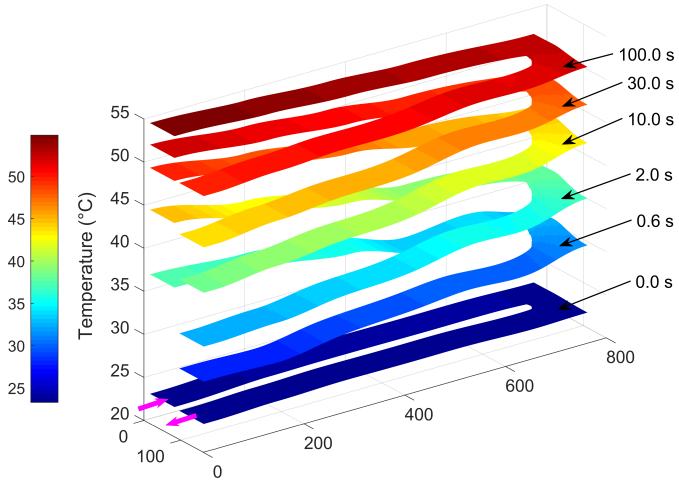

Figure 2.18: Interpolated fluid temperature fields at selected points in time (exemplary for PS, STAT, $Re_{targ} = 20000$)

Equation (2.19) is modeled in ProTeIn as a finite difference method to propagate the temperature information from the internal boundary conditions onto the entire evaluation domain. A solution for $T_f(x,y)$ is calculated by an iterative technique for every individual time step. The thermocouple data are available with a sample rate of 5 samples/s (after resampling), so a solution is obtained for every 0.2 s. Figure 2.18 shows the resulting fluid temperature fields at selected points in time, exemplary for the pressure side. The underlying thermocouple data are the same as presented in figure 2.12 for an experiment at $Re_{targ} = 20000$ with the model STAT.

2.4.3 Data Analysis

Now that we have the TLC indication times $t_{Gmax}(x,y)$ determined from the video analysis, the TLC indication temperature T_{TLC} determined from the TLC calibration, and the fluid temperature histories $T_f(x,y,t)$ determined from the temperature field interpolations, we can solve equation (2.10) for the heat transfer coefficients $h(x,y)$. From that we can determine the Nusselt

numbers $Nu(x,y)$ and employ a correlation to obtain a reference value Nu_0 for normalization of the Nusselt numbers.

Heat Transfer Coefficient

At the time of the TLC indication the surface has reached the TLC indication temperature ($T_w(t_{Gmax}) = T_{TLC}$). With this information inserted into equation (2.10), we get

$$T_{TLC} - T_0 = \sum_{j=1}^{N} \left[1 - \exp\left(\beta^2\right) \operatorname{erfc}\left(\beta\right)\right] \cdot \Delta T_{f(j,j-1)}$$

$$\text{with} \quad \beta = h\sqrt{\frac{t_{Gmax} - \tau_j}{\rho c k}} \tag{2.20}$$

Equation (2.20) is numerically solved for every pixel position (x,y). The resulting contour plot of the heat transfer coefficients $h(x,y)$ is given in figure 2.19a.

Nusselt Number

To translate this $h(x,y)$-distribution into a Nusselt number distribution $Nu(x,y)$ the local heat conductivity of the fluid $k_f(x,y)$ is required. A Sutherland based correlation for the temperature dependency of k_f is given in White [78]. ProTeIn uses this correlation, while taking the time-averaged local fluid temperature history $\overline{T_f}(x,y)$ into account. Whereby only the temperature values between start of the experiment and the respective TLC indication time are considered for averaging.

$$k_f(x,y) \approx \left(\frac{\overline{T_f}(x,y)}{273}\right)^{\frac{3}{2}} \cdot \frac{11.2547}{\overline{T_f}(x,y) + 194} \qquad T_f \text{ in K},\ k_f \text{ in W/(m K)} \tag{2.21}$$

The Nusselt number distribution is then

$$Nu(x,y) = \frac{h(x,y) \cdot d_h}{k_f(x,y)} \tag{2.22}$$

Figure 2.19b shows the resulting contour plot of the Nusselt number distribution.

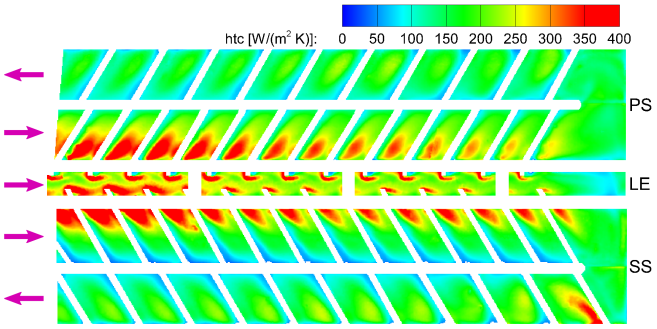

(a) Heat transfer coefficient

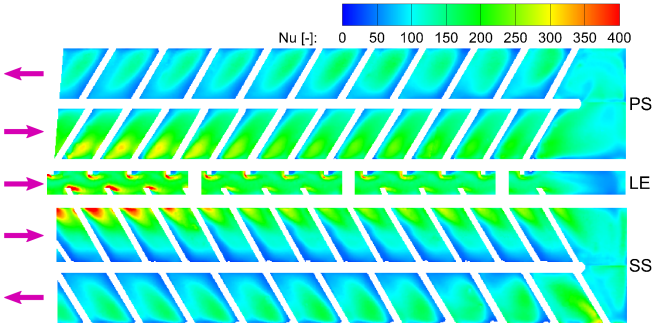

(b) Nusselt number

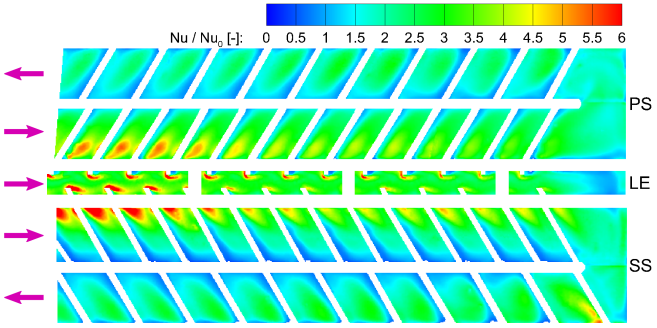

(c) Normalized Nusselt number

Figure 2.19: Results of heat transfer evaluation and data analysis

Normalized Nusselt Number

The Nusselt number is already a dimensionless quantity. It can therefore be used e.g. to predict real engine behavior, or to compare the experimental results with CFD results. However, the Nusselt number level is still dependent from the Reynolds number. So, for the possibility to compare experiments conducted at different Reynolds numbers, it is common practice to normalize the Nusselt number with a suitable reference value obtained by a correlation. In this thesis a correlation for turbulent flow in smooth channels by Dittus-Boelter/ McAdams [79] is used

$$Nu_0 = 0.023\, Re^{0.8} Pr^n \tag{2.23}$$

where the parameter n is dependent from the heat transfer direction. If the heat flow is from hot fluid to cold wall, like for the stationary experiments with STAT, then $n = 0.3$. If the heat flow is from hot wall to cold fluid, like for the experiments with rotation, then $n = 0.4$. For the Reynolds number the mean value Re_{mean} and for the Prandtl number a constant value $Pr = 0.7179$ for air was used. The resulting contour plot of the normalized Nusselt number distribution $\frac{Nu(x,y)}{Nu_0}$ is given in figure 2.19c

2.4.4 Data Reduction

This section presents data reduction methods for deriving line averaged and segment averaged data from the local values.

Line Averaging

With the line averaging method mean values along the stream wise coordinate s are determined. The averaging lines are chosen parallel to the ribs for PS and SS and transverse to the direction of flow for LE as indicated by the red dashed lines in figure 2.20. The definition of s can also be seen in this figure. The origin of this stream wise coordinate is set at the tip wall of the channel, so that negative values refer to pass 1 and positive values refer to pass 2.

For the LE this method is realized by simply averaging the columns of the respective data array. For PS and SS an image warping algorithm implemented in LabVIEW is applied. The fist step is to select a parallelogram that is aligned with the respective rib angle as indicated in figure 2.20. Pass 1 and pass 2 are evaluated individually with separate parallelograms. The values

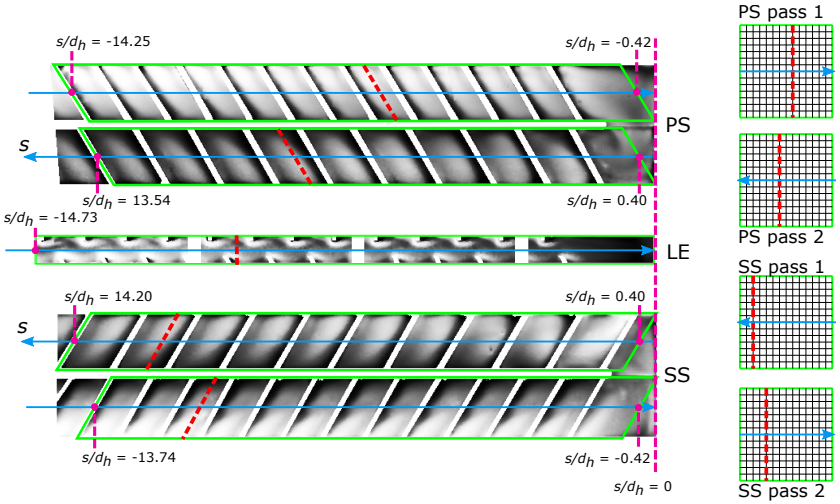

Figure 2.20: Evaluation domains, coordinates and illustration of warping method for line averaging, STAT

inside the parallelogram are mapped onto a square grid of arbitrary size. This virtually morphs the parallelogram into a square. The grid dimensions should be approximately the number of data points (i.e. number of pixels) inside the parallelogram along the s-coordinate. The remaining unknown grid values are interpolated using the diffusion model as described in section 2.4.2. This method warps the evaluation domain so that the ribs now appear as vertical lines on the square grid.

Line Averaging is then performed, just like for LE, by averaging the columns of the data array. By using this method, however, some areas are neglected. Especially in the bend region there are triangular shaped areas left that are not considered for this evaluation. In the inlet and outlet region only complete rib segments are included.

In order to only use non-dimensional values for data visualization, s is normalized with the hydraulic diameter of passage 1. Figure 2.21 shows the line averaged normalized Nusselt numbers plotted against the normalized stream wise coordinate s/d_h.

The diagram shows the characteristic profiles for a cooling channel with rib turbulators. Directly downstream of the ribs the heat transfer values are

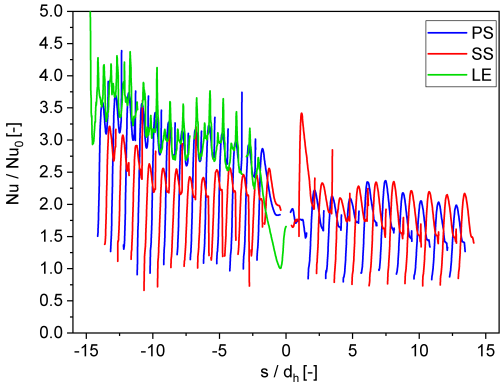

Figure 2.21: Line averaged normalized Nusselt numbers (STAT, $Re_{targ} = 20000$)

relatively low, but due to flow reattachment they are subsequently increasing with a steep gradient up to a local maximum.

It can also be seen that the heat transfer levels can significantly vary between the respective surfaces. In passage 1 the values for PS and LE are notably higher than for the SS, whereas in passage 2 the values for PS and SS are nearly on the same level. The staggered rib arrangement between PS and SS is clearly visible here.

Segment Averaging

For PS and SS area averaging is performed for individual rib segments. Figure 2.22 shows the corresponding segment numeration. Again, segments with a negative number refer to passage 1 and segments with a positive number to passage 2. The bend regions are divided along the divider web main axis, so that the resulting parts can be associated with passage 1 (b1) and passage 2 (b2) respectively.

For this method first individual masks for each segment are created using an image processing software, e.g. GIMP[20]. Area averaging is then performed in LabVIEW™ by calculating the arithmetic mean value of all data points inside the respective mask. Figure 2.23 shows the segment averaged normalized Nusselt numbers plotted against the segment numbers. Here too only complete

[20]GNU Image Manipulation Program

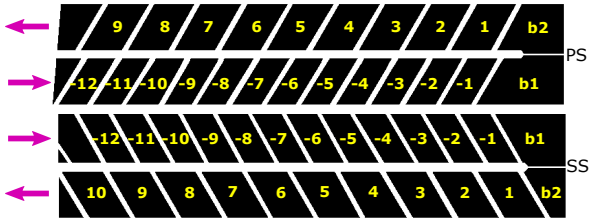

Figure 2.22: Segment numeration (STAT)

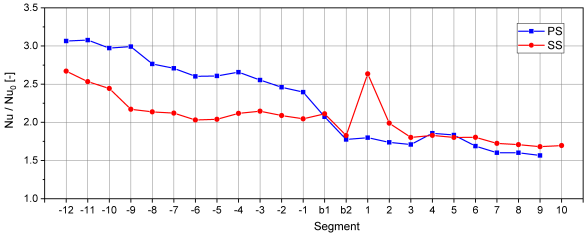

Figure 2.23: Segment averaged normalized Nusselt numbers (STAT, $Re_{targ} = 20000$)

rib segments are considered for evaluation. Truncated segments in the inlet and outlet region are neglected.

Also the different heat transfer levels between PS and SS in passage 1 can be clearly seen in this diagram. For SS a significant increase in heat transfer can be seen in the first segment downstream of the bend due to a reattaching flow in this area.

With every data reduction step some underlying information gets lost. While here, in contrast to the line averaging method, every data point of the bend region is included in the averaging process, references to e.g. the stacked rib arrangement is completely missing in this representation of the data.

2.5 Aspects to Consider for Rotating Experiments

The previous sections described the application of the transient TLC heat transfer measurement method for stationary experiments. This section lists

the main aspects that have to be considered for applying this method for experiments with a rotating model.

Due to additional centrifugal forces and higher test air pressures, mechanical aspects like tensile and bending stresses have to be taken into account. Because of the moving test model the observation concept has to be revised and new optical aspects have to be considered. Also thermal aspects regarding the required fluid temperature step change have to be noted. Furthermore, a telemetry system has to be applied for data acquisition.

2.5.1 Mechanical Aspects

At the maximum rotational speed of 900 rpm the investigated test model experiences centrifugal accelerations of up to 815 g. All components must be selected and the model itself must be designed to withstand these additional centrifugal forces. The investigated rotating model (ROT-B) has a more compact and sturdier design than the stationary model (STAT). The mantles of the thermocouples that measure the fluid temperature inside the channel are reinforced with capillary steel tubes to prevent bending. All connections and cables have strain relief.

The experiments are conducted with air pressures of up to 10 bar (absolute) in order to achieve the required test conditions. Therefore, the model is mounted inside a pressurized model housing and the air passage routing was designed to minimize pressure forces on the model.

2.5.2 Observation and Optical Aspects

There are two possible approaches to capture the TLC color play of a rotating model with a video camera. The first one is a stationary camera that is synchronized with the rotational speed to capture one image per revolution at a specific angular position of the model. With this measurement principle, however, the video frame rate is directly dependent from the rotational speed of the model. Especially for low rotational speeds the frame rate would become too low. This would result in high uncertainties for the measured TLC indication times. A possible solution to achieve higher frame rates with this method is to use multiple cameras at different angular positions around the circumference of the rotor. However, this would require time-consuming image registration methods in post processing to combine the video footage of multiple cameras into a single video. Another disadvantage is motion blur, which increases with

the rotational speed of the model. To minimize this effect a triggered strobe system with very short flash durations would be required for every used camera.

The second approach, that is employed here, uses cameras that are rotating together with the model. The biggest advantage is that a fixed, high frame rate can be used that doesn't need to be synchronized with the rotational speed. Furthermore, as there is no relative motion between test model and camera, motion blur is not an issue. The biggest disadvantage is the very small distance between model and camera, which requires the implementation of a wide angle lens. This inevitably leads to a significant perspective distortion with a distinct fisheye effect.

The selection of cameras that can withstand the occurring centrifugal accelerations, however, is limited. High performance industrial cameras cannot be used as their weight, internal design, power requirements and data interface make it difficult to implement them in a rotating system. Small camera modules, such as those used in smartphones or action cameras, are better suited. The video footage can then be saved internally on a micro SD card. Also their lens systems are much smaller and lighter and therefore less prone to deformation due to centrifugal forces. However, compared to an industrial camera, limitations regarding performance and the configuration of the camera settings must be accepted.

2.5.3 Thermal Aspects

For the stationary experiments the required fluid temperature is provided by an electric heater to create a positive fluid temperature step change. The heat transfer is then from fluid to test channel wall during the experiment, resulting in density distributions that do not correspond to reality. However, for typical flow conditions of these heat transfer experiments the effects of gravity on the flow due to density differences can be neglected.

For experiments with rotation the influence of centrifugal acceleration on the flow due to the density differences cannot be neglected. Therefore, the heat transfer needs to be in the correct direction from test channel wall to fluid in order to reproduce comparable density distributions. For this a cooling air supply system using a liquid nitrogen operated heat exchanger is implemented. This system can provide temperatures down to $-120\,^{\circ}\mathrm{C}$ for the test air.

As shown in section 2.3.2, it is advantageous to position the bypass valve system as near as possible to the test model to approximate an ideal fluid temperature step change as well as possible. However, it would be very difficult to implement

a bypass valve unit such as the one presented in figure 2.11 in a rotating system. It cannot be guaranteed that the valves would function accurately under centrifugal loads. Furthermore, the valves would need pneumatic or electric actuation. Both options would require complex solutions including slip rings and/or rotary unions.

The more practical approach is to keep the bypass valve unit in the stationary system and rather pre-cool the air supply passages inside the rotor in order to minimize heat exchange of the test air before entering the model. For this purpose the internal test air supply lines are designed as integrated heat exchangers which are fed by a secondary temperature control air circuit.

2.5.4 Aspects of Data Acquisition and Synchronization

To acquire fluid temperature and pressure measurement data from inside a rotating model, a telemetry system is needed. Analog-to-digital conversion of the thermocouple and pressure sensor signals is performed by a co-rotating sensor signal amplifier. The digitized values are then transmitted in real-time via a HF-radio signal to a stationary receiver.

For the stationary experiments the video footage could be directly saved to a measurement computer. In contrast, the rotating cameras store their video material on internal micro SD memory cards. For additional real-time monitoring the video signal is transmitted via a bluetooth connection. After the experiment the video material is downloaded from the memory card to a network attached data storage.

CHAPTER 3

Test Rig for Rotational Effects

In this chapter the rotating test rig for the investigation of rotational effects on the heat transfer distribution is presented. The rig was designed in close cooperation with industrial partners and set up at the *Institut für Thermodynamik der Luft- und Raumfahrt* (ITLR) at the *Universität Stuttgart*. First, the main requirements for the test rig to achieve the targeted test parameters are discussed. After that, the design of the rig and the investigated test model are presented. Finally, the experimental procedure and data evaluation processes as well as the result of validation tests are shown.

3.1 Requirements and Test Parameters

The behavior of a physical system is defined by a complete set of *dimensionless* quantities formed by the relevant *physical* variables. This fact suggests that if two systems have the same numerical values for all the defining dimensionless quantities, then these two systems are dimensionally similar and their behavior can be closely correlated [65]. Therefore, the results of measurements on a model can be used to assess the behavior of a dimensionally similar prototype.

The complete set of dimensionless quantities that describe the behavior of a rotating cooling channel are given in equations (3.3) to (3.8). A derivation of these quantities is given in appendix B.

3.1.1 Dimensionless Quantities

For a rotating cooling channel the heat transfer mainly depends on the following dimensionless quantities:

$$Nu = f\left\{Re, Ro, Bo, Pr, Ma\right\} \tag{3.1}$$

The Nusselt number Nu is the ratio of convective to conductive heat transfer

$$Nu = \frac{h d_h}{k_f} \tag{3.2}$$

where h is the heat transfer coefficient, k_f is the thermal conductivity of the fluid and the hydraulic diameter d_h is employed as characteristic length.

The Reynolds number Re is the ratio of inertial forces to viscous forces

$$Re = \frac{u d_h}{\nu} = \frac{\rho u d_h}{\mu} = \frac{\dot{m} d_h}{A\mu} \tag{3.3}$$

As the fluid velocity u inside the channel cannot be measured directly, the Reynold number is derived from the mass flow rate $\dot{m}$, as described in section 2.3.3.

The rotation number Ro is the ratio of Coriolis forces to inertial forces

$$Ro = \frac{\Omega d_h}{u} = \frac{\rho A \Omega d_h}{\dot{m}} \tag{3.4}$$

Assuming ideal gas ($p = \rho R T$), equation (3.4) can be further modified

$$Ro = \frac{p A \Omega d_h}{R T \dot{m}} \tag{3.5}$$

Equation (3.5) shows, that for a given channel geometry (A, d_h) and given mass flow rate $\dot{m}$ (and therefore given Reynolds number Re), the rotation number can be increased by increasing rotational speed Ω or by increasing pressure p. Therewith being able to change independently Ω and p for a given Re offers high flexibility.

The buoyancy number Bo is the ratio of buoyancy forces to inertial forces

$$Bo = \frac{\Delta\rho}{\rho} Ro^2 \frac{R}{d_h} = \frac{T_w - T_f}{T_w} Ro^2 \frac{R}{d_h} \tag{3.6}$$

It is dependent from the density differences $\Delta\rho$ inside the fluid. In our definition of Bo the density ratio is expressed as a temperature ratio, where the temperature difference between the initial wall temperature $T_w(0) = T_0$ and the fluid temperature T_f at the channel inlet is considered.

The Prandtl number Pr is defined as the ratio of kinematic viscosity to thermal diffusivity

$$Pr = \frac{\nu}{a} = \frac{\mu c_p}{k} \tag{3.7}$$

It depends only on the fluid type and the fluid state. For both the model experiments and real engine operation (prototype), air is used as fluid, so that a general similarity in the Prandtl number is given. For the dimensional modeling and the design of the experiment a constant Prandtl number of $Pr = 0.7$ for dry air is assumed. When evaluating the experiments the temperature dependence of the Prandtl number is taken into account.

The Mach number Ma is the ratio of flow velocity to the local speed of sound

$$Ma = \frac{u}{c} \tag{3.8}$$

In the investigated cooling channels only relatively low flow velocities occur ($Ma < 0.3$). Therefore, the effects of compressibility are small and the test air can be considered incompressible. Thus, the Mach number is not a relevant quantity for our application and we can neglect the similarity in Mach number.

3.1.2 Physical Variables

In cooperation with the industrial partners, the target ranges for the dimensionless quantities to be covered by the rotating rig were defined. Thereby, the parameters of current and also expected parameters of future cooling configurations have been taken into account. The physical variables (the actual test parameters) were then defined on the basis of these target ranges.

In the early design stages the maximum rotation speed was set to $n_{max} = 900\,\text{rpm}$ to limit the mechanical stresses on the rotating components. In order to still be able to provide the required rotation numbers and buoyancy numbers,

fluid pressures of up to 10 bar should be made possible. At a given Reynolds number an increase in the fluid pressure decreases the flow velocity and thus results in an increase in rotation number and buoyancy number. Table 3.1 shows the resulting ranges of test parameters that served as foundation for the design of the rotating test rig. For a simple visualization of the achievable

Table 3.1: Ranges of test parameters

Symbol	Description	Value range	Unit
R	mean model radius	0.75	m
d_h	hydraulic diameter of cooling channel	0.01 ... 0.03	m
p	fluid pressure	1 ... 10	bar
n	rotational speed	0 ... 900	rpm
$\dot{m}$	mass flow rate of cooling fluid	0.002 ... 0.03	kg/s
T_f	fluid temperature	-100 ... +80	°C

ranges of dimensionless quantities, a Monte Carlo simulation has been carried out in Matlab®[1]. For this, experiment simulations have been conducted, where for each of the test parameters p, n and $\dot{m}$ a random value inside the ranges of table 3.1 was selected. Figure 3.1 shows the results for $N = 2 \cdot 10^6$ virtual experiments for a channel with a hydraulic diameter of $d_h = 0.015\,\mathrm{m}$ and an initial wall temperature of $T_w = 293.15\,\mathrm{K}$. Since the measurement principle is based on a fluid temperature change, the minimum temperature difference between wall and fluid was set to 10 K. Thus, the range for the randomly chosen fluid temperature was set to $233.15\,\mathrm{K} \leq T_f \leq 283.15\,\mathrm{K}$.

Buoyancy number and rotation number cannot be set completely independent from each other. Equation (3.6) and figure 3.1c suggest that for a fixed geometry and a given rotation number, the buoyancy number can only be varied by changing the difference between wall temperature and fluid temperature. However, these temperatures also dictate how fast the TLC indications occur in a transient heat transfer experiment. During the planning of the experiment the fluid temperature is specified in such a way that too fast or too late indications are avoided, as both would result in increased measurement uncertainties. Here, the start temperature, the indication temperature of the applied TLCs, and also the targeted Reynolds number have to be taken into account. This means that the margin to select an arbitrary buoyancy number independent from the rotation number is limited.

[1] from MathWorks, Inc.

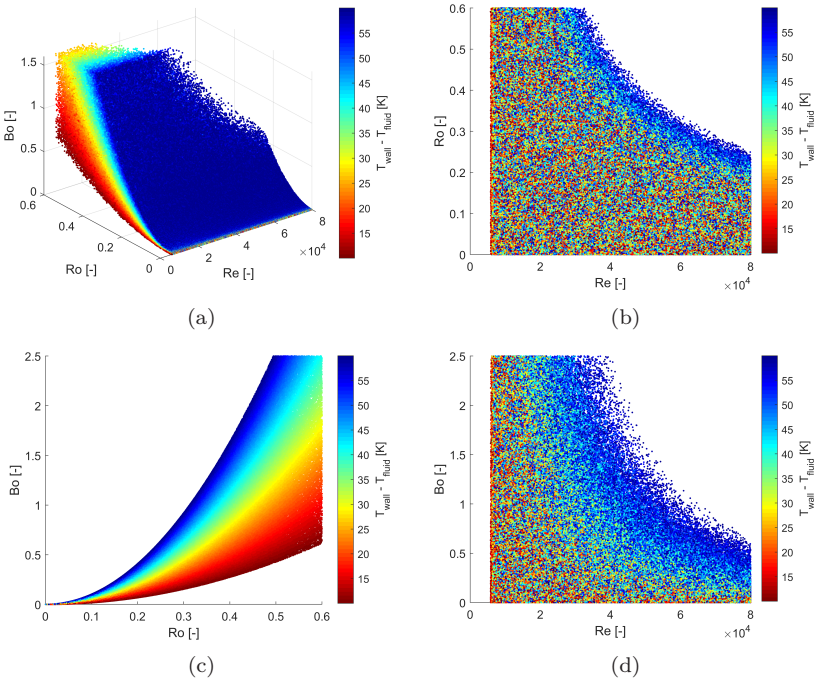

Figure 3.1: Achievable dimensionless quantities for a channel with a hydraulic diameter of $d_h = 0.015\,\mathrm{m}$: (a) 3D-plot for Re, Ro, Bo, (b) 2D-plot for Re, Ro, (c) 2D-plot for Ro, Bo, (d) 2D-plot for Re, Bo

3.2 Design of Test Rig and Facility

At the beginning of the design phase some restrictions and boundary conditions have been defined. The maximum rotor diameter was set to $d_{max} = 2\,\mathrm{m}$. The maximum combined mass of the Perspex model together with its aluminum housing was set to $m_{max} = 50\,\mathrm{kg}$. At the maximum rotational speed of $n_{max} = 900\,\mathrm{rpm}$ the model has a circumferential velocity of $v_{max} = 70.69\,\mathrm{m/s}$ (at the mean model radius of $R_{mean} = 0.75\,\mathrm{m}$). The maximum centrifugal acceleration at this radius is $a_{max} = 6.662 \cdot 10^3\,\mathrm{m/s^2} \approx 679.1\,\mathrm{g}$. This corresponds to a maximum centrifugal force of $F_{max} = 3.331 \cdot 10^5\,\mathrm{N}$, a maximum kinetic energy of $E_{max} = 1.249 \cdot 10^5\,\mathrm{J}$, and a maximum momentum of

$P_{max} = 3.534 \cdot 10^3\,\mathrm{kg\,m/s}$ for m_{max}. With these key data in mind the design process for the rig and the associated safety installations were realized.

3.2.1 Test Rig Overview

Figure 3.2 shows an overview of the rotating test rig. It consists of a rotor

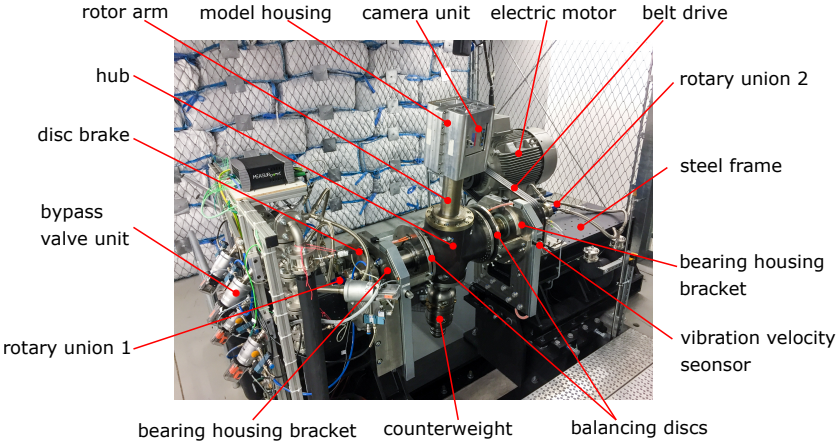

Figure 3.2: Test rig overview

which is supported by two ball bearings. The rotor is mounted in a steel frame comprised of several welding assemblies. The two bearing housing brackets are mounted with a form-fit connection to their corresponding welding assemblies, which can be adjusted translatory and rotatory in all directions in order to align the two bearings. The correct alignment was guaranteed by a laser based measurement system.

An electric motor[2] with a power of 55 kW drives the rotor via a belt drive based on four narrow V-belts[3], while the rotational speed is controlled by a frequency converter. The pulley diameters are $d_1 = 265\,\mathrm{mm}$ for the drive pulley on the motor and $d_2 = 315\,\mathrm{mm}$ for the output pulley on the rotor resulting in a transmission ratio of $i \approx 1.2$.

[2] from Siemens Ag type 1LE 1501-2DC23-4AF4-Zv
[3] from Optibelt GmbH type Super X-Power XPB 2280 Ld

Both directions of rotation are possible. For the start-up procedure an arbitrary sequence of acceleration ramps (up to a maximum acceleration of $\dot{n}_{max} = 600\,\mathrm{rpm}/\,\mathrm{min}$) and holding speeds (up to $n_{max} = 900\,\mathrm{rpm}$) can be predefined. During the controlled deceleration the motor is able to recover the energy and return it to the power grid. In case of a power outage, where the rotor cannot be slowed down via the electric motor, a disc brake can be manually activated. Two brake calipers[4] are pneumatically held open during operation. By opening the pneumatic line, the brake calipers close by spring power to stop the rotor within a few seconds.

The rotational speed is measured by a custom-designed rotary encoder system consisting of a disc with 15 evenly distributed radial boreholes, an inductive sensor[5], and a counter module[6]. The inductive sensor is mounted on a stator and aligned with the encoder disc on the shaft, so that the sensor detects 15 boreholes per revolution. This allows to derive the rotational speed by evaluating the frequency of the borehole detections.

3.2.2 Rotor

A cross-section view of the rotor is given in figure 3.3. The main parts of the rotor: shaft, hub, rotor arm and counter weight arm are manufactured from steel[7] with a high tensile strength. The hollow shaft, both half-shells of the hub, and the rotor arm have been additionally tempered to achieve an ultimate tensile strength of $\sigma_{min} = 880\,\mathrm{MPa}$. Rotor arm and counterweight arm are form-fit connected to the hub. Hub, brake disc, and pulley are mounted to the shaft using clamping sets[8].

The rotor is supported by two bearing housing units[9] consisting of a ball bearing[10] in a cast iron housing designed for flange mounting. The inner rings of the ball bearings are fixed to the shaft by eccentric locking collars. On the brake disc side of the rotor, the housing unit is flange mounted to the bearing housing bracket. Here, axial movement of the rotor is only possible within the tolerances of the bearing itself, so that this side functions as the fixed bearing. On the pulley side of the rotor, the housing unit was customized by removing the flange to create a cylindrical outer contour. This allows axial sliding of the

[4] from Ringspann GmbH type DH 030 FPM
[5] by Balluff type BES040R
[6] from Siemens type 6ES7138
[7] type 817M40 (EN24T)
[8] from KTR Kupplungstechnik GmbH type CLAMPEX KTR 200-120X165
[9] from Schaeffler Technologies AG & Co. KG type RME120
[10] from Schaeffler Technologies AG & Co. KG type GE120-KRR-B

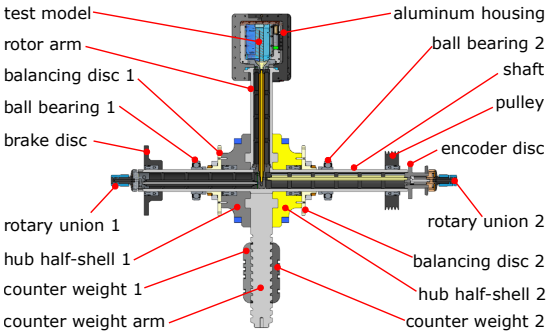

Figure 3.3: Cross-section view of rotor

adapted housing unit inside a corresponding opening in the bearing housing bracket to function as an axial floating bearing.

The test model is installed inside an aluminum housing which is mounted at the end of the rotor arm with a form-fit connection. For balancing, a counter weight consisting of two steel[11] half-shells is mounted to the counter weight arm. It can be installed at discrete radial positions with a spacing of 40 mm. Grooves in the counter weight allow the mounting of smaller weights for fine static balancing. Additional balancing discs are mounted to the side of each of the two hub half-shells to allow precise dynamic balancing of the rotor in two planes. These discs provide threaded holes at regular intervals along the circumference, where screws and washers of different materials and sizes can be attached. A balancing system[12] evaluates the measurement data of two vibration velocity sensors[13] that are directly mounted to the bearing housing brackets. This system then calculates the angular positions on the balancing discs and the respective masses of the balancing weights that need to be added there.

Both ends of the hollow shaft are equipped with rotary unions[14] to introduce air into the rotor. The layout of the internal pipe system for routing the test air to and from the model is described in detail in section 3.2.4.

[11] type AISI304L / DIN1.4307 (X2CrNi18-9)
[12] from Hofmann Mess- und Auswuchttechnik GmbH & Co. KG type AB9000
[13] from Hofmann Mess- und Auswuchttechnik GmbH & Co. KG type PMG 85 HM
[14] from Deublin type 2620-520-252

3.2.3 Test Facility

In addition to the test rig itself, the test facility consists of two other main components: the cooling air supply system and the test rig control and safety installations. Figure 3.4 shows the floor plan and the main infrastructure of the test facility, which is spread over several rooms. The control room, from which the test rig is remotely controlled, is not shown in this illustration.

Cooling Air Supply System

The cooling air supply system can be divided into four functional units:

- compressed air supply
- liquid nitrogen heat exchanger
- temperature mixing
- pressure and mass flow control and measurement

Figure 3.5 shows a schematic diagram of the cooling air supply system with the functional units highlighted.

A screw compressor[15] with an integrated refrigeration dryer provides air with an operating overpressure of 13 bar, a pressure dew point of 3 °C, and a maximum mass flow rate of 111 g/s. In order to guarantee a constant operating pressure, a reservoir with a volume of 3 m^3 is connected downstream of the compressor. This dampens possible pressure fluctuations and ensures stable conditions during an experiment.

The pressurized air is then cooled down and further dehumidified using a custom build heat exchanger[16], which is operated with liquid nitrogen. A special multi-stage process, in which the temperature difference for the heat transfer in the heat exchanger is kept below 30 K, prevents the formation of aerosols. This way, very dry air with temperatures down to −120 °C and corresponding pressure dew points can be provided.

Subsequently, the air is split into two paths. A cold-gas strand and a hot-gas strand. The latter one is electrically heated up again to temperatures up to 80 °C. By mixing these strands back together with a controlled mass flow ratio, arbitrary temperatures within the limits of the two strands can be achieved. Applying this mixing principle, three separate air flows are generated: the

[15] from Kaeser Kompressoren type CSD 85 T
[16] from Messer Group GmbH / Herco Kühltechnik Hermanns & Co. GmbH

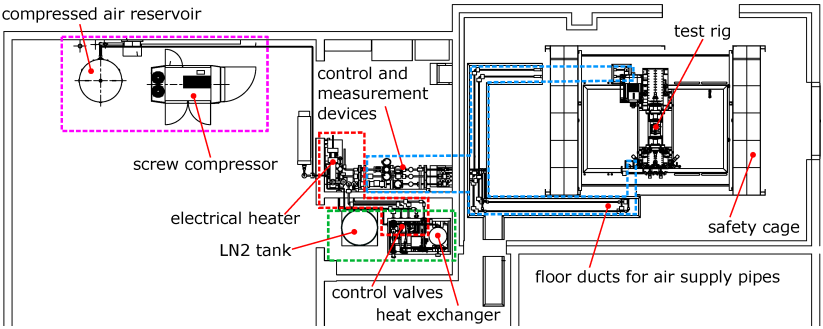

Figure 3.4: Floor plan and main infrastructure of facility

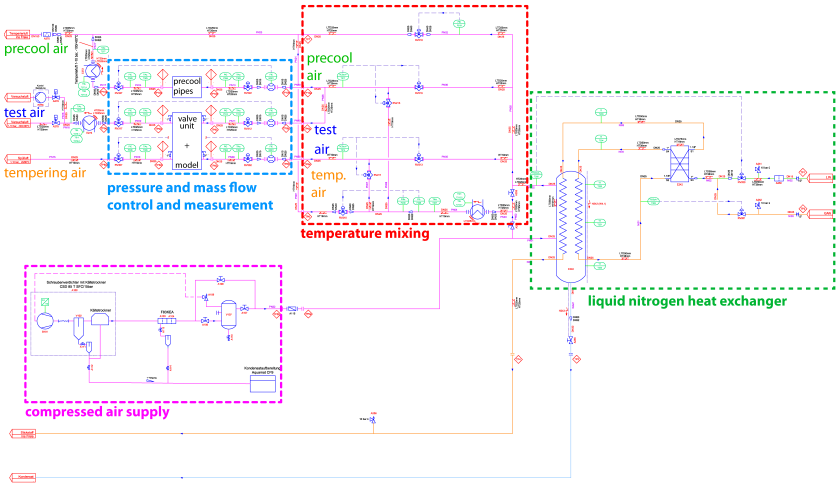

Figure 3.5: Schematic diagram of cooling air supply system

test air, the tempering air and the precool air. A detailed descriptions of the application of these air flows is given in section 3.2.4. If these very low pressure dew points are not required, the heat exchanger can be bypassed and the hot-gas strand can be taken directly from the pressure reservoir and then led to the electrical heater. Thus, the amount of liquid nitrogen needed to achieve the required temperatures can be reduced.

The three air flows are routed to the test rig via copper pipes installed in floor ducts. The test air and the tempering air pipes are connected to a bypass valve unit that controls the flow through a rotary union to the pipes inside the rotor and to the test model, see section 3.2.4. At the opposite end of the shaft, the pipes of the precool air are connected to the second rotary union. With the precool air, the inner air supply lines inside the rotor are conditioned before the experiment.

Control valves[17] are positioned upstream and downstream of the test rig in each of the three air passages to control the pressure level and mass flow rate. Each line is also equipped with pressure transmitters[18] and resistance thermometers[19] upstream and downstream of the test rig. The mass flow rate is respectively measured upstream of the inlet control valves. Since the test Reynolds number is directly determined from the mass flow rate measurement of the test air, a Coriolis flowmeter[20] with a high accuracy (maximum measured error: $\pm 0.35\,\%$ of reading) has been selected for the test air and also for the tempering air. For the precool air, a vortex flowmeter[21] is used. All these control and measurement devices are integrated in a single skid.

Test Rig Control and Safety Installations

The test rig control and the safety concept have been developed in close cooperation with an external company[22]. Several measures for safely operating of the rig have been taken to ensure that it does not pose a hazard to anyone in the vicinity. Operating guidelines have been created and all persons involved were instructed in these guidelines. These include e.g. that no person is allowed in the test room during operation of the rig. An elaborate start-up procedure has been worked out to ensure that the motor can only be started after all

[17] from Samson type: valve 3241, actuator 3277, position controller 3730
[18] from Endress Hauser type Cerabar S PMP 71
[19] from Endress Hauser type PT100 TR12 / TMT 182
[20] from Endress Hauser type Proline Promass 83F
[21] from Endress Hauser type Prowirl F200
[22] Quintec Automatisierungs- und Datentechnik GmbH

points of a checklist have been addressed. The start-up procedure includes e.g. a strict order in which the doors of the safety cage and the test room must be closed and confirmed by a key switch. The final key switch is located in the control room from which the rig is remotely operated and monitored with several surveillance cameras.

The safety cage[23] was designed to withstand the worst case scenario of a catastrophic malfunction at maximum rotational speed. The cage consists of a steel beam construction covered by steel wire mesh. In the rotational plane, bags filled with foam glass gravel are positioned between two layers of wire mesh. In case of an impact, the foam glass filling with a thickness of up to 0.8 m at the sidewalls and 0.4 m at the ceiling, is able to absorb the energy and distribute the resulting forces onto a large area of the steel wire mesh. The basis for the design of the cage was an assumed error case where the complete aluminum model housing detaches at full speed. The kinetic energy of this *projectile* is $E_{max} = 1.249 \cdot 10^5$ J. The durability of the cage is guaranteed for an impact energy of $E_{kin} \leq 1.4 \cdot 10^5$ J

3.2.4 Fluid Temperature Step Change

For the stationary tests, a bypass valve unit was positioned as near as possible to the inlet of the test model, see section 2.3.2. As described in section 2.5.3, this approach is not practical for rotating tests. Instead, a new stationary bypass valve unit was built and positioned near the first rotary union. It controls the air supply to the rotor and to the test model and allows to switch between two separate air flows: the tempering air and the test air. The bypass valve unit consists of six fast switching stainless steel flange valves[24] that can be individually controlled. They are connected by stainless steel pipe bends and T-connectors, as illustrated in the schematic drawing in figure 3.6b. Figure 3.6a shows the bypass valve unit integrated in an aluminum framework on the test rig.

Since the passages between the valve unit and the test model are comparatively long, a warming of the test air on its way to the model inside the shaft and the rotor arm must be expected. Especially for experiments with low mass flow rates, the resulting fluid temperature change may differ considerably from an ideal fluid temperature step change and may therefore be insufficient. Precooling the supply pipes inside the shaft and the rotor arm is a means to

[23] from Geobrugg AG
[24] from Schubert & Salzer Control Systems GmbH type 7032

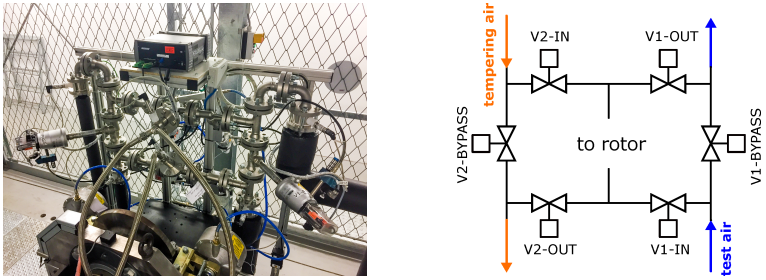

(a) (b)

Figure 3.6: Bypass valve unit: (a) installation in aluminum framework on the test rig, (b) schematic drawing of valve interconnection

minimize unwanted heating of the fluid. Therefore, these pipes are designed as heat exchangers, as shown in figure 3.7. They are made of three integrated

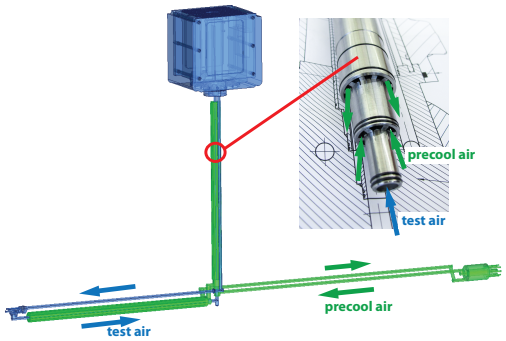

Figure 3.7: Internal routing of heat exchanger pipes

pipes. The central pipe leads the test air to the model. The outer pipes form a secondary air circuit that is not connected to the test model section. This circuit is supplied with precool air through the second rotary union, in order to precool the central main passage before the start of the experiment. This conditioning phase can take up to two hours, depending on the required test parameters and targeted test air temperatures. In this phase, cold air from the precooled center pipe must be prevented from entering the model. Especially during the start-up of the rotor, centrifugal forces would pump the cold air with its higher density radially outwards towards the model. This would lead

to unintended cooling of the model and corrupt the required isothermal initial condition. For this reason, tempering air is passed through the rotor and through the model in the reverse flow direction, during the conditioning phase, see figure 3.8a.

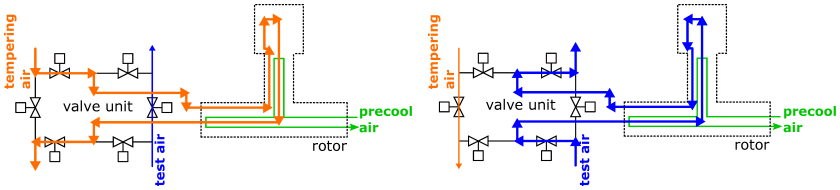

(a) Conditioning (b) Experiment

Figure 3.8: Bypass valve unit setting for conditioning state and experiment state

The temperature of the tempering air is set to the measured (ambient) start temperature of the model to ensure an isothermal initial condition for the experiment. The pressure of the tempering air is set to the targeted pressure of the test air for the experiment to prevent a pressure jump when switching from conditioning state to experiment state. The mass flow rate for the tempering air is set to a minimum to avoid excessive reheating of the precooled supply passages while simultaneously ensuring a continuous venting of the test air supply passage in the reversed flow direction.

During the conditioning phase the test air is continuously flowing in bypass mode (see figure 3.8a) to precool the supply lines between air supply system and bypass valve unit. The valve unit is equipped with several temperature and pressure measuring points to monitor the conditioning procedure and to assess if the required boundary conditions to conduct the experiment have been reached.

The experiment starts by switching all six valves simultaneously to put the tempering air in bypass mode and to lead the cold test air in the originally intended flow direction through the rotor and through the test model, see figure 3.8b. Figure 3.9 shows exemplary fluid temperature histories for two experiments: one with an extremely low mass flow rate $\dot{m} \approx 2.4\,\mathrm{g/s}$, and one with a comparatively high mass flow rate $\dot{m} \approx 19.4\,\mathrm{g/s}$.

These fluid temperature measurements were obtained by the inlet thermocouple (T01) of a model (ROT-B, see section 3.2.5) with a hydraulic diameter of $d_{h1} = 15\,\mathrm{mm}$ for the inlet passage. Both experiments were conducted with the

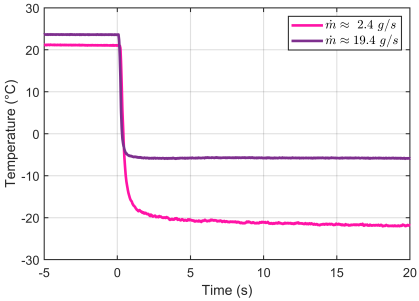

Figure 3.9: Exemplary fluid temperature step changes for different mass flow rates, measured at the model inlet (T01)

same TLC type with an indication temperature of $T_{TLC} = 1.93\,°C$. The fluid inlet temperatures were individually adjusted for each experiment in order to attain suitable TLC indication times. Therefore, the conditioning phases for both experiments differed considerably. For the experiment with the low mass flow rate a much lower fluid inlet temperature (measured upstream of the inlet valve V1-IN at the bypass valve unit) had to be selected. It can be seen that by precooling the internal supply passages, a very fast fluid temperature step change, independent from the selected mass flow rate, can be achieved.

3.2.5 Test Model

Geometry

The test model ROT-B for the rotating experiments was derived from the stationary model STAT. The geometry was scaled down with a scaling factor of 0.759, so that the hydraulic diameter of the fist passage of ROT-B is now $d_{h1} = 15\,mm$. Furthermore, to fit inside the aluminum housing the model had to be shortened by approximately 40 %. The total length of passage 1 is 186 mm. Passage 2 has an effective length of only 149 mm, because of a 90° bend at its outlet. Correspondingly, fewer rib segments are available here. A listing of the main model parameters is given in table 3.2.

A CAD representation of the fluid domain is given in figure 3.10a. An illustration of a possible positioning of this generic cooling channel configuration within a turbine blade contour is shown in figure 3.10b. This figure also shows the orientation of the geometry with respect to the rotation axis. In this thesis

Table 3.2: ROT-B model parameter

	pass 1	pass 2
shape of cross-section	trapezoidal	rectangular
hydraulic diameter d_h (mm)	15.00	19.89
length of passage L (mm)	186	149
rib angle γ	60°	60°
rib pitch p / hydraulic diameter d_h	1.0	1.0
rib height e / hydraulic diameter d_h	0.1333	0.1333
rib width b / hydraulic diameter d_h	0.1	0.1
rib offset between SS and PS / rib pitch p	0.5	0.5
number of SS ribs	11	8
number of PS ribs	10	7

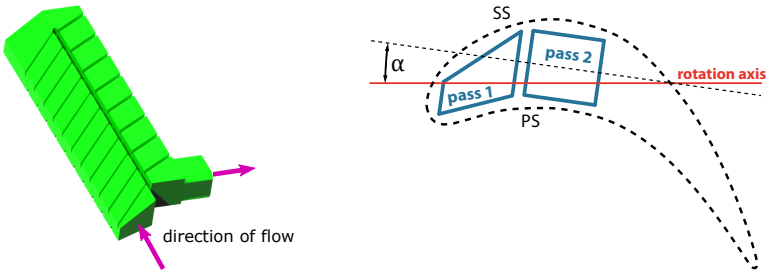

(a) (b)

Figure 3.10: ROT-B model: (a) CAD representation of fluid domain, (b) Illustration of channel cross-section inside blade contour and orientation of geometry with respect to the rotation axis (bottom view)

the model angle is defined as the angle between the rotation axis and the SS and PS sidewalls of pass 2 in a projected view along the channel main axis. For the presented test campaign a model angel of $\alpha = 8°$ was chosen.

Perspex Model

The model is manufactured out of Perspex. Figure 3.11a shows the four main parts: the two half-shells for the ribbed PS and SS sidewalls, the divider web, and the tip wall. The inner channel walls are then coated with TLCs[25]

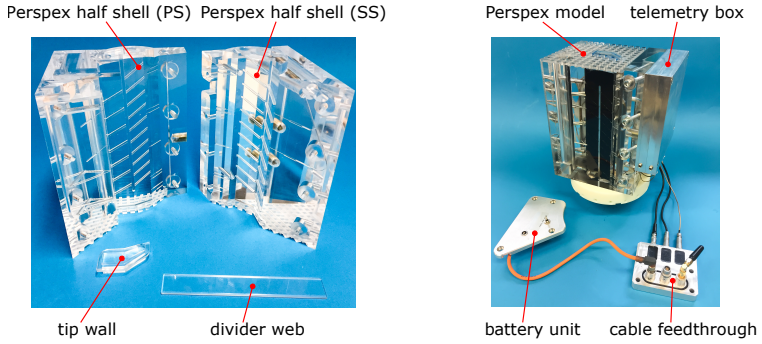

(a) (b)

Figure 3.11: ROT-B model: (a) Perspex model parts, (b) TLC coated and instrumented model with attached telemetry system

and black contrast paint. Subsequently, the model is instrumented with thermocouples and pressure sensors. After that, the divider web and the tip wall are positioned and the two half shells are screwed together. Figure 3.11b shows the instrumented and assembled model together with the rotating part of the telemetry system.

Thermocouple Instrumentation

The fluid temperature development is measured with 15 thermocouples that are positioned along the test channel, as shown in figure 3.12b. The custom-designed type K thermocouples[26] are reinforced with capillary tubes on a length

[25] from LCR Hallcrest LTD. type SPN100/G0C1W
[26] from Thermoexpert type 1KV025/27/KR0,5-25/IM/D2,5/TKK09/1m

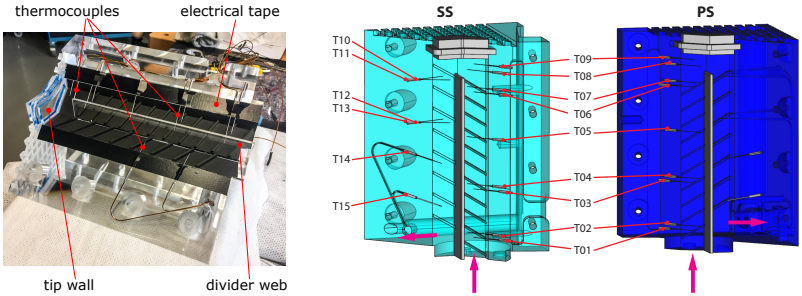

(a) Mounting (b) Positions

Figure 3.12: Thermocouple instrumentation

of 25 mm to prevent excessive bending due to centrifugal forces. At the tip, the diameter is reduced to 0.25 mm to ensure fast response times that are required for the transient measurement method. The thermocouples (T01...T09, T14, T15) are positioned in respective grooves inside the contact surfaces between the two half-shells and held in position by electrical tape[27], as shown in figure 3.12a. During assembly of the model, the thermocouples are wedged in, while the electrical tape acts as sealing between the two half-shells. The thermocouples (T10...T13) are mounted through boreholes in the PS half-shell and sealed with hot-melt adhesive, as described in section 2.2.4 for the stationary model. As with STAT, the thermocouples are arranged either as single sensors or as sensor pairs.

Three additional thermocouples (T16, T17 and T18) are installed in blind boreholes inside the PS half-shell to measure the Perspex temperature. These boreholes are orientated normal to the unribbed trailing edge (TE) of pass 2 and end 1 mm to 3 mm underneath the surface. Before inserting the thermocouples, the bore holes were filled with heat sink grease[28] to ensure effective heat conduction.

Pressure Sensor Instrumentation

The fluid pressure development is measured with four absolute pressure sensors[29] with a measuring range of 0 bar to 17 bar. The measurement principle

[27] from 3M type Temflex 1500, vinyl plastic electrical tape
[28] from Chemtronics type CircuitWorks CT40-5
[29] from Kulite Semiconductor Products, Inc. type XCL-152-17barA

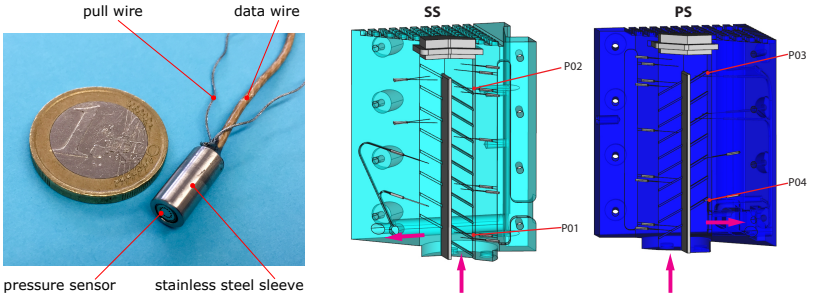

(a) Sensor (b) Positions

Figure 3.13: Pressure sensor instrumentation

of these sensors is based on the piezoresistive effect. Mechanical pressure on a semiconductor diaphragm causes a change of its electrical resistivity, which is measured via a integrated Wheatstone bridge circuit. These sensors are therefore equipped with four wires: two for the 10 V DC excitation, and two for the signal output voltage (100 mV full scale output). The sensors are installed inside stainless steel sleeves to protect them from mounting stresses, as shown in figure 3.13a. They are mounted inside blind boreholes and sealed with hot-melt adhesive. The blind bores are connected to the test channel with through bores with a diameter of only 0.7 mm. These pressure taps are perpendicular on the respective channel surface, i.e. the leading edge in pass 1 and the unribbed back wall in pass 2. Figure 3.13b shows the sensor positions: near the inlet (P01), upstream of the bend (P02), downstream of the bend (P03) and upstream of the 90° bend at the outlet (P04). Pull wires are attached to the steel sleeve to allow the sensors to be retrieved again from the boreholes.

Telemetry System

The custom-designed radio telemetry system[30] provides 22 temperature and 6 pressure channels. The rotating part consists of a sensor signal amplifier (SSA) installed inside an aluminum box, a cable feedthrough and a battery unit, as shown in figure 3.11b. The stationary receiver is shown in figure 3.14c.

Figure 3.14a shows the sensor signal amplifier mounted to the Perspex model. The thermocouples and pressure sensors are plugged to the pin connector. A

[30] from Ingenieurbüro Manner

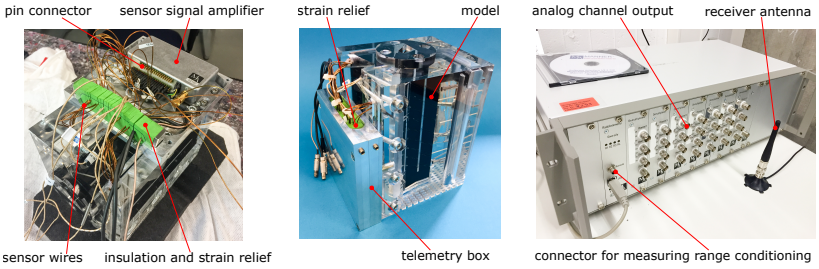

Figure 3.14: Telemetry system: (a) Sensor signal amplifier sensor connection and wiring, (b) Telemetry box mounted to Perspex model, (c) Receiver

slitted vibration damping plate[31] is used for strain relief for the sensor wires. After closing the telemetry box, the damping plate is compressed using screws on the side of the box in order to fixate the wires, see figure 3.14b. The main purpose of the box is to insulate the sensor signal amplifier against fast temperature changes, as this would influence the temperature measurements. Even though the sensor signal amplifier is equipped with cold junction compensation, using a reference temperature sensor[32] inside its housing, this setup cannot compensate fast temperature changes. Therefore, the sensor signal amplifier is kept at a constant temperature as best as possible for the duration of the experiment. For validation the cold junction temperature is monitored inside the telemetry box with a thermocouple (T19) positioned near the pin connector. The complete telemetry measurement chain is illustrated in figure 3.15.

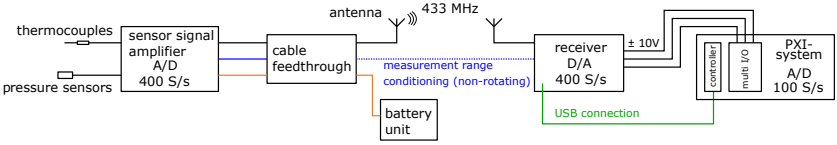

Figure 3.15: Telemetry measurement chain

Three cables connect the sensor signal amplifier with the cable feedthrough, which provides the corresponding connectors on the outside of the model housing (see figure 3.18b). The transmitting antenna is directly plugged to the top connector. The middle connector provides remote access to the sensor

[31] from AirLoc AG type 715
[32] from Texas Instruments type LM60

signal amplifier for measurement range conditioning at standstill of the rig. During the experiment this connecter is vacant. The bottom connector is connected to the battery unit, which is mounted to the underside of the model housing. The battery unit uses a NiMH rechargeable battery with a capacity of 1000 mA h to allow continuous operation of the telemetry system for up to six hours.

The sensor signal amplifier employs individual A/D converters for a synchronized digitization of all channels with a resolution of 16 bit and a sample rate of approximately 400 samples/s. The sensitivity of the amplifier can be adjusted between 0.1 mV/V and 12 mV/V for each channel individually. At a sensitivity of 1 mV/V the zero drift is stated with $< 0.02\,\%/\mathrm{K}$. The digitized data are then transmitted as a coded signal at a radio frequency of 433 MHz. The receiver is equipped with four antennas for an optimal reception through antenna diversity. Individual D/A converters for each channel convert the digital values back to analog voltage signals onto a range of $-10\,\mathrm{V}$ to $+10\,\mathrm{V}$ for the temperature data and onto a range of $0\,\mathrm{V}$ to $+10\,\mathrm{V}$ for the pressure data. These signals are then measured with a sampling rate of 100 samples/s using a multifunction measurement I/O module[33] of a PXI-system.

Sensor Calibration

For the calibration of the sensors the complete measuring chain, as illustrated in figure 3.15, was taken into account. Using the remote conditioning function, the measuring range of the telemetry system was adjusted to the value range expected to occur during the experiment. For this, the gain-values (sensitivity) and the zero points of the sensor signal amplifier can be set individually for each of the 28 channels. However, for each channel category the same values have been used in this thesis. That means, all temperature channels are configured identically. Similarly, all pressure channels are configured with the same gain and zero point values.

This way, the thermocouple channels are set up to cover a temperature range of $-40\,^{\circ}\mathrm{C}$ to $+50\,^{\circ}\mathrm{C}$, which is then mapped with a 16 bit resolution onto a range of $-10\,\mathrm{V}$ to $+10\,\mathrm{V}$ for the analog signal output of the receiver, as shown in figure 3.16a.

The temperature measurement calibration was performed by using a dry-block calibrator[34] that can be operated in a temperature range of $-100\,^{\circ}\mathrm{C}$ to $+155\,^{\circ}\mathrm{C}$.

[33] from National Instruments type NI-PXIe-6345
[34] from Ametek Denmark A/S type RTC-159 B

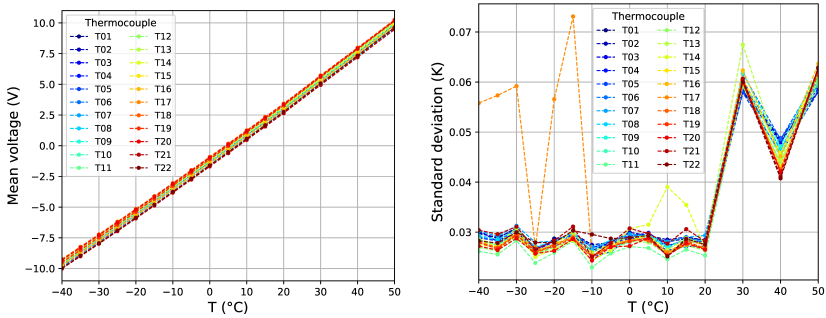

(a) Calibration curves

(b) Standard deviation

Figure 3.16: Thermocouple calibration

All thermocouples have been fitted inside an aluminum cylinder together with the temperature reference sensor[35] and the dynamic load compensation sensor[36] of the dry-block calibrator. The cylinder is then inserted into the calibrator. With this setup, measurement accuracies of $\pm 0.03\,\mathrm{K}$ for the reference temperature can be achieved. The temperature range was then passed through in steps of $5\,\mathrm{K}$ for $T < 20\,^{\circ}\mathrm{C}$ and in steps of $10\,\mathrm{K}$ for $T > 20\,^{\circ}\mathrm{C}$. At each temperature step, steady-state conditions and temperature stability have been verified by the calibrator, before acquisition of the calibration point. For each thermocouple a fixed number of 1000 samples of the receiver's voltage signal output are acquired at a rate of 100 samples/s. The resulting calibration curves in figure 3.16a show the mean values of these measurements.

The calibration curves are then stored as look-up tables in the instrument driver[37] of the measurement I/O module. Thus, to each measured voltage a corresponding temperature can be assigned by linear interpolation between the support points of the look-up table. Figure 3.16b shows the standard deviation determined from the 1000 samples for each thermocouple. In the temperature range of $-40\,^{\circ}\mathrm{C}$ to $+20\,^{\circ}\mathrm{C}$, which is the relevant range for the presented experiments, the standard deviation stays below $0.04\,\mathrm{K}$, with the only exception of thermocouple T17.

[35] from Ametek Denmark A/S type STS-200 A 917
[36] from Ametek Denmark A/S type DLC-159
[37] from National Instruments type DAQmx

The pressure channels are conditioned to cover a measurement range of 0 bar to 12 bar. This range is then mapped onto a range of 0 V to +10 V for the analog signal output of the receiver, as shown in figure 3.17a.

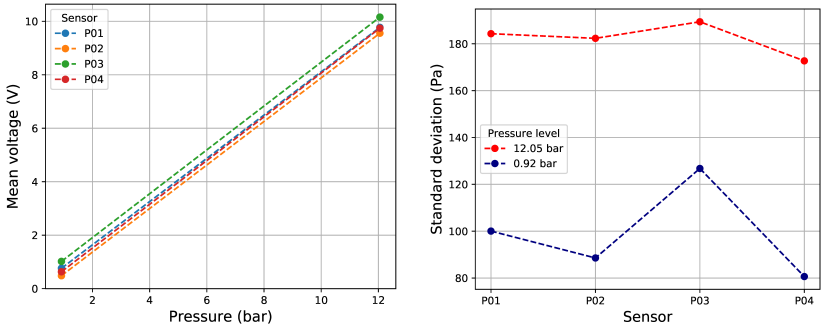

(a) Sensitivity calibration

(b) Standard deviation

Figure 3.17: Pressure sensor calibration

In contrast to the temperature calibration, the pressure calibration is performed only at two extreme points (at 0.92 bar and at 12.05 bar) to determine the sensitivity of the pressure measurement chain. Only the gradient of the linear calibration curve is determined, because a zero point drift has to be expected for the pressure sensors. In post-processing of each experiment, the zero point offset between the sensors is corrected.

Calibration was performed by connecting all sensors, together with a reference sensor[38], to a common pressure plenum. The plenum pressure is adjusted using a nitrogen pressure bottle. Again, after steady state conditions are reached, for each sensor a fixed number of 1000 samples of the receiver's voltage signal output are acquired at a rate of 100 samples/s. The mean values of theses measurements are presented in figure 3.17a. These calibration points are stored in the instrument driver of the measurement I/O module, so that to each measured voltage a corresponding pressure value is assigned. The standard deviations are below 190 Pa (0.016 % of full scale output) for all sensors, as shown in figure 3.17b.

[38] from Omega Engineering type PXM319-015AI

Model Housing

The model housing consists of two aluminum half shells, see figure 3.18a.

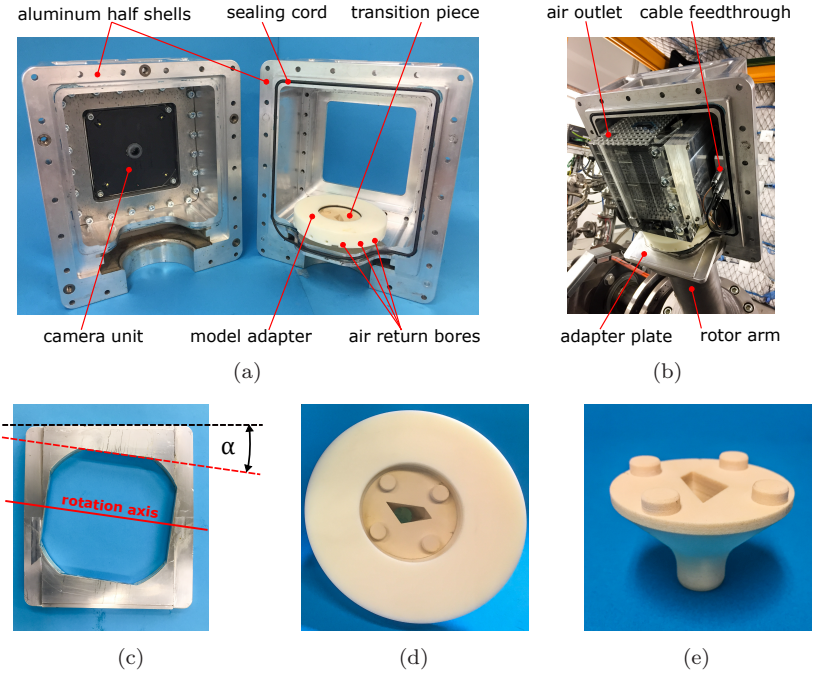

Figure 3.18: Model housing and components: (a) aluminum half-shells, (b) SS half-shell on rotor arm with installed model, (c) adapter plate, (d) model adapter with inlet transition piece, (e) 3D-printed inlet transition piece

It is mounted to the rotor arm with a form-fit connection. The orientation of the housing with respect to the rotation axis is defined by an adapter plate, see figures 3.18b and 3.18c. The adapter plate is interchangeable, so that for each required model angle a respective adapter plate can be chosen. For the presented experiments in this thesis an adapter plate with an angle of $\alpha = 8°$ has been used.

After the first housing half-shell is sled onto the end of the rotor arm, the Perspex model is inserted and positioned on a model adapter[39] which connects the air supply pipes of the rotor arm with the model. The model adapter holds an interchangeable transition piece[40], see figures 3.18d and 3.18e. This component is 3D-printed, using a laser-sintering process, and ensures a smooth transition between the supply pipe with the circular cross-section and the model inlet with the trapezoidal cross-section. For models with a different inlet geometry, a respective new transition piece must be printed.

The three cables of the telemetry box are then connected to the cable feed-through. Subsequently, the housing can be closed by sliding the second half-shell onto the rotor arm and screwing both housing parts together. By doing so, two wooden wedges (not shown) on top of the model brace the model in its position. The half-shells are sealed against each other with a sealing cord, see figure 3.18a

After the test air passes the test channel, it exits the model at the air outlet at the top, see figure 3.18b. The test air then pressurizes the model housing. This way, the Perspex model itself is only exposed to low differential pressures, even at high operating pressures of up to 10 bar. The test air is led back to the return pipe in the rotor arm through air return bores in the circumferential surface of the model adapter, see figure 3.18a.

3.2.6 Optical Access and Lighting

Each housing half-shell holds a camera unit to allow a direct and simultaneous observation of the suction sidewall and pressure sidewall. The camera unit consists of a modified commercial action camera[41], lighting and signal LEDs, IR receiver and batteries integrated in an aluminum plate, see figure 3.19.

The camera records with a Full HD progressive scan resolution of 1920 x 1080 pixels at a frame rate of $\nu_{fps} = 30$ fps. The video recording is stored with a MPEG-4 AVC / H.264 compression on an internal micro SD memory card. A 145° wide angle lens allows a camera position very near to the model. Camera lens and sensor are encapsulated and covered by protective glass. This way, possible deformations and thereby video distortions due to operating pressures of up to 10 bar are prevented.

[39] made from PA6 G
[40] from IGUS type iglidur I3
[41] from MOBIUS

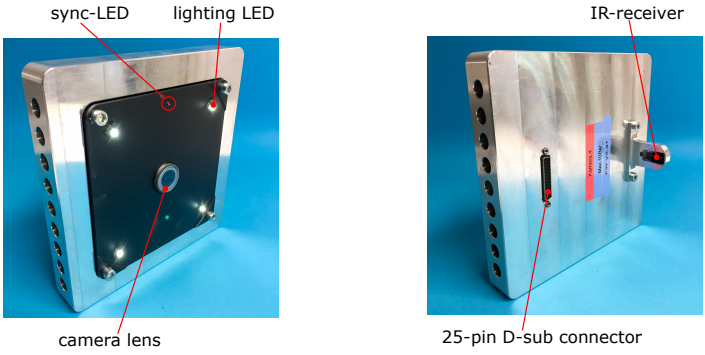

(a) Front (b) Back

Figure 3.19: Camera unit

Four white LEDs[42] with a color temperature of 6500 K are positioned in the corners of the unit providing a homogenous illumination of the model. A single red LED, which is visible in the video through reflection in the Perspex model, is used for synchronization of the video with the fluid temperature measurements. The switching of this sync-LED is timed with external data acquisition, so that the video and temperature measurements can be synchronized in post-processing. Camera and LEDs are activated remotely via a coded IR signal. The IR receiver is positioned on a small cantilever mounted on the back of the unit, see figure 3.19b. This ensures an unobstructed line of sight between IR transmitter and receiver independent from the orientation of the model housing or position of the rotor arm.

The camera unit is powered by four batteries[43] with a total capacity of 9600 mA h. A 25-pin D-sub connector provides the USB interface for the configuration of the camera settings and for downloading the videos from the internal memory card. Recharging of the batteries is also done via this connector. A matt black coating reduces reflections in the Perspex model.

3.2.7 Synchronization and Data Management

For the evaluation of the experiment the synchronization of the video data with the fluid temperature data is essential, as the method is based on measuring the

[42] from Lumileds Holding B.V type Luxeon Rebel
[43] type LiFePo4

delay between an excitation (fluid temperature step change) and the according response (TLC indication). This synchronization can be achieved within the uncertainty of approximately one video frame ($\approx 33\,\mathrm{ms}$).

Auxiliary measurement data such as mass flow rates and the rotation speed are used to determine the test parameters (Reynolds number, rotation number...) and boundary conditions (room temperature, control valve positions...) of the experiment. These data can be synchronized with an uncertainty of approximately 100 ms.

Video Synchronization

The PXI-system is the main device for measurement data acquisition (telemetry data, switching valve positions and pressures of valve unit), as well as the basis for the test rig control (switching valves control, camera and lighting control). It consists of a chassis[44], in which several data acquisition cards are plugged in. The system is controlled using a controller module running a Microsoft Windows operating system. All PXI measurement modules are connected via a communication bus and additionally via a dedicated timing and synchronization bus and are configured to use a common time base.

The test rig control program is written in LabVIEW. Using a PXI-counter/timer module[45], the trigger signals for the valves, cameras, and LEDs are generated. Simultaneously with the start trigger, an IR-signal is sent to the camera unit to switch off the sync-LED to get a temporal reference point in the video recording. In order to be able to synchronize the video with external measurements, the delay between the trigger signal and the actual time at which the sync-LED light goes off, needs to be determined. For this a preliminary test was set up, as illustrated in figure 3.20a. Using a photo diode[46], the intensity of the LED light is measured. The signal output of the photo diode, as well as the trigger signal are measured with an oscilloscope. The result for a test, where the sync-LED was switched on, is given in figure 3.20b. The delay between the trigger signal and the sync-LED response was determined with a high repeatability to $t_{syncLED} = 94\,\mathrm{ms}$.

The trigger signal also marks the start for the valve unit to switch from the conditioning state to the experiment state, see figure 3.8. Two inductive proximity sensors[47]per each valve check the valve position status. The sensor

[44] from National Instruments type NI PXIe-1065
[45] from National Instruments type NI-PXI-6602
[46] from ThorLabs type DET10AM, response time $< 2.3\,\mathrm{ns}$
[47] from IFM type IN5121

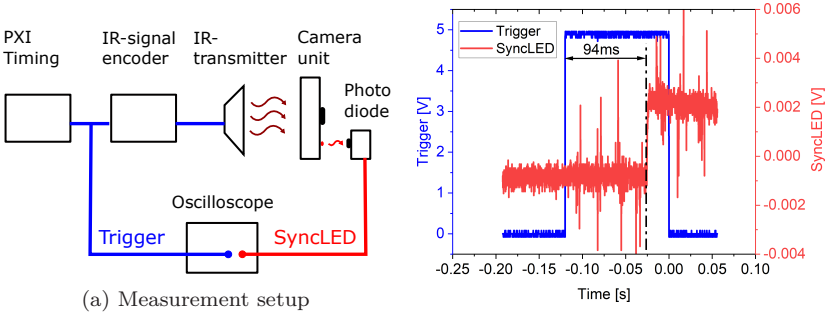

(a) Measurement setup

(b) Oscilloscope measurement

Figure 3.20: Delay measurement between trigger and sync-LED response

signals are acquired with the same PXI I/O measurement module that is also used to acquire the telemetry data. This way, the time the valves take to fully open was determined to $t_{open} \leq 80\,\text{ms}$ and the time to fully close to $t_{close} \leq 60\,\text{ms}$.

While the delay for the sync-LED always has a fixed value, the delay of the fluid temperature change t_{ftc} depends on the test parameters such as mass flow rate and pressure of the test air. Figure 3.21 shows the delays for two exemplary experiments at Reynolds numbers of $Re = 7500$ and $Re = 60000$ respectively.

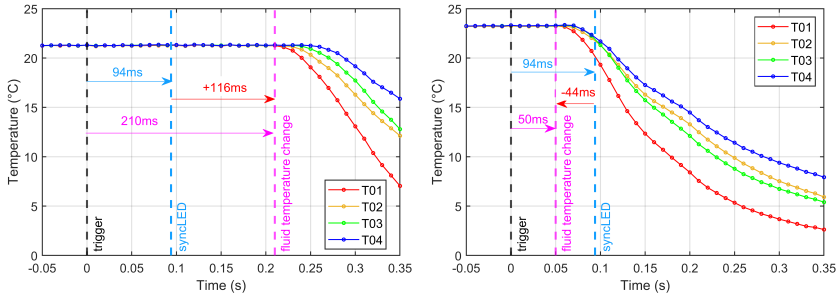

(a) $Re = 7500$; $\overline{T_f} \approx -24.15\,°\text{C}$

(b) $Re = 60000$; $\overline{T_f} \approx -1.23\,°\text{C}$

Figure 3.21: Detection of fluid temperature change for synchronization of video and fluid temperature data

Illustrated are the fluid temperature data of the first four thermocouples in the test channel in a short time frame after the trigger signal. Regarding the evaluation of the experiment, the start of the fluid temperature change defines the actual start of the experiment. This point in time with respect to the trigger signal ($t_{trigger} = 0\,\mathrm{s}$) is manually selected for every experiment individually from the fluid temperature measurements. Here, t_{ftc} is defined as the time of the measurement sample just before the first detection of a temperature change at the first thermocouple (T01). The time difference between the sync-LED and the fluid temperature change is then

$$\Delta t_{sync} = t_{ftc} - t_{syncLED} \tag{3.9}$$

For a video with a frame rate of $\nu_{fps} = 30\,\mathrm{fps}$ the time interval between two frames is $\Delta t_{frame} = \nu_{fps}^{-1} \approx 33\,\mathrm{ms}$. The time difference Δt_{sync} can then be normalized with Δt_{frame} to obtain the number of frames between the sync-LED and the fluid temperature change

$$N_{sync} = \lfloor \frac{\Delta t_{sync}}{\Delta t_{frame}} \rceil \tag{3.10}$$

where the resulting value of the normalization needs to be rounded to the nearest integer value. The video is then cut at the frame where the fluid temperature starts to change. For positive values of Δt_{sync} the video is cut N_{sync} frames after the frame where the sync-LED turns off. For negative values of Δt_{sync} the video is cut $|N_{sync}|$ frames before the frame where the sync-LED turns off.

Synchronization of Auxiliary Measurement Data

An overview of the data flow and logging procedure of the auxiliary measurement data is shown in figure 3.22.

The measurement data of the cooling air supply system such as temperatures, pressures and mass flow rates of the three air flows, as well as control valve positions, are gathered by a programmable logic controller (PLC)[48] and transferred via a ProfiNET interface to a measurement computer with the designation VRE. The electric motor is controlled via a second PLC[49]. This PLC employs a counter module[50] to evaluate the rotational speed of the rotor. It furthermore monitors the safety installations such as door closing contacts,

[48] from Siemens type SIMATIC S7-300 CPU315F-2 PN/DP
[49] from Siemens type SIMATIC S7 IM 151-8 F PN/DP
[50] from Siemens type 6ES7138

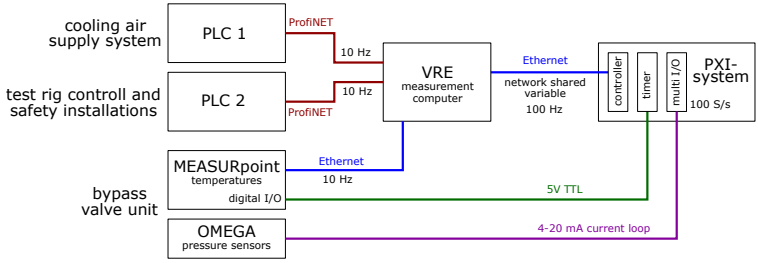

Figure 3.22: Data flow and logging procedure of auxiliary measurement data

rotor standstill detection and pressure of emergency brake line. All these data are also transferred via ProfiNET to the VRE measurement computer. The ProfiNET network provides the data of the two PLCs with a refresh rate of 10 Hz. The data logging procedure (written in LabVIEW) also logs the data at this rate to the VRE computer.

The two instances of LabVIEW running on the PXI-system and the VRE computer are synchronized via a network shared variable over an Ethernet connection. The PXI-system writes the valve unit status (bypass, conditioning or experiment) to this shared variable, which is updated with a refresh rate of 100 Hz. The variable is then read out by the VRE computer. Considering the logging rate of only 10 Hz, the latency of this synchronization method via Ethernet is negligible.

A MEASURpoint temperature measurement device[51] is employed to acquire the temperatures at six key positions of the valve unit as well as the temperatures at both rotary unions. Additionally the room temperature is logged. For this, type K thermocouples are used. The temperature data are acquired with a rate of 10 samples/s and transmitted via an Ethernet connection to the VRE computer. The device is equipped with a digital I/O port that is used for synchronization with the PXI-system. The PXI-counter/timer module provides the valve unit status (bypass, conditioning or experiment) as binary code via a 5 V TTL connection. The MEASURpoint device then logs the valve unit status simultaneously with the temperature data.

The valve unit is also equipped with six pressure sensors[52] that are positioned near the thermocouples. They are directly connected via a 4-20 mA current loop

[51] from Data Translation GmbH type MEASURpoint DT 8874-16
[52] from Omega Engineering type PXM319-015AI

to a multifunction I/O module[53] of the PXI-system. Thus, these measurements are already synchronized via the dedicated synchronization bus of the PXI-system.

3.3 Experimental Procedure and Evaluation

In this section the test procedure and the evaluation of the test parameters of a typical experiment are described. Subsequently, additional image processing steps for the video analysis are presented. These are now required due to the new observation concept using co-rotating cameras. Then some verification tests are presented. The temperature development inside the Perspex channel wall is measured with several thermocouples and compared to the analytical solution. Finally, a comparison between the results of two experiments performed at different test parameters but leading to similar Reynolds and rotation numbers is presented.

3.3.1 Test Procedure

Preparation and Temperature Conditioning

While the valve unit is in bypass mode, the cooling air supply system is turned on to cool down the heat exchanger and the test air supply lines up to the bypass valve unit. After the heat exchanger has reached its operating temperature, the generated cold air is sufficiently dry. A part of this air is electrically reheated and used as tempering air. The target temperature for this tempering air is set to the temperature measured at the Perspex model (thermocouples T16, T17 and T18). When the target temperature is reached, the bypass valve unit is switched to conditioning mode to fill the air passages inside the rotor and the model with dry tempering air. Now that any possible moisture has been removed from the internal air supply line, potential condensation issues are prevented and the precooling air can now also be directed through the rotor in order to cool down the supply line.

As the rotor is still at standstill and the model is fixed in an upright position, the valve unit may be switched back into bypass mode. The trapped air in the supply line cools down, but does not rise to the model due to natural convection. Of course, if the targeted start temperature of the model differs from the current model temperature, the valve unit has to be operated in conditioning mode to

[53] from National Instruments type NI-PXI-6238

temper the model accordingly. However, for all experiments in this thesis the targeted start temperature for the model was set to the model temperature that was measured prior to conditioning, as described above. Depending on the test parameters, the conditioning phase may take up to two hours. In the meantime, the camera units are configured and put into standby mode. After that, the test rig is prepared to start up the rotor.

Start Up Procedure

Before the rotor is started, the bypass valve unit is switched to conditioning mode to lead the tempering air in the reversed direction through the model. The mass flow rate should be set very low, to prevent excessive reheating of the continuously cooled supply line. However, the pressure of the tempering air should correspond to the targeted test air pressure to avoid pressure jumps when switching from conditioning mode (tempering air) to experiment mode (test air). When the target temperature for the test air is reached, the rotor is speeded up according to a predefined speed ramp. During this phase, the values of the vibration velocity sensors are continuously monitored. After reaching the target value, the rotation speed is kept constant for the duration of the experiment.

Experiment

The experiment is started by switching the bypass valve unit from conditioning mode to the experiment mode. The cold test air is directed through the model, where the cooling of the channel walls is then indicated by the TLC color play. Using the Bluetooth connection to the camera units, the TLC color play is monitored in real time. The experiment can be stopped as soon as all relevant areas have shown the TLC color play.

Figure 3.23 shows one exemplary video-frame of an experiment with a rotational speed of 403 rpm. The corresponding frames of the camera units are displayed in the top left corner. Furthermore, the fluid temperature development at the inlet, bend and outlet are displayed in the bottom left corner. The round instruments on the right hand side show the current rotational speed, the current g-force at the mean model radius and some motor telemetry data.

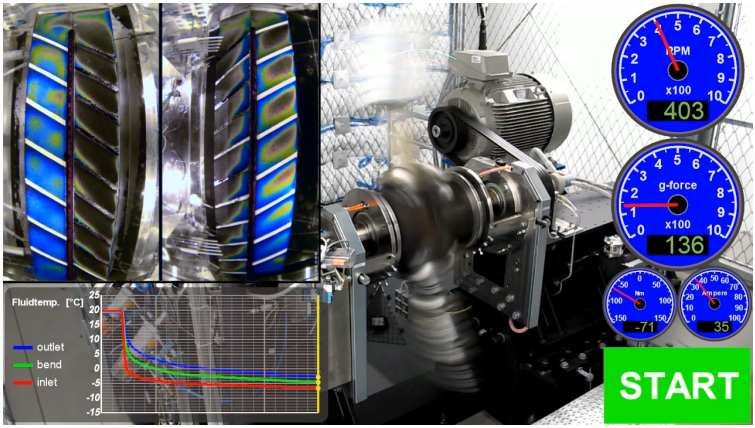

Figure 3.23: Video frame of rotating experiment with measurement data overlay

Shutdown

The rotor is braked to a complete standstill with the electric motor. The three air flows are stopped and the air passages of the rotor are vented. Subsequently, the video recordings are downloaded from the camera units and copied together with the remaining measurement data to a network attached storage.

3.3.2 Test Parameter Evaluation

This section describes the evaluation of the test parameters for an exemplary experiment with the test model ROT-B (hydraulic diameter of pass 1: $d_{h1} = 15\,\text{mm}$, cross-section area of pass 1: $A_1 = 291\,\text{mm}^2$). The target parameters for this experiment are listed in table 3.3.

Figure 3.24 shows the main control and measurement points for the test air. The mass flow rate is measured by a Coriolis mass flow meter (M311). Using control valves upstream (RV312) and downstream (RV317) of the test rig, the mass flow rate and pressure level can be controlled simultaneously. Pressure and temperature of the test air are also measured upstream (P314, T313) and downstream (P316, T315) of the test rig. All these control and measurement devices are integrated in a common skid, see figure 3.5. The access to the rotor and test model is controlled via the switching valves (V1-BYPASS, V1-IN, V1-OUT) of the bypass valve unit. The temperature sensor T1-IN directly

Table 3.3: Target parameters

Symbol	Description	Value	Unit
$\dot{m}$	mass flow rate	9.70	g/s
p	fluid pressure (at model inlet)	6.00	bar
T_f	fluid temperature (at model inlet)	-6.00	°C
n	rotational speed	802	rpm
Re	Reynolds number	30000	-
Ro	rotation number	0.300	-
Bo	buoyancy number	0.457	-

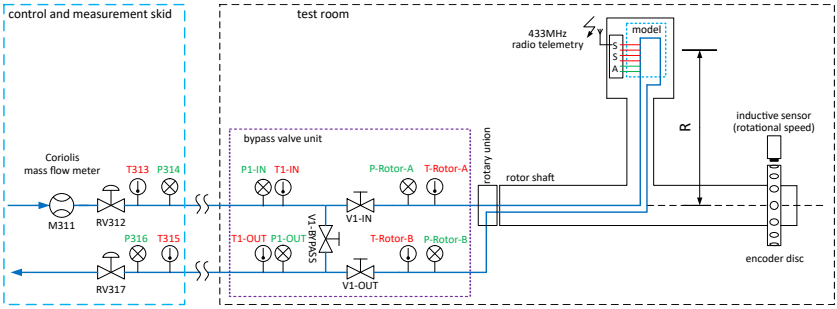

Figure 3.24: Main control and measuring points of test air

upstream of V1-IN is used during the conditioning phase to assess if the test air supply lines upstream of the bypass valve unit are sufficiently cooled and whether the experiment can be started. Finally, during the experiment, the fluid temperatures and fluid pressures along the test channel are acquired with the sensor signal amplifier (SSA) of the radio telemetry system.

Figure 3.25 shows some results of these measurements. The speed up procedure is illustrated in figure 3.25a. The rotational speed n is increased with a constant acceleration of $\dot{n} = 600\,\mathrm{rpm/s}$ until the target speed is reached. During the experiment, the rotational speed is kept constant. The angular velocity Ω is determined from the rotational speed as follows

$$\Omega(t) = \frac{n(t) \cdot 2\pi}{60} \qquad n \text{ in rpm, } \Omega \text{ in rad/s} \tag{3.11}$$

Start and end of the experiment are marked with dashed lines. The remaining diagrams focus only on this time frame.

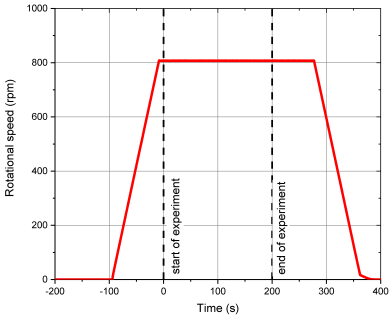

(a) Rotational speed

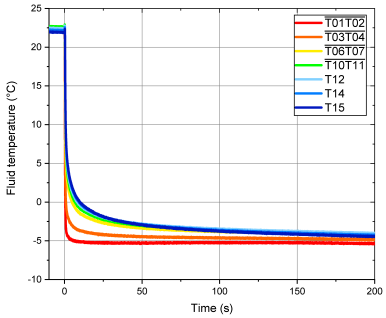

(b) Fluid temperature

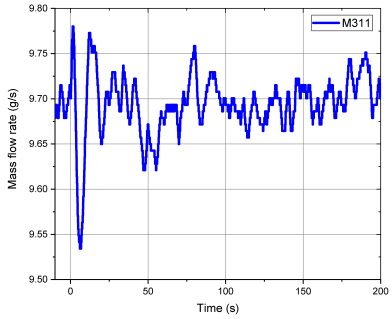

(c) Mass flow rate

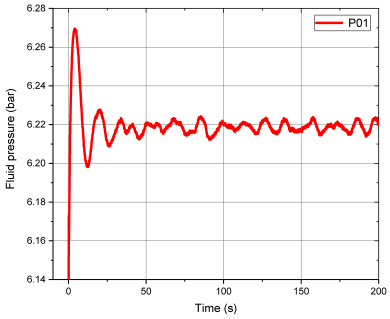

(d) Fluid pressure

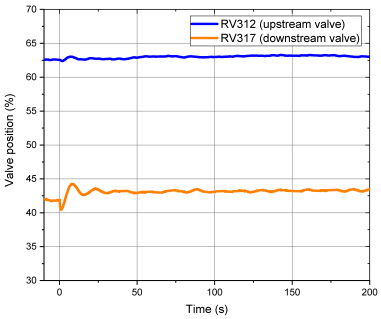

(e) Control valve positions

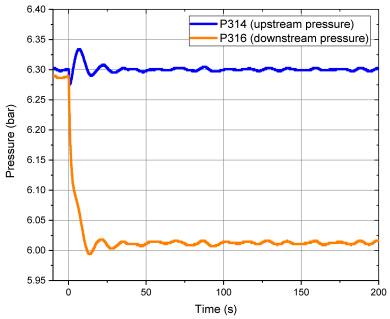

(f) Pressure loss

Figure 3.25: Direct measurements

The fluid temperature histories are shown in figure 3.25b. For thermocouple pairs (e.g. T01 and T02, see figure 3.12b) the respective mean values ($\overline{\mathrm{T01T02}}, \overline{\mathrm{T03T04}}, ...$) are presented. The fluid temperature data as shown here are also the basis for the fluid temperature field interpolation (compare section 2.4.2).

The test parameters are evaluated at the inlet of the test channel. So for all derived parameters that are influenced by the fluid temperature only the mean value of the first thermocouple pair is taken into account:

$$T_f(t) \mathrel{\widehat{=}} \frac{T_{T01}(t) + T_{T02}(t)}{2} \tag{3.12}$$

Accordingly, for all derived parameters that are dependent on the fluid pressure, only the measurement of the first pressure sensor (P01) is taken into account:

$$p(t) \mathrel{\widehat{=}} p_{P01}(t) \tag{3.13}$$

The mass flow rate and fluid pressure histories are given in figures 3.25c and 3.25d. Their curves show fluctuations which are highest at the beginning of the experiment and then gradually diminish. This can be explained by the suddenly increased pressure loss for the test air when switching from conditioning mode (or bypass mode) to experiment mode, see figure 3.25f. This change in pressure loss causes a readjustment of the control valves, as shown in figure 3.25e, in order to keep the mass flow rate and the upstream pressure constant.

The histories of some derived parameters are given in figure 3.26. The fluid density ρ at the channel inlet is determined from the ideal gas equation

$$\rho(t) = \frac{p(t)}{R\ T_f(t)} \tag{3.14}$$

where R is the specific gas constant.

The mean flow velocity u at the channel inlet with the cross-section area of A_1 is determined from the mass flow rate and the fluid density by applying the continuity equation (assuming quasi-stationary flow conditions)

$$u(t) = \frac{\dot{m}(t)}{\rho(t)\ A_1} \tag{3.15}$$

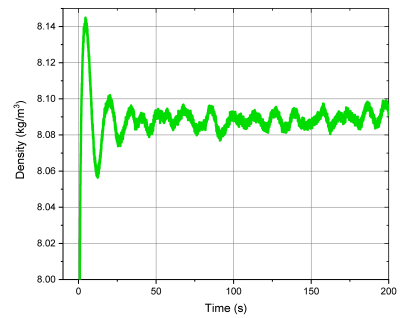

(a) Density

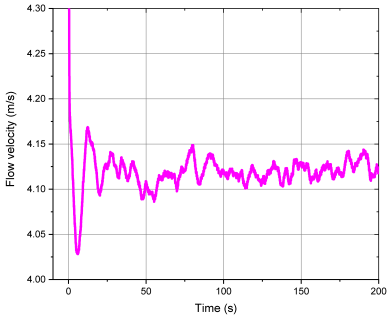

(b) Flow velocity

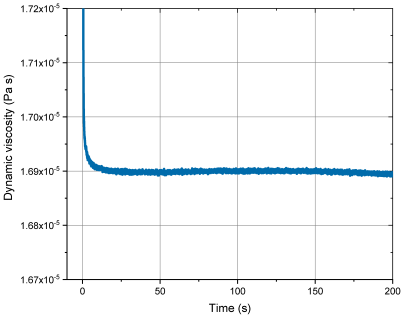

(c) Dynamic viscosity

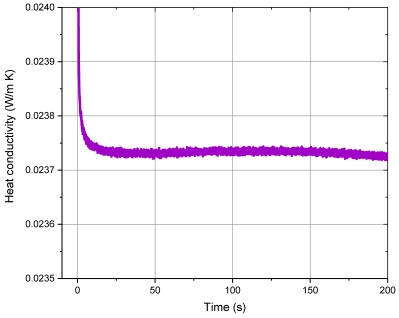

(d) Heat conductivity

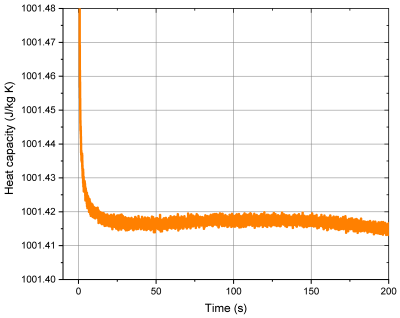

(e) Heat capacity

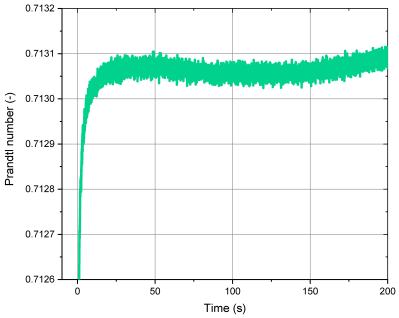

(f) Prandtl number

Figure 3.26: Derived parameters

The dynamic viscosity μ is determined from the fluid temperature using a correlation as described in section 2.3.3

$$\mu(t) = \frac{0.000001458 \cdot T_f(t)^{1.5}}{T_f(t) + 110.4} \qquad T_f \text{ in K, } \mu \text{ in Pa s} \qquad (2.18)$$

The heat conductivity of the fluid k_f is determined on the basis of equation (2.21) presented in section 2.4.3

$$k_f(t) = \left(\frac{T_f(t)}{273}\right)^{\frac{3}{2}} \cdot \frac{11.2547}{T_f(t) + 194} \qquad T_f \text{ in K, } k_f \text{ in W/(m K)} \qquad (3.16)$$

The temperature dependence of the specific heat capacity c_p is accounted for and implemented as a power series

$$\begin{aligned} c_p(t) = {} & 1052.019 - 460.384 \cdot \left(\frac{T_f(t)}{1000}\right) + 1268.248 \cdot \left(\frac{T_f(t)}{1000}\right)^2 \\ & - 1049.836 \cdot \left(\frac{T_f(t)}{1000}\right)^3 + 382.4979 \cdot \left(\frac{T_f(t)}{1000}\right)^4 \\ & - 52.38578 \cdot \left(\frac{T_f(t)}{1000}\right)^5 \qquad T_f \text{ in K, } c_p \text{ in J/(kg K)} \end{aligned} \qquad (3.17)$$

The Prandtl number is then determined from the dynamic viscosity, the heat capacity and the heat conductivity

$$Pr(t) = \frac{\mu(t)\ c_p(t)}{k_f(t)} \qquad (3.18)$$

From these measured and derived parameters the dimensionless quantities are calculated, see figure 3.27. Figure 3.27a shows the history of the Reynolds number, which is determined from the mass flow rate and the dynamic viscosity as described in section 2.3.3

$$Re(t) = \frac{\dot{m}(t)\ d_{h1}}{A_1\ \mu(t)} \qquad (2.17)$$

The history of the rotation number is shown in figure 3.27b. It is calculated from the angular velocity and the flow velocity

$$Ro(t) = \frac{\Omega(t)\ d_{h1}}{u(t)} \qquad (3.19)$$

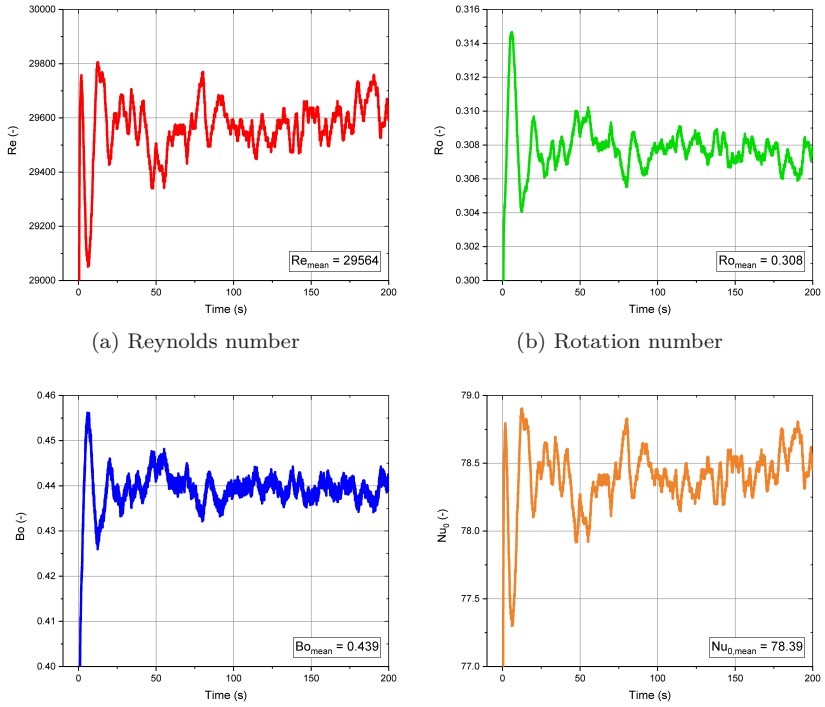

(a) Reynolds number

(b) Rotation number

(c) Buoyancy number

(d) Reference Nusselt number

Figure 3.27: Derived dimensionless quantities

Figure 3.27c shows the history of the buoyancy number which is calculated from the fluid temperature and the rotation number

$$Bo(t) = \frac{T_0 - T_f(t)}{T_0} Ro(t)^2 \frac{R}{d_{h1}} \tag{3.20}$$

where T_0 is the start temperature of the experiment.

The history of the reference Nusselt number Nu_0 is shown in figure 3.27d. It is determined by a correlation as described in section 2.4.3

$$Nu_0(t) = 0.023\, Re(t)^{0.8} Pr(t)^{0.4} \tag{3.21}$$

where an exponent of $n = 0.4$ for the Prandtl number was chosen, as the direction of heat transfer is from hot wall to cold fluid.

These time-resolved parameters are reduced to their respective mean value by time-averaging all values between start and end of the experiment. The mean values determined for this experiment are listed in table 3.4.

Table 3.4: Mean values of measured and derived test parameters

Symbol	Description	Value	Unit
$\dot{m}$	mass flow rate	9.69	g/s
p	fluid pressure (at model inlet)	6.22	bar
T_f	fluid temperature (at model inlet)	-5.20	°C
n	rotational speed	807	rpm
Re	Reynolds number	29564	-
Ro	rotation number	0.308	-
Bo	buoyancy number	0.439	-
Nu_0	reference Nusselt number	78.393	-

All dimensionless quantities stated in the results chapter refer to mean values which are determined as described here.

3.3.3 Image Processing

The videos of the TLC indications recorded with the camera units show a strong wide-angle distortion. The largest part of this effect is due to perspective distortion, as the distance between camera and test model is very short. Objects of the same size are imaged differently depending on the distance from the camera, so that objects further away from the camera appear smaller. Therefore, this effect must be particularly taken into account, if the imaged object is three-dimensional with a strong expansion into the depth of the scene.

The second contribution to the overall distortion is lens distortion. While lens distortion might be corrected rather well by a standard lens correction method implemented in e.g. Adobe® Photoshop®, GIMP or VirtualDub etc., the perspective distortion cannot be corrected by a simple transformation of the resulting image. For this, detailed 3D information of the imaged object and its position with respect to the camera would be required. Similarly, pre-calibration of the cameras with commercially available calibration plates

with regular calibration patterns is not suitable for the imaging of 3D objects or 3D surfaces.

Therefore, a different approach for the correction of the wide-angle distortion was chosen, where the distorted image is warped to match the geometry of a predefined target image. The applied dewarp algorithm *bUnwarpJ* developed by Arganda-Carreras et al. [4] performs 2D image registration based on elastic deformations represented by B-splines. This software tool is included in the open source image processing software package *Fiji* by Schindelin et al. [61]. The dewarping procedure is illustrated in figure 3.28 exemplary for the pressure side.

First, a single frame is extracted from the experiment video. This is the source image. The corresponding target image must be an image of the same pixel size. It is created from the CAD model of the test channel by choosing a projected view perpendicular onto the PS and SS surfaces of pass 2. The target geometry is positioned inside its image frame so that the best possible match with the source geometry is already achieved. In this way, the amount of dewarping required for the source image can be kept as low as possible.

Then landmarks are set at distinctive spots in the source image like intersection points between ribs and the divider web or the intersection between two outer edges. The corresponding landmarks are automatically added in the target image at the same pixel positions as in the source image. They then need to be manually dragged on the corresponding distinctive spot of the target image.

From the pixel positions of the landmarks of both images *bUnwarpJ* then calculates the warping transformation. A visual representation of the calculated distortion is given in the form of a deformation grid. The calculated transformation is then applied to all frames of the video. The resulting video can then be cropped to the relevant heat transfer surface and further processed as described in section 2.4.1.

The wide-angle correction has two main advantages for the evaluation. First, it simplifies the comparison with the results of numerical investigations, as the dimensions of both results should match. Second, it guarantees that the rib segments do not appear deformed which would adulterate the results of segment averaging. Averaging of uncorrected segments would lead to overvaluation of areas that appear stretched and to undervaluation of areas that appear compressed and thus to errors in the averaging result.

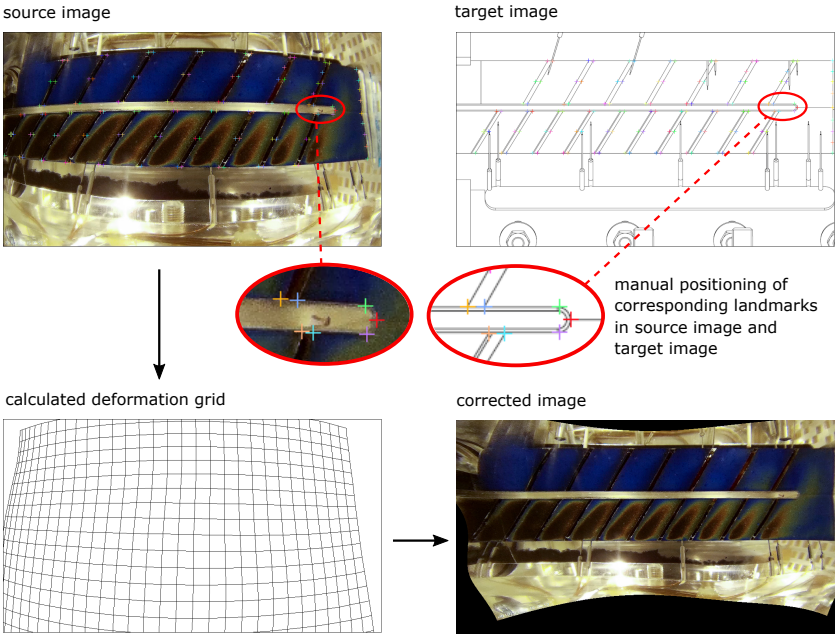

Figure 3.28: Correction of wide angle distortion (exemplary for PS)

3.3.4 Verification Tests

Verification tests have been conducted with the model ROT-A, a forerunner of model ROT-B. The cooling channel geometry and rib configuration of ROT-A is identical to ROT-B. However, the ribs have been positioned manually and fixed to the channel walls by double-sided adhesive tape. The uncertainty regarding the rib geometry is therefore higher compared to the CNC milled ribs of ROT-B. Furthermore, ROT-A is instrumented with only three fluid thermocouples, but with 10 thermocouples in different depth inside the Perspex wall. Figure 3.29 shows the positions of these thermocouples. Five thermocouples are located near the inlet and five near the bend. The respective positioning of the thermocouples is identical for these two stream wise positions. The thermocouples are mounted inside blind boreholes that end at different distances (3 mm to 15 mm) from the inner surface of suction side pass 1, see figure 3.29b. Effective heat conduction between Perspex and thermocouple is ensured by filling the boreholes with heat sink grease, before inserting the thermocouples.

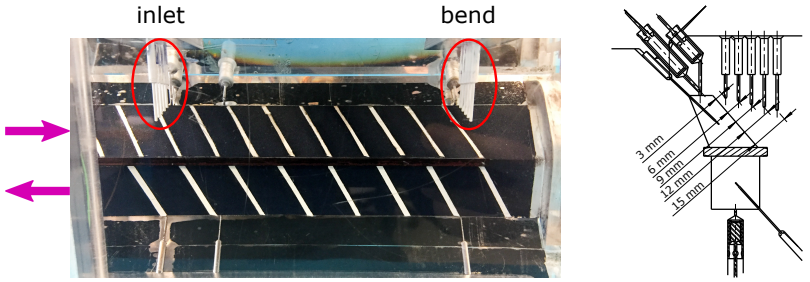

(a) View on suction side (b) Bottom view

Figure 3.29: Perspex thermocouple positions (ROT-A)

The Perspex thermocouples perform two functions. First, the isothermal status of the test model can be assessed at the start of the experiment. Evaluation of the thermocouple data for experiments with ROT-A showed that the model can be kept isothermal within an uncertainty of $\pm 0.2\,\mathrm{K}$ for rotating experiments and even within $\pm 0.1\,\mathrm{K}$ for stationary experiments, where preliminary tempering of the model is not required. Second, the validity of the semi-infinite wall assumption can be verified.

Solid Temperature Histories

Using the Perspex thermocouples, the temperature development inside the solid is evaluated. Figure 3.30a shows the histories of the differences between thermocouple measurement and the start temperature for an exemplary experiment with ROT-A.

With a mass flow rate of $\dot{m} \approx 10\,\mathrm{g/s}$ and a fluid pressure at the channel inlet of $p \approx 6.2\,\mathrm{bar}$, the mean Reynolds number for this experiment was evaluated to $Re_{mean} \approx 31400$. The start temperature was $T_0 \approx 19.9\,^{\circ}\mathrm{C}$ and the mean fluid temperature at the inlet was $\overline{T_f} \approx -7.4\,^{\circ}\mathrm{C}$. It can be seen that a faster temperature change is obtained near the bend, suggesting higher heat transfer values in this region compared to the inlet region.

At the end of the experiment ($t_{end} = 90\,\mathrm{s}$), the temperature at a depth of $z = 3\,\mathrm{mm}$ had decreased by approximately $10\,\mathrm{K}$, while the temperature at a depth of $z = 15\,\mathrm{mm}$ remained virtually unchanged. The minimum wall thickness for ROT-A is $20\,\mathrm{mm}$. Thus, for this experimental setting, the assumption of a semi-infinite wall is fulfilled.

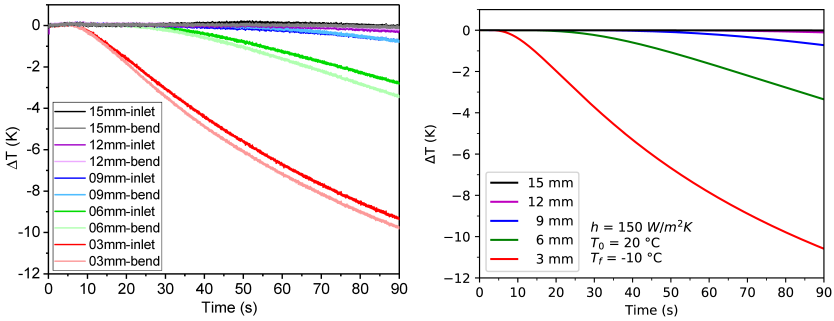

(a) Thermocouple measurement (b) Analytical solution

Figure 3.30: Temperature development at different depths inside the solid

A comparison with the analytical solution for heat conduction in a semi-infinite wall with surface convection is given in figure 3.30b. The solution was obtained by evaluating equation (2.8) with varying values for the depth z using SymPy, a Python library for symbolic mathematics. For the heat transfer coefficient a constant value of $h = 150\,\mathrm{W/(m^2\,K)}$ was chosen. The start temperature was set to $T_0 = 20\,^\circ\mathrm{C}$ and the fluid temperature or rather reference temperature to $T_f = T_{ref} = -10\,^\circ\mathrm{C}$. Regarding the material properties of Perspex the same values as specified in ProTeIn are used, see table 3.5.

Table 3.5: Material properties of Perspex

Symbol	Description	Value	Unit
ρ	density	1190	$\mathrm{kg/m^3}$
c	specific heat capacity	1470	$\mathrm{J/(kg\,K)}$
k	heat conductivity	0.19	$\mathrm{W/(m\,K)}$
a	thermal diffusivity	$1.086 \cdot 10^{-7}$	$\mathrm{m^2/s}$

The solid temperature histories show a good agreement between thermocouple measurements and analytical solution. This indicates that the presented experimental procedure is valid and that the assumptions of a semi-infinite wall and a 1D heat conduction are justified.

Verification Run

As mentioned in section 3.1, the behavior of a physical system is defined by a complete set of *dimensionless* quantities. If two systems (e.g. prototype and model) have the same numerical value for all relevant dimensionless quantities, then these two systems are dimensionally similar and their behavior can be closely correlated. Likewise, if two experiments are conducted with the same numerical values for all relevant dimensionless quantities, the obtained results should also be similar for both experiments.

This statement is verified by comparing the results of two experiments that have been conducted at similar Reynolds number, rotation number and buoyancy number, but at different *physical* test parameters, namely rotational speed and fluid pressure. The test parameters for the experiments with the identifiers V0073 and V0074 are listed in table 3.6.

Table 3.6: Test parameters for verification tests

Experiment		V0073	V0074	
Symbol	Description	Value	Value	Unit
n	rotational speed	247	397	rpm
p	fluid pressure	10.3	6.2	bar
$\dot{m}$	mass flow rate	9.9	10.0	g/s
Re	Reynolds number	31407	31764	-
Ro	rotation number	0.153	0.145	-
Bo	buoyancy number	0.117	0.105	-
Nu_0	reference Nusselt number	82.3	83.1	-

The evaluated normalized Nusselt number distributions are given in figure 3.31. They show a very good agreement between the two experiments. Consequentially, we obtain matching results for the segment averaged normalized Nusselt numbers, see figure 3.32. These results strengthen confidence in the experiments on repeatability and transferability of the results with regard to model similarity.

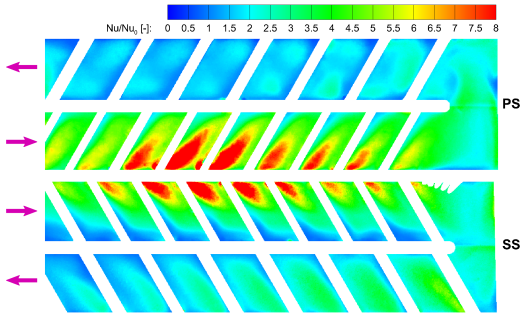

(a) V0073

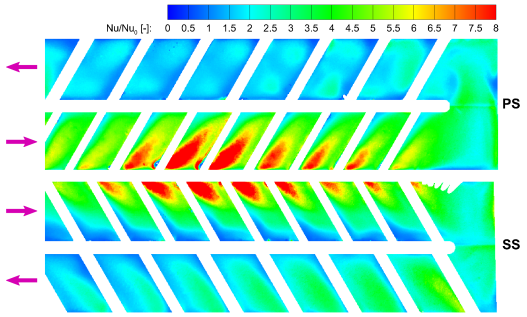

(b) V0074

Figure 3.31: Normalized Nusselt number distribution (Nu/Nu_0)

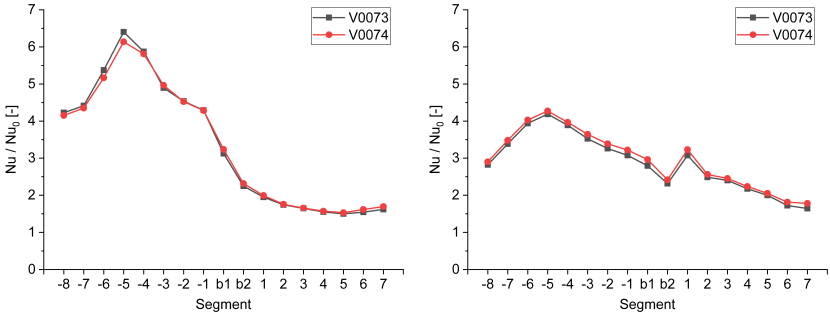

(a) PS (b) SS

Figure 3.32: Segment averaged normalized Nusselt number (Nu/Nu_0)

CHAPTER 4

Results and Discussion

In this chapter exemplary results of a measurement campaign with the model ROT-B are presented. The campaign resulted in a total of 32 evaluated experiments with varying Reynolds numbers and rotation numbers. The results are presented as local Nu/Nu_0 distributions as well as segment averaged and line averaged Nu/Nu_0 values. Furthermore, by calculating the ratio between the results of a rotating and the corresponding stationary experiment, the influence of rotation on the heat transfer distribution is directly visualized. Finally, line averaged, segment averaged, and additionally passage averaged values are plotted against the rotation number for three different Reynolds numbers. These diagrams clearly show the significant spreading of the heat transfer values with rotation, i.e. the increasing or decreasing of local heat transfer depending on the surface position and orientation of the surface with respect to the rotational axis.

4.1 Test Parameters

The model Rot-B was coated with TLCs[1] with a calibrated indication temperature of $T_{TLC} = 1.93\,°C$ and black backing paint. The TLC coating and instrumentation remained unchanged throughout the test campaign.

The experiments have been conducted with Reynolds numbers between $Re_{targ} = 5000$ and $Re_{targ} = 60000$. The rotation number has been varied between $Ro_{targ} = 0$ and $Ro_{targ} = 0.5$. As described in section 3.1.2, the buoyancy number cannot be chosen fully independently of the rotation number. At a given Reynolds number and rotation number the buoyancy number can only be varied by varying the combination of fluid temperature and start temperature. The fluid temperature, however, is mainly adjusted with respect to the start temperature and the TLC indication temperature in order to obtain suitable TLC indication times. Small variations were possible, accounting for the indication time ranges, see figure 3.1. The obtained buoyancy numbers varied between $Bo = 0$ and $Bo = 2.4$.

The diagrams in figure 4.1 show the evaluated mean values of the dimensionless quantities Re, Ro and Bo for all 32 experiments. Most data points are available for the three Reynolds numbers $Re = 7500$, $Re = 15000$ and $Re = 30000$, where the rotation number has been varied in finer steps. Therefore, only the results for these Reynolds numbers are presented in the following sections.

[1] from LCR Hallcrest Ltd. type SPN100/G0C1W Lot# 6686

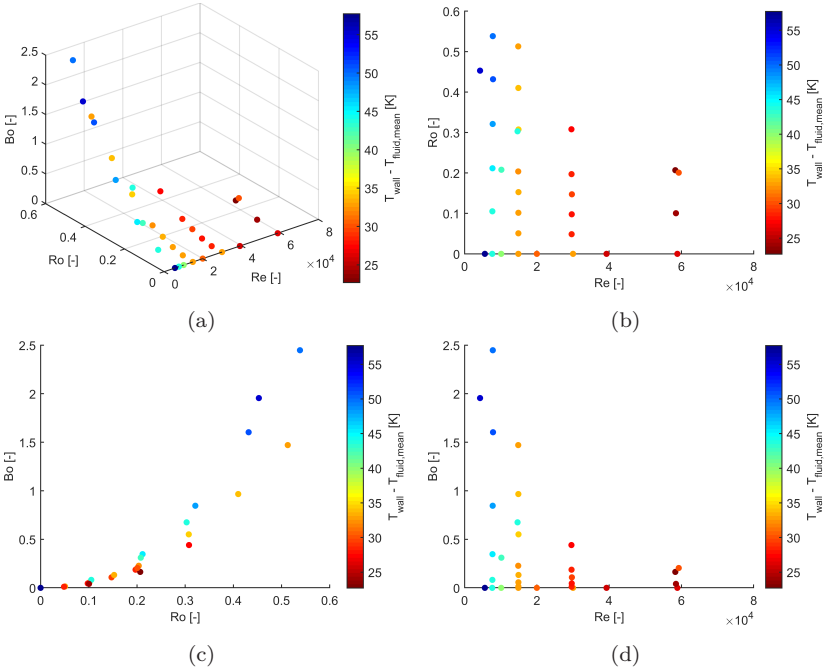

Figure 4.1: Dimensionless quantities of measurements

4.2 Heat Transfer Distribution

4.2.1 Stationary Experiments

Figure 4.2 shows the results of the stationary experiments presented as normalized Nusselt number distributions. These Nusselt number ratios represent the heat transfer enhancement of a ribbed channel compared to a smooth channel with the same hydraulic diameter. Since these experiments have been conducted without rotation, the heat transfer distribution is influenced only by the rib turbulators, the bend, and generally by the channel geometry such as shape of cross-section and aspect ratio. The contour plots show the typical structures for a rib-roughened channel, characterized by low values directly behind the ribs due to a detached flow and flow recirculation. These are followed by regions with significantly enhanced heat transfer due to flow

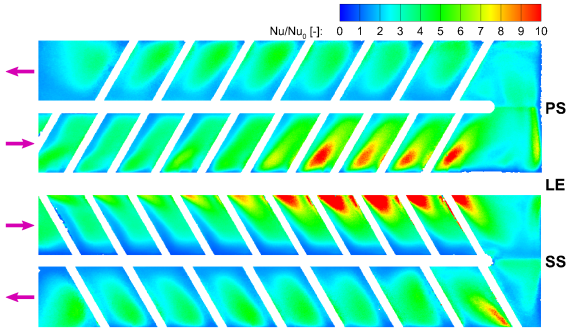

(a) $Re = 7500$

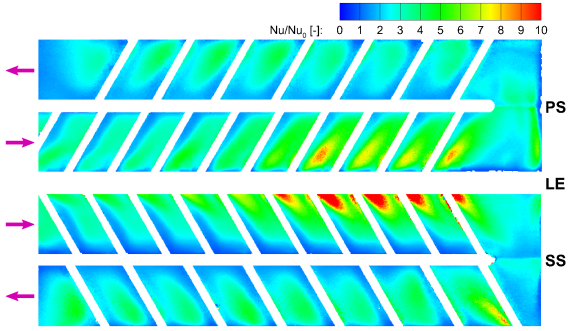

(b) $Re = 15000$

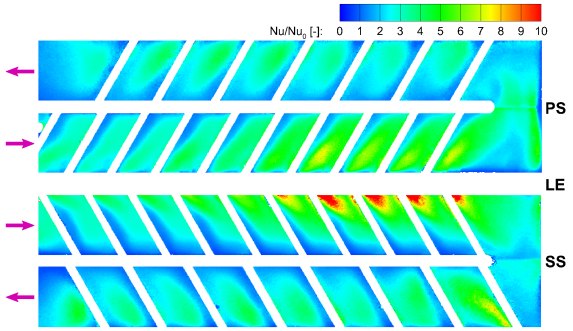

(c) $Re = 30000$

Figure 4.2: Normalized Nusselt number Nu/Nu_0, $Ro = 0$

reattachment. The inclined ribs induce secondary flows that lead to heat transfer enhancement near the leading edge in pass 1, especially in segments -4 to -1 (compare figure 4.3) upstream of the bend. In contrast, the rib induced secondary flows lead to heat transfer enhancement near the trailing edge in pass 2.

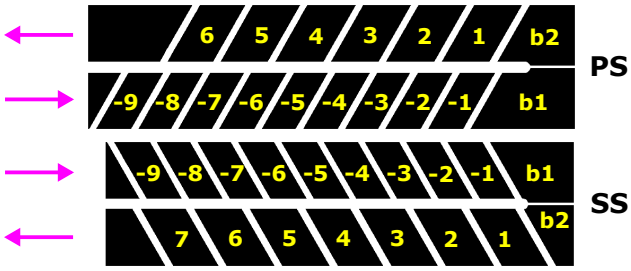

Figure 4.3: Segment numeration (ROT-B)

It can be seen that for all three Reynolds numbers shown, the structure of the heat transfer distribution remains similar. However, the level of the Nusselt number ratios decrease somewhat with increasing Reynolds numbers. This is also seen in the segment averaged data, see figure 4.4. The differences in the

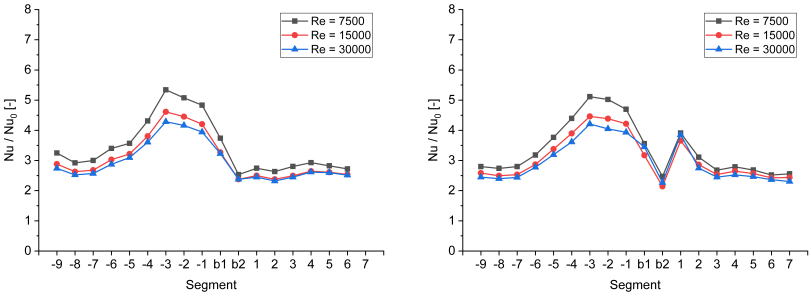

(a) PS (b) SS

Figure 4.4: Segment averaged normalized Nusselt numbers Nu/Nu_0, $Ro = 0$

normalized Nusselt numbers seem to be more pronounced in pass 1 and less in pass 2.

4.2.2 Rotating Experiments

The influence of rotation on the heat transfer distribution is presented exemplary for a target Reynolds number of $Re_{targ} = 15000$. Figure 4.5 shows the normalized Nusselt numbers for three different rotation numbers. These contour plots need to be compared to the plot of the corresponding stationary experiment, see figure 4.2b. The respective buoyancy numbers for the presented experiments are listed in table 4.1.

Table 4.1: Mean values of dimensionless quantities for $Re_{targ} = 15000$

Experiment		V0104	V0107	V0103b	V0110
Symbol	Description	Value	Value	Value	Value
Re	Reynolds number	14870	14909	14913	14840
Ro	rotation number	0.000	0.153	0.307	0.513
Bo	buoyancy number	0.000	0.133	0.551	1.470
Nu_0	ref. Nusselt number	45.28	45.37	45.38	45.20

At a rotation number of $Ro = 0.153$ (see figure 4.5a) heat transfer is significantly increased on the PS of pass 1 compared to the stationary case. On the SS only a minimal increase is visible. In pass 2 the heat transfer level is decreased on the PS. Furthermore, distinctive double structures appear in the rib segments downstream of segment 1 that are not present in the non-rotating case. On the SS heat transfer first slightly increases downstream of the bend in segments 1 to 5 and noticeably decreases in segments 6 and 7.

At a rotation number of $Ro = 0.307$ heat transfer is further enhanced on PS of pass 1 and further diminished on PS of pass 2 compared to $Ro = 0.153$. The double structures change their pattern in segments 2 to 4 and vanish completely in segments 5 and 6. On the SS of pass 1 heat transfer further increases near the leading edge, while simultaneously the regions with low values near the divider web grow and change their appearances from an L-shape to a more triangular shape. In pass 2 the regions of enhanced heat transfer are shifted from the trailing wall towards the divider web compared to the stationary case. The overall heat transfer on SS pass 2 is decreasing with rotation.

At $Ro = 0.513$ the effects described for $Ro = 0.307$ are even more pronounced. Heat transfer is further increased on PS of pass 1 and slightly further diminished on PS pass 2. The double structures on PS pass 2 have disappeared with the exception of segment 2 where this phenomenon is still slightly visible. On

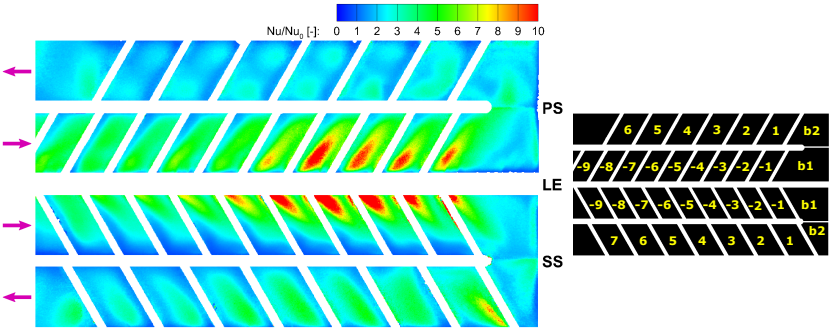

(a) $Ro = 0.153$

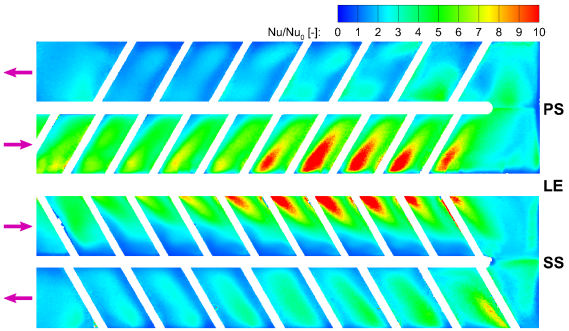

(b) $Ro = 0.307$

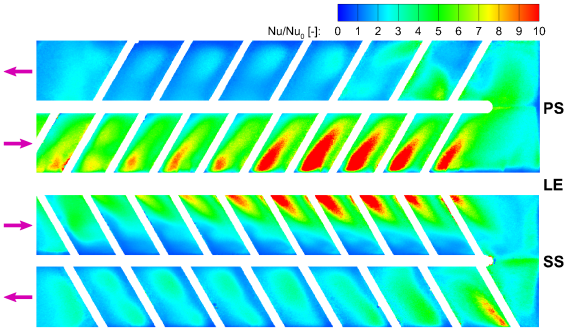

(c) $Ro = 0.513$

Figure 4.5: Normalized Nusselt number Nu/Nu_0, $Re_{targ} = 15000$

the SS the influence of rotation on the heat transfer distribution is in general smaller than on the PS. In pass 1 the differences compared to $Ro = 0.307$ are minimal. In pass 2 heat transfers in segments 2 to 5 are slightly diminished and in segments 6 and 7 slightly increased compared to $Ro = 0.307$.

4.2.3 Effects of Rotation

For a direct visualization of the rotational effects on the heat transfer distribution, the ratio of the normalized Nusselt numbers between a rotating and the corresponding stationary experiment are calculated.

$$NNNR = \frac{\left(\frac{Nu}{Nu_0}\right)_{ROT}}{\left(\frac{Nu}{Nu_0}\right)_{STAT}} \tag{4.1}$$

Instead of comparing the Nusselt numbers of the rotating and stationary experiment directly, this *NNNR* parameter was chosen in order to reduce the influence of small Reynolds number differences between the rotating and the stationary experiment. For the presented experiments with a target Reynolds number of $Re_{targ} = 15000$ the relative difference between measured mean Reynolds number and target Reynolds number was typically below 1 %. The maximum relative difference of the reference Nusselt number Nu_0 between the rotating and the stationary experiment was below 0.25 %. For lower Reynolds numbers and corresponding lower mass flow rates it becomes more and more difficult to hit the desired target Reynolds number. In these cases higher deviations between measured mean Reynolds number and target Reynolds number have to be considered. At $Re_{targ} = 7500$, for example, relative deviations of up to 4.9 % for the mean Reynolds number and up to 2.4 % for the Nu_0-value have been determined. The advantages of the *NNNR* parameter become clearer under these conditions.

With this representation of the results, the influences of possible systematic measurement errors are reduced. Possible systematic measurement errors are for example errors of the fluid temperature measurements due to unfavorable positioning of thermocouples, thermal inertia of thermocouples, calibration errors, or errors due to false assumptions regarding the material properties of the Perspex test model. These errors should affect the obtained absolute Nusselt numbers for both experiments (rotating and stationary) in the same direction and similar magnitude. Therefore, by calculating the *NNNR*, the effect of systematic measurement errors can be reduced. Figure 4.6 shows the normalized Nusselt number ratio distributions for the three rotating experiments that were

presented in figure 4.5. Regions with locally increased heat transfer due to rotation effects are represented in red. Regions with decreasing heat transfer values are represented in blue. Areas where heat transfer remains unchanged compared to the stationary reference case are indicated in yellow.

It can be seen that for PS pass 1, heat transfer enhancement can be registered for complete segments, where the values increase with increasing rotation number. In contrast, at PS pass 2, the rib segments 1 to 6 are divided into two regions. Near the divider web, heat transfer is enhanced and near the trailing edge, heat transfer is diminished. In segments 3 to 6, the enhanced areas near the divider web become smaller with increasing rotation number and vanish completely at $Ro = 0.513$. In contrast, in segment 1, the area of heat transfer enhancement near the divider web grows and the values also increase with increasing rotation number. The values of the areas near the trailing edge with diminished heat transfer further decrease with increasing rotation number. One exception is segment 2, where a region with increased values emerges in the corner between upstream rib and trailing edge, marked with a circle in figure 4.6c. At first there is a rather modest enhancement for $Ro = 0.153$ but the values increase with increasing rotation number.

On SS pass 1, the segments are also divided between heat transfer enhanced and diminished areas. Especially in the first segments (-9 to -5) heat transfer is enhanced near the leading edge and diminished near the divider web. In segments -4 to -1 the enhanced regions near the leading edge are shifted more towards the central part of the rib segment. With increasing rotation number slim areas near the divider web also show heat transfer enhancement, marked with a rectangle in figure 4.6c.

In the bend region of the SS, the first part b1 shows diminished values at $Ro = 0.153$. The values and distribution remain essentially unchanged with increasing rotation number. In contrast, part b2 of the SS bend shows heat transfer enhancement and a significant dependency from the rotation number with increasing values from $Ro = 0.153$ to $Ro = 0.513$.

On SS pass 2, heat transfer is in general enhanced for the segments 1 to 5 and diminished for segments 6 and 7 at $Ro = 0.153$. However, in segments 3 to 5 areas with $NNNR$ values below 1 are apparent in the corners between downstream rib and trailing edge, marked with an ellipse in figure 4.6a. Furthermore, in theses segments heat transfer is significantly increased in the corners between upstream rib and trailing edge. At $Ro = 0.307$ and $Ro = 0.513$, however, this characteristic shifts rather towards segments 2 and 3. With increasing rotation number also the segments 2 to 7 show a more recurring pattern with increased values near the divider web and decreased values near the trailing edge.

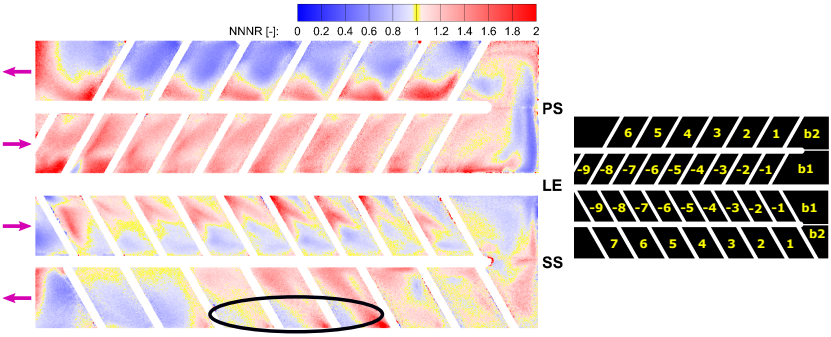

(a) $Ro = 0.153$

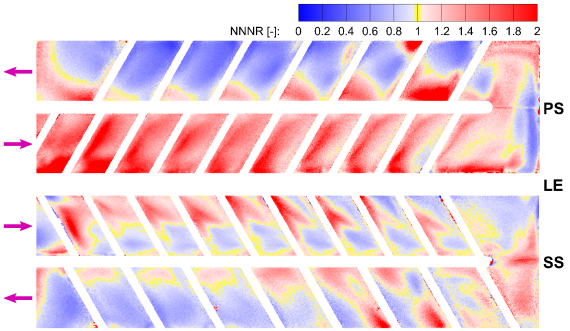

(b) $Ro = 0.307$

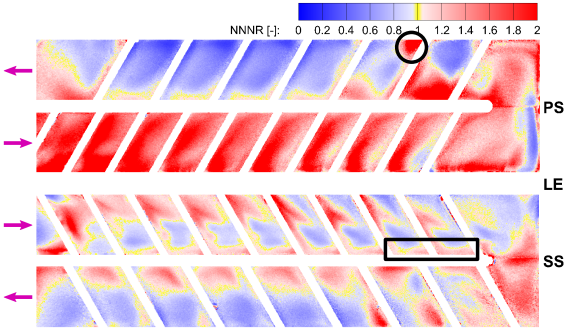

(c) $Ro = 0.513$

Figure 4.6: Normalized Nusselt number ratio $NNNR$, $Re_{targ} = 15000$

In general one can see that the effects of rotation on heat transfer affect the pressure side far more than the suction side. On the PS the bandwidth of heat transfer values widens with increasing rotation number far more than on the SS, meaning that on PS more extreme values emerge with increasing rotation number for both heat transfer enhancement and reduction.

4.3 Further Data Reduction

Data reduction procedures for line averaging and segment averaging have been performed as described in section 2.4.4. Line averaging results are presented exemplary for the experiments listed in table 4.1. Furthermore, for these cases also histograms of the *NNNR* distribution are presented. Segment averaged and passage averaged results are additionally given for the Reynolds numbers $Re_{targ} = 7500$, $Re_{targ} = 15000$ and $Re_{targ} = 30000$, while also considering all investigated rotation numbers.

4.3.1 Histograms of Normalized Nusselt Number Ratios

Histograms are derived from the *NNNR* distributions, see figure 4.7. Thereby, the channel regions PS pass 1, PS bend, PS pass 2, SS pass 1, SS bend and SS pass 2 are evaluated individually. In figure 4.7a these regions are illustrated with the color code used in the histograms. As with segment averaging, only complete rib segments are considered. Truncated segments (marked black) are neglected. Presented are stacked histograms, meaning that the histograms of the individual regions are illustrated stacked on top of each other. For the calculation of the histograms a bin width of 0.01 for the *NNNR* values was chosen.

For all rotation numbers almost all values of PS pass 1 lie above 1, meaning heat transfer enhancement due to rotational effects. In contrast, the majority of the values for PS pass 2 are below 1, meaning heat transfer reduction due to rotational effects. The values of the remaining regions are more evenly distributed between heat transfer enhancement and reduction.

At $Ro = 0.153$ a higher number of values above 1 are notable for SS pass 2. With increasing rotation number, however, the distribution is shifted more towards values below 1. On the other hand, with increasing rotation number the distribution of the PS bend shifts further to higher values, so that at $Ro = 0.513$ almost the complete PS bend region shows heat transfer enhancement.

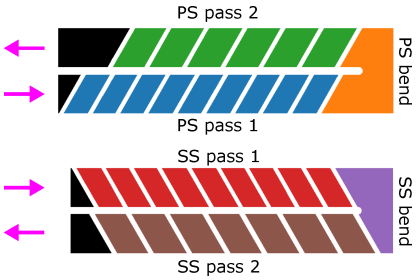

(a) Evaluated channel regions

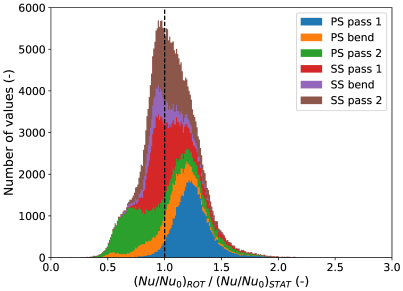

(b) $Ro = 0.153$

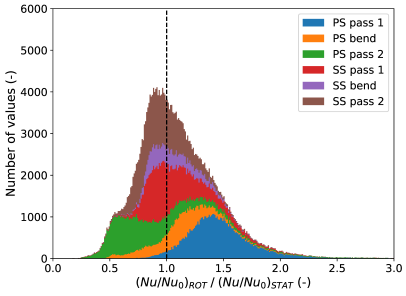

(c) $Ro = 0.307$

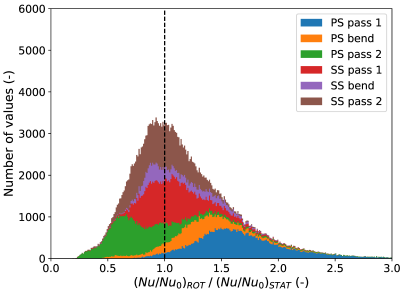

(d) $Ro = 0.513$

Figure 4.7: Histograms of *NNNRs*, $Re_{targ} = 15000$

The histograms also show the increasing bandwidth of evaluated *NNNR* values with increasing rotation number. While at $Ro = 0.153$ the highest values are approximately around $NNNR_{max} \approx 2.0$, they lie around 2.5 at $Ro = 0.307$ and around 2.9 at $Ro = 0.513$. Also the lowest values further decrease with rotation number; from $NNNR_{min} \approx 0.4$ at $Ro = 0.153$ to approximately 0.25 at $Ro = 0.513$.

4.3.2 Line Averaging

Figure 4.8 shows the regions that are considered for line averaging, marked as green parallelograms. In addition, the diagram contains all relevant coordinates

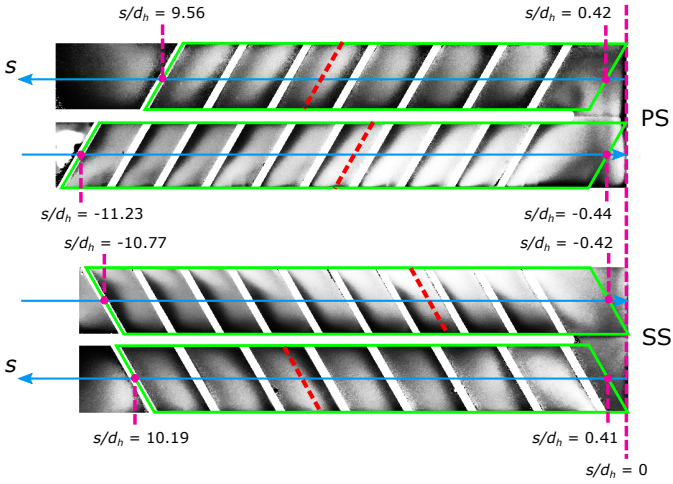

Figure 4.8: Line averaging procedure (ROT-B)

of the start and end points of the parallelograms. The results for line averaged normalized Nusselt numbers are given in figure 4.9 exemplary for $Re_{targ} = 15000$. The diagrams show the typical heat transfer pattern for a ribbed channel characterized by flow separation and flow reattachment behind the ribs. The staggered rib arrangement between PS and SS is also visible in these diagrams.

The main trends that have been described before are also shown in this representation of the data. Especially the significant increase of the normalized Nusselt numbers for PS pass 1 and the notable decrease for PS pass 2 with increasing rotation number are clearly recognizable here. Again, for SS the effects of rotation are less pronounced.

It should be mentioned that if there are strong variations along the averaging line, for example very high values near the leading edge and relatively low values near the divider web such as for SS pass 1, these extreme values cancel out each other to some degree. Thus, with this averaging method strong variations lateral to the main flow direction cannot be identified. Furthermore, areas outside of the averaging regions (green parallelograms, see 4.8) are neglected.

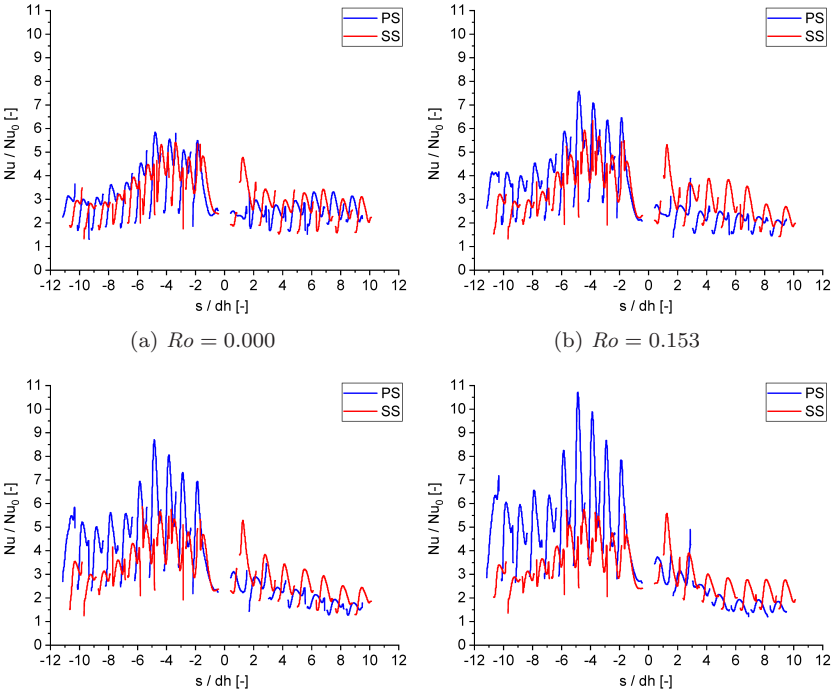

(a) $Ro = 0.000$ (b) $Ro = 0.153$

(c) $Ro = 0.307$ (d) $Ro = 0.513$

Figure 4.9: Line averaged normalized Nusselt numbers, $Re_{targ} = 15000$

Figure 4.10 shows the respective normalized Nusselt number ratios. Here the effect of rotation is directly visualized. It can be seen that rotation in general increases the line averaged values in pass 1 for both PS and SS. However, on SS also *NNNR* values below 1 are apparent for stream wise coordinates between $s/d_h = -5$ and $s/d_h = -0.42$.

In pass 2 the line averaged *NNNR* values of PS are mainly below 1 for stream wise coordinates above $s/d_h = 4$ for all presented rotation numbers. For SS pass 2 at first an increase is shown at $Ro = 0.153$. However, at rotation numbers $Ro = 0.307$ and $Ro = 0.513$, the SS values also mainly lie below 1 for stream wise coordinates above $s/d_h = 4$.

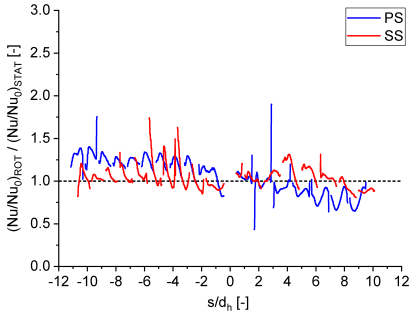

(a) $Ro = 0.153$

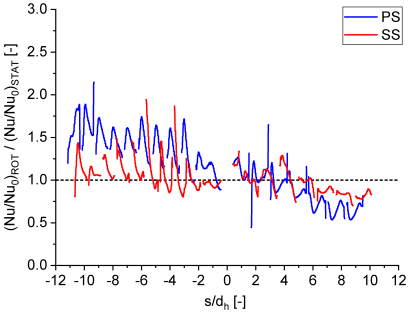

(b) $Ro = 0.307$

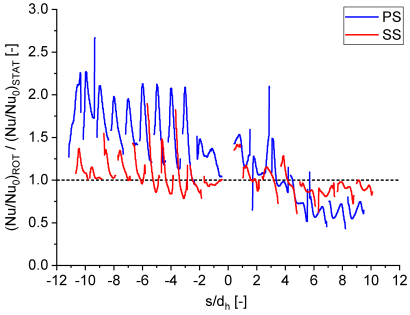

(c) $Ro = 0.513$

Figure 4.10: Line averaged *NNNR*, $Re_{targ} = 15000$

4.3.3 Segment Averaging

For segment averaging the arithmetic mean values per rib segment are calculated as described in section 2.4.4. As with line averaging, some information is lost trough the averaging process. High varieties in heat transfer values within one segment (e.g. at SS pass 1) cannot be identified or represented with segment averaged results. However, it allows a quick identification of the general trend for heat transfer per rib segment in dependence of rotation number. Furthermore, segment averaged results allow the comparison with investigations that use the approach with individually heated copper elements, e.g. Wagner et al. [71–73]. With this measurement method, mean heat transfer data per each copper segment were directly obtained.

Figure 4.11 shows the segment averaged normalized Nusselt numbers (top row) and *NNNRs* (bottom row) for the example cases at $Re_{targ} = 15000$. For the

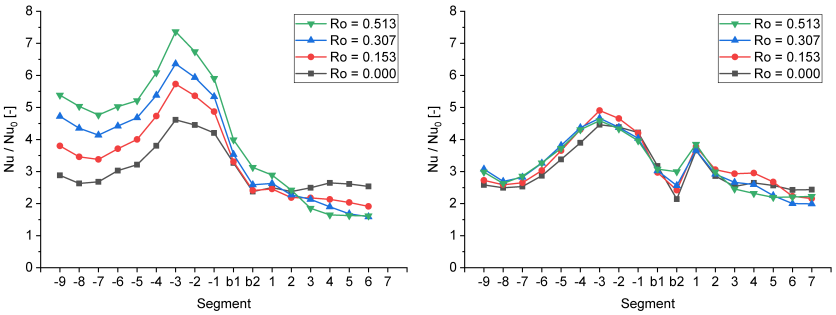

(a) Nu/Nu_0 (PS) (b) Nu/Nu_0 (SS)

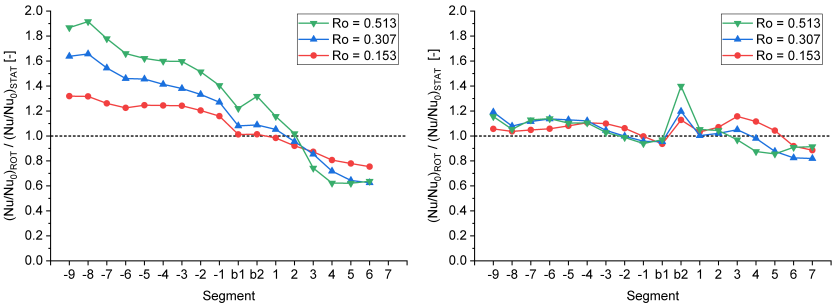

(c) *NNNR* (PS) (d) *NNNR* (SS)

Figure 4.11: Segment averaged normalized Nusselt numbers and *NNNRs*, $Re_{targ} = 15000$

PS the strong correlation between averaged heat transfer value and rotation number is immediately evident. This correlation is characterized by heat transfer enhancement in pass 1 and reduction in pass 2 with increasing rotation number. However, one can see that the intersection point between heat transfer enhancement and reduction does not lie directly in the bend region (b1 or b2), but further downstream in segment 1 ($Ro = 0.153$) or segment 2 ($Ro = 0.307$ and $Ro = 0.513$).

On the SS the effects are less distinct. Also, the trends differ for the respective rotation numbers. For $Ro = 0.153$ the *NNNR* values lie slightly above 1 in pass 1. The values for $Ro = 0.307$ and $Ro = 0.513$ are almost identical in pass

1. They lie above the values for $Ro = 0.153$ in segments -9 to -4 but below further downstream and even below 1 in segment -1. In segment b1 the values lie slightly below 1 for all presented rotation numbers. In contrast, segment b2 shows a strong dependency from the rotation number. In segment 1 all values are again slightly above 1 independent from rotation number. In the remaining segments of pass 2 the values first increase before they decline again towards the outlet. The higher the rotation number, the earlier the values fall below 1. For $Ro = 0.153$ this occurs at segment 6, for $Ro = 0.307$ at segment 4 and for $Ro = 0.513$ already at segment 3.

Another way to display the rotation number dependency is to plot the segment averaged *NNNR* values directly versus the rotation number. This is shown in figure 4.12 not only for $Re_{targ} = 15000$ but also for $Re_{targ} = 7500$ and $Re_{targ} = 30000$. Furthermore, not only three exemplary but all investigated rotation numbers are presented (i.e. 5 for each $Re_{targ} = 7500$ and $Re_{targ} = 30000$, and 7 for $Re_{targ} = 15000$).

One can see that for the PS the first few segments show almost a linear increase with rotation number, especially for $Re_{targ} = 7500$ and $Re_{targ} = 15000$. Here at the highest investigated rotation number, values of almost 2 are reached, which would mean a heat transfer increase by 100 %. In pass 2, starting from segment 2 heat transfer is reduced. The values seem to be staggered, where the values decrease in flow direction from segment to segment. The lowest *NNNR* values are registered at the last segment (no. 6).

The most interesting finding from this evaluation is that for segments with heat transfer reduction the values only decrease to a specific minimum value and then increase again with increasing rotation number. For $Re_{targ} = 7500$ and $Re_{targ} = 15000$ heat transfer in segment 6 reaches its minimum value within a rotation number range of 0.3 to 0.45. It is there approximately 40 % lower compared to the stationary case. For $Re_{targ} = 30000$ the highest investigated rotation number was $Ro = 0.308$. Therefore, no statement can be made here, whether the minimum was already reached, or if the values would have further decreased with increasing rotation number.

On the SS the results are less clear. Since for $Re_{targ} = 30000$ only results for rotation numbers up to $Ro = 0.308$ are available, in the following the general trend is only discussed for $Re_{targ} = 7500$ and $Re_{targ} = 15000$. The highest *NNNR* values are obtained for the highest rotation numbers at the bend segment b2. However, the level of heat transfer enhancement is significantly lower compared to the PS. At the highest rotation number the averaged heat transfer values for segment b2 show a maximum increase by approximately 40 %. Furthermore, while at the PS the values are staggered with respect to

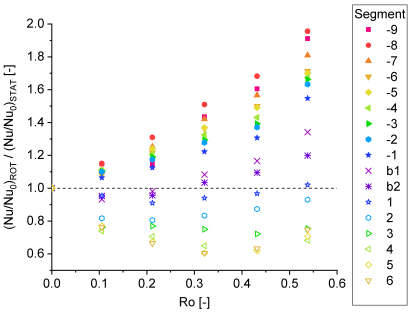

(a) PS, $Re_{targ} = 7500$

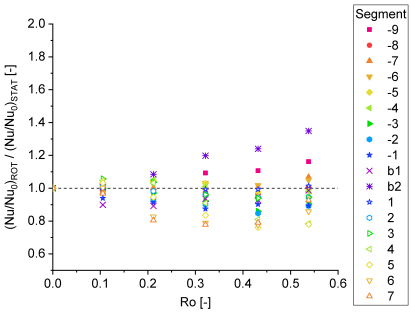

(b) SS, $Re_{targ} = 7500$

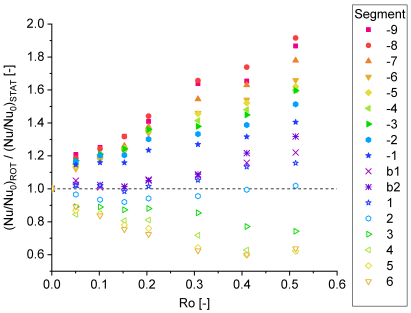

(c) PS, $Re_{targ} = 15000$

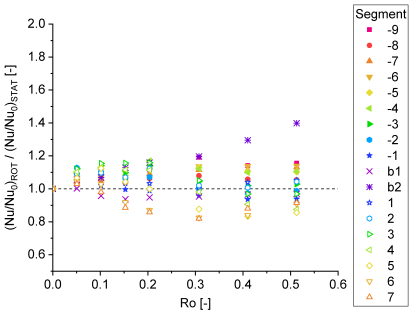

(d) SS, $Re_{targ} = 15000$

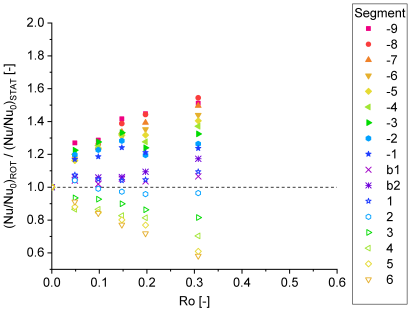

(e) PS, $Re_{targ} = 30000$

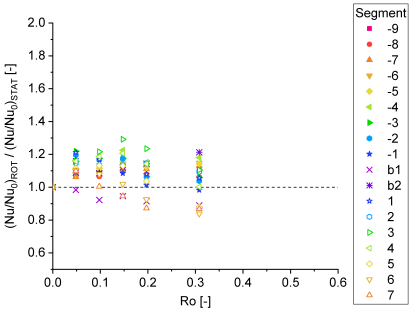

(f) SS, $Re_{targ} = 30000$

Figure 4.12: Segment averaged *NNNRs* vs. rotation number

segment position, segment b2 of the SS seems to have an exceptional behavior for the higher rotation numbers. Here, the values of the remaining segments are well below that of segment b2.

The lowest *NNNR* values on the SS are obtained at the latest segments (5 to 7). Like on PS, the values decrease only to a minimum value within a rotation number range of $0.3 \leq Ro \leq 0.45$, before they increase again with increasing rotation number. This decrease is, however, considerably lower than on the PS. On the SS minimum values of only $NNNR_{min} \approx 0.8$ are obtained.

4.3.4 Passage Averaging

For passage averaging the arithmetic mean values are calculated for complete passage walls (PS pass 1, PS pass 2, SS pass 1 and SS pass 2), as depicted in figure 4.7a. Bend regions (PS bend, SS bend) and truncated segments near the inlet and outlet are not considered in this representation. Figure 4.13 shows passage averaged *NNNR* values for the three target Reynolds numbers $Re_{targ} = 7500$, $Re_{targ} = 15000$ and $Re_{targ} = 30000$ plotted versus the rotation number. This representation of global values per passage wall allows, for example, to compare the results with other studies that provide globally evaluated heat transfer data, e.g. the results compilation by Liou et al. [41], see figure 1.3.

It can be seen, that - within the investigated rotation numbers - rotation always leads to increased global heat transfer values on PS pass 1 (unstable endwall) and to reduced values on PS pass 2 (stable endwall). While in pass 1 the values seem to increase unbounded with increasing rotation number, the reduction in pass 2 stops within a rotation number range of approximately $0.3 \leq Ro \leq 0.45$. For higher rotation numbers the values increase again. This is consistent with the curve progressions depicted in figure 1.3, where the globally averaged Nusselt numbers ratios (rotating to stationary) are depicted for unstable and stable endwalls of different channels with various cross-sectional shapes.

At the SS rotation has a much weaker influence on the global heat transfer. Furthermore, the direction of the influence (enhancement or reduction) is dependent on rotation number and Reynolds number. For SS pass 1 (stable endwall) heat transfer is slightly increased (by up to 14 %) for Reynolds numbers $Re_{targ} = 15000$ and $Re_{targ} = 30000$ but slightly decreased (by down to 6 %) for $Re_{targ} = 7500$. At SS pass 2 (unstable endwall) the *NNNR* values at first increase for the lower rotation numbers but then decrease again with increasing rotation number so that the situation switches from heat transfer

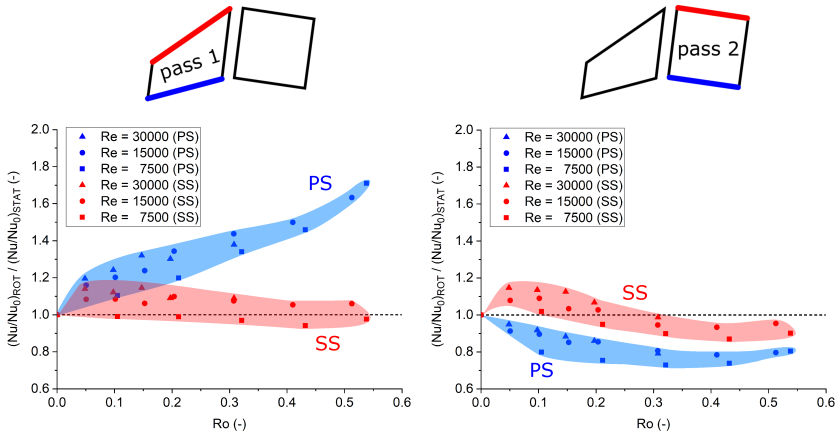

(a) Pass 1 (radial outward flow) (b) Pass 2 (radial inward flow)

Figure 4.13: Passage averaged *NNNRs*

enhancement to heat transfer reduction. The rotation number at which this changeover happens is dependent on the Reynolds number. For $Re_{targ} = 7500$ the global *NNNR* value falls below 1 already at approximately $Ro \approx 0.1$. For $Re_{targ} = 30000$ this happens at approximately $Ro \approx 0.3$. For higher rotation numbers the values seem to increase again. However, there is not enough data available to allow for a reliable statement about the further course.

The results also suggest that for a given rotation number, higher Reynolds numbers in general lead to higher *NNNR* values independent of the surface orientation (stable or unstable endwall) and regardless whether the current situation is characterized by heat transfer enhancement or reduction.

While the PS data match very well the trends of other studies as depicted by Liou et al. [41] (see figure 1.3) this isn't the case for the SS results. At SS pass 1 (stable endwall) the *NNNR* values at first increase with increasing rotation number, whereas according to figure 1.3 a decreasing trend should be expected. On the other hand at SS pass 2 (unstable endwall), where steadily increasing values could be expected, the values decrease and even fall below 1 for higher rotation numbers. A possible explanation could be the channel surface orientation with respect to the direction of rotation and the specific shape of pass 1. The skew angle between pass 1 and pass 2 is comparable to

those found in real turbine blade geometries, whereas former studies mainly used idealized configurations.

CHAPTER 5

Conclusion and Outlook

Conclusion

In this thesis the transient thermochromic liquid crystal method (TLC) has been applied for heat transfer measurements on a rotating turbine blade cooling channel configuration. The TLCs have been used here as surface temperature sensors. The main advantage of TLCs is that they can be sprayed onto the investigated inner channel surfaces using an airbrush system. Thus, this measurement method provides spatially resolved heat transfer data even for complex, engine-similar cooling channel geometries.

First, the measurement principle, the experimental procedure and the data analysis procedures were described for a stationary (non-rotating) experiment. The investigated geometry was a generic two-pass serpentine leading edge cooling scheme consisting of an inlet passage with a trapezoidal cross-section, a 180° bend and an outlet passage with a rectangular cross-section. The pressure side and suction side walls were equipped with rib turbulators that were inclined with an angle of 60° with respect to the main flow direction.

For the application of this measuring technique in a rotating experiment, several challenges had to be solved. These challenges concerned e.g. optical aspects,

such as accessibility and lighting, material loads due to additional centrifugal forces, thermal aspects with respect to the required cooling fluid temperature change, and data acquisition aspects.

The consideration of these aspects lead to the design of a rotating test rig that allows the investigation of cooling channels under engine representative conditions, characterized by Coriolis forces and rotation induced buoyancy forces onto the cooling fluid flow. The test rig, the corresponding infrastructure, the test model and measurement data acquisition procedures were described in detail.

A test campaign with rotation number variation and Reynolds number variation resulted in a total of 32 evaluated experiments. The spatially resolved results showed that rotational effects can significantly change the local heat transfer distribution. Heat transfer can be considerably increased or reduced, depending on the orientation of the observed surface with respect to the rotational axis and also depending on the local position on the surface.

In order to quantify the observed effects and for data visualization purposes, a comparison parameter was introduced: the normalized Nusselt number ratio ($NNNR$). This parameter describes the local heat transfer of a rotating experiment in relation to the corresponding stationary experiment, taking into account possible differences in the measured Reynolds number between the two experiments. Using this parameter the influence of rotation on the heat transfer distribution can be directly visualized, while simultaneously the influence of possible systematic measurement errors is minimized. The results were presented as contour plots of the 2D-heat transfer distribution. Additionally the data were reduced to line averaged, segment averaged and finally passage averaged representations.

The spatially resolved results showed that one rib segment does not need to be affected as a whole towards one direction but can simultaneously contain regions with heat transfer enhancement and heat transfer reduction. This insight would not be possible with measurement techniques that provide only mean values per segment such as the common approach with individually heated copper elements. Considering all passage surfaces together, it was shown that for an exemplary case ($Re_{targ} = 15000$), heat transfer could be increased locally by up to 190 % ($NNNR \approx 2.9$) and at a different location simultaneously decreased by down to 75 % ($NNNR \approx 0.25$). The segment averaged values of the same data showed, however, only a maximum increase by approximately 100 % ($NNNR \approx 2.0$) for one segment and simultaneously a reduction by only approximately 40 % ($NNNR \approx 0.6$) for a different segment.

The knowledge of spatially resolved heat transfer data is therefore essential for the development of future turbine blade cooling schemes. Only with this knowledge the thermal load and the temperature distribution inside the turbine blade can be reliably predicted. Thus, local cooling features can be improved and the cooling mass flow consumption can be reduced in order to optimize the thermal efficiency of gas turbine engines. The results obtained with the rotating rig presented in this thesis can therefore be a valuable contribution for the development of future internal blade cooling concepts.

Outlook

One main disadvantage of the transient TLC measurement method is, however, that the fluid temperature cannot be chosen freely in order to set arbitrary buoyancy numbers. The fluid temperature must be carefully adjusted with respect to the model start temperature and the TLC indication temperature. Only with a correctly set fluid temperature level, the TLC indications occur within a suitable time frame, as too fast or too late indications would increase measurement uncertainty.

For a rotating experiment this is especially critical, since, as shown in figures 4.6 and 4.7, rotation increases the bandwidth of the measured heat transfer values. Therefore, also the bandwidth of the indication times increases with rotation, where the earliest indications occur even faster and the latest indications occur later or even not at all within the duration of the test.

A possible solution to this problem is the simultaneous application of different TLC types with varying indication temperatures, either as mixtures or as individual layers. Mixtures of several TLC types have been applied in stationary tests for example by Ling et al. [37], Ryley et al. [59], Ryley et al. [60], Talib et al. [67], and Waidmann et al. [76] and in rotating tests for example by Blair et al. [6] (steady-state) and Pagnacco et al. [48, 49] (transient).

With this approach, several correlations between time and surface temperature are obtained for each pixel from a single experiment. For each region or even for each individual pixel the one indication from the set of indications could then be selected that would result in the lowest measurement uncertainties.

Bibliography

[1] Acharya, S., Eliades, V., and Nikitopoulos, D. E.: Heat Transfer Enhancements in Rotating Two-Pass Coolant Channels With Profiled Ribs: Part 1–Average Results. *J. Turbomach.* 2001/01/00/, 123 (1), pp. 97–106.

[2] Al-Hadhrami, L. and Han, J.-C.: Effect of rotation on heat transfer in two-pass square channels with five different orientations of 45° angled rib turbulators. *International Journal of Heat and Mass Transfer*, 2003, 46 (4), pp. 653–669. DOI: 10.1016/S0017-9310(02)00325-3.

[3] Anderson, M. R. and Baughn, J. W.: Hysteresis in Liquid Crystal Thermography. *J. Heat Transfer*, 2004/06/00/, 126 (3), pp. 339–346.

[4] Arganda-Carreras, I., Sorzano, C. O. S., Marabini, R., Carazo, J. M., Ortiz-de-Solorzano, C., and Kybic, J.: 'Consistent and Elastic Registration of Histological Sections Using Vector-Spline Regularization'. In: *Beichel, Sonka (Hg.) 2006 – Computer vision approaches to medical image analysis. CVAMIA 2006.* Vol. 4241, pp. 85–95. DOI: 10.1007/11889762.

[5] Baehr, H. D. and Stephan, K.: Wärme- und Stoffübertragung. 8., aktualisierte Auflage. Berlin, Heidelberg: Springer Berlin Heidelberg, 2013. DOI: 10.1007/978-3-642-36558-4.

[6] Blair, M. F., Wagner, J. H., and Steuber, G. D.: New applications of liquid–crystal thermography in rotating turbomachinery heat transfer research. *ASME, International Gas Turbine and Aeroengine Congress and Exposition, 36th, Orlando, FL, June 3-6, 1991. 11 p.* 1991.

[7] Bons, J. P. and Kerrebrock, J. L.: Complementary Velocity and Heat Transfer Measurements in a Rotating Cooling Passage With Smooth Walls. *Journal of Turbomachinery*, 1999, 121 (4), pp. 651–662. DOI: 10.1115/1.2836717.

[8] Boyce, M. P.: Gas turbine engineering handbook. 2. ed. Boston, Mass.: Gulf Professional Publ, 2002.

[9] Chambers, A. C., Gillespie, D. R. H., Ireland, P. T., and Dailey, G. M.: A Novel Transient Liquid Crystal Technique to Determine Heat Transfer Coefficient Distributions and Adiabatic Wall Temperature in a Three-Temperature Problem. *Journal of Turbomachinery*, 2003, 125 (3), p. 538. DOI: 10.1115/1.1575252.

[10] Chang, S. W., Liou, T. M., Hung, J. H., and Yeh, W.-H.: Heat Transfer in a Radially Rotating Square-Sectioned Duct With Two Opposite Walls Roughened by 45 Deg Staggered Ribs at High Rotation Numbers. *J. Heat Transfer*, 2007/02/00/, 129 (2), pp. 188–199.

[11] Cheah, S. C., Iacovides, H., Jackson, D. C., Ji, H., and Launder, B. E.: LDA Investigation of the Flow Development Through Rotating U-Ducts. *Journal of Turbomachinery*, 1996, 118 (3), pp. 590–596. DOI: 10.1115/1.2836706.

[12] Coletti, F., Maurer, T., Arts, T., and Di Sante, A.: Flow field investigation in rotating rib-roughened channel by means of particle image velocimetry. *Experiments in Fluids*, 2012, 52 (4), pp. 1043–1061. DOI: 10.1007/s00348-011-1191-2.

[13] Davenport, R.: The Benefits of a Rotating Rig for Research into Advanced Turbine Cooling Systems: RTO MEETING PROCEEDINGS 8. *RTO Applied Vehicle Technology Panel (AVT) Symposium, Toulouse, France*, 1998.

[14] Ekkad, S. V. and Han, J. C.: A transient liquid crystal thermography technique for gas turbine heat transfer measurements. *Measurement Science and Technology*, 2000, 11 (7), pp. 957–968. DOI: 10.1088/0957-0233/11/7/312.

[15] Elfert, M., Voges, M., and Klinner, J.: Detailed Flow Investigation Using PIV in a Rotating Square-Sectioned Two-Pass Cooling System With Ribbed Walls. *Proceedings of the ASME Turbo Expo 2008*. New York, NY: ASME, 2008, pp. 1039–1050. DOI: 10.1115/GT2008-51183.

[16] Eliades, V., Nikitopoulos, D. E., and Acharya, S.: Mass-Transfer Distribution in Rotating, Two-Pass, Ribbed Channels with Vortex Generators. *Journal of Thermophysics and Heat Transfer*, 2001, 15 (3), pp. 266–274. DOI: 10.2514/2.6622.

[17] Gallo, M., Astarita, T., and Carlomagno, G. M.: Heat transfer measurements in a rotating two-pass square channel. *Quantitative InfraRed Thermography Journal*, 2007, 4 (1), pp. 41–62. DOI: 10.3166/qirt.4.41-62.

[18] Han, J.-C. and Zhang, Y. M.: Effect of Uneven Wall Temperature on Local Heat Transfer in a Rotating Square Channel With Smooth Walls and Radial Outward Flow. *J. Heat Transfer*, 1992, 114 (4), p. 850. DOI: 10.1115/1.2911892.

[19] Han, J.-C., Zhang, Y.-M., and Kalkuehler, K.: Uneven Wall Temperature Effect on Local Heat Transfer in a Rotating Two-Pass Square Channel With Smooth Walls. *J. Heat Transfer*, 1993, 115 (4), p. 912. DOI: 10.1115/1.2911387.

[20] Han, J.-C.: Recent Studies in Turbine Blade Cooling. *The International Journal of Rotating Machinery*, 2004, 10 (6), pp. 443–457. DOI: 10.1080/10236210490503978.

[21] Han, J.-C. and Huh, M.: Recent Studies in Turbine Blade Internal Cooling. *Heat Transfer Research*, 2010, 41 (8), pp. 803–828. DOI: 10.1615/HeatTransRes.v41.i8.30.

[22] Han, J.-C., Dutta, S., and Ekkad, S.: Gas Turbine Heat Transfer and Cooling Technology. Second Edition. Hoboken: CRC Press, 2012.

[23] Iacovides, H., Jackson, D. C., Ji, H., Kelemenis, G., Launder, B. E., and Nikas, K.: LDA Study of the Flow Development Through an Orthogonally Rotating U-Bend of Strong Curvature and Rib-Roughened Walls. *Journal of Turbomachinery*, 1998, 120 (2), pp. 386–391. DOI: 10.1115/1.2841417.

[24] Incropera, F. P., DeWitt, D. P., Bergman, T. L., and Lavine, A. S.: Fundamentals of heat and mass transfer. 7. ed., international student version. Singapore: Wiley, 2013.

[25] Ireland, P. T. and Jones, T. V.: The response time of a surface thermometer employing encapsulated thermochromic liquid crystals. *Journal of Physics E: Scientific Instruments*, 1987, 20 (10), pp. 1195–1199. DOI: 10.1088/0022-3735/20/10/008.

[26] Ireland, P. T. and Jones, T. V.: Liquid crystal measurements of heat transfer and surface shear stress. *Measurement Science and Technology*, 2000, 11 (7), pp. 969–986. DOI: 10.1088/0957-0233/11/7/313.

[27] Ireland, P. T., Mittal, V., Namgoon, H., and Jackson, D.: Heat Transfer and Flow Testing in Engine HP Turbine Cooling System Development. *Int. Symp. on Heat Transfer in Gas Turbine Systems, Turbine-09, Antalya, Turkey*, 2009.

[28] Jenkins, S. C., Shevchuk, I. V., von Wolfersdorf, J., and Weigand, B.: Transient Thermal Field Measurements in a High Aspect Ratio Channel Related to Transient Thermochromic Liquid Crystal Experiments. *Journal of Turbomachinery*, 2012, 134 (3), p. 31002. DOI: 10.1115/1.3106028.

[29] Johnson, B. V., Wagner, J. H., Steuber, G. D., and Yeh, F. C.: Heat Transfer in Rotating Serpentine Passages With Selected Model Orientations for Smooth or Skewed Trip Walls. *ASME 1993 International Gas Turbine and Aeroengine Congress and Exposition*. [Place of publication not identified]: [publisher not identified], 5241993. DOI: 10.1115/93-GT-305.

[30] Johnson, B. V., Wagner, J. H., Steuber, G. D., and Yeh, F. C.: Heat Transfer in Rotating Serpentine Passages With Trips Skewed to the Flow. *Journal of Turbomachinery*, 1994, 116 (1), p. 113. DOI: 10.1115/1.2928265.

[31] Kloss, M.: Stoffübergang in durchströmten, rotierenden Relativsystemen: Aussagefähigkeit der Naphthalin-Sublimations-Methode: Dissertation,Technische Universität Darmstadt. 2015.

[32] LCR Hallcrest: Handbook of thermochromic liquid crystal technology: RT006 Rev01.

[33] LCR Hallcrest: TLC products for use in research and testing applications: RT001 Rev02.

[34] Les, C., Brend, M. A., Bonham, C., and Carrotte, J. F.: Quantifying ageing effects in thermochromic liquid crystal thermography as applied to transient convective heat transfer experiments. *Measurement Science and Technology*, 2018, 29 (11), p. 115201. DOI: 10.1088/1361-6501/aadb24.

[35] Ligrani, P. M., Oliveira, M. M., and Blaskovich, T.: Comparison of Heat Transfer Augmentation Techniques. *AIAA Journal*, 2003, 41 (3), pp. 337–362. DOI: 10.2514/2.1964.

[36] Ligrani, P.: Heat Transfer Augmentation Technologies for Internal Cooling of Turbine Components of Gas Turbine Engines. *The International Journal of Rotating Machinery*, 2013, 2013 (3), pp. 1–32. DOI: 10.1155/2013/275653.

[37] Ling, J. P. C. W., Ireland, P. T., and Turner, L.: A Technique for Processing Transient Heat Transfer, Liquid Crystal Experiments in the Presence of Lateral Conduction. *Journal of Turbomachinery*, 2004, 126 (2), p. 247. DOI: 10.1115/1.1740777.

[38] Liou, T.-M. and Chen, C.-C.: LDV Study of Developing Flows Through a Smooth Duct With a 180 deg Straight-Corner Turn. *Journal of Turbomachinery*, 1999, 121 (1), pp. 167–174. DOI: 10.1115/1.2841228.

[39] Liou, T.-M., Chen, C.-C., and Chen, M.-Y.: TLCT and LDV measurements of heat transfer and fluid flow in a rotating sharp turning duct. *International Journal of Heat and Mass Transfer*, 2001, 44 (9), pp. 1777–1787. DOI: 10.1016/S0017-9310(00)00221-0.

[40] Liou, T.-M., Hwang, Y. S., and Li, Y.-C.: Flowfield and Pressure Measurements in a Rotating Two-Pass Duct With Staggered Rounded Ribs Skewed 45Degrees to the Flow. *Journal of Turbomachinery*, 2004, 128 (2), pp. 340–348. DOI: 10.1115/1.2162180.

[41] Liou, T. M., Chang, S. W., Hung, J. H., and Chiou, S. F.: High rotation number heat transfer of a 45° rib-roughened rectangular duct with two channel orientations. *International Journal of Heat and Mass Transfer*, 2007, 50 (19-20), pp. 4063–4078. DOI: 10.1016/j.ijheatmasstransfer.2007.01.060.

[42] Liou, T.-M., Chang, S. W., Lan, Y.-A., and Chan, S.-P.: Isolated and Coupled Effects of Rotating and Buoyancy Number on Heat Transfer and Pressure Drop in a Rotating Two-Pass Parallelogram Channel With Transverse Ribs. *Journal of Heat Transfer*, 2018, 140 (3), p. 032001. DOI: 10.1115/1.4038133.

[43] Mathison, R. M. and Dunn, M. G.: A New Rotating Facility for Investigating Cooling Passage Internal Heat Transfer: GPPF-2017-158. *Proceedings of the 1st Global Power and Propulsion Forum, Zurich, Switzerland*, 2017.

[44] Morris, W. D. and Salemi, R.: An Attempt to Uncouple the Effect of Coriolis and Buoyancy Forces Experimentally on Heat Transfer in Smooth Circular Tubes That Rotate in the Orthogonal Mode. *J. Turbomach.* 1992/10/00/, 114 (4), pp. 858–864.

[45] Morris, W. D.: A rotating facility to study heat transfer in the cooling passages of turbine rotor blades. *Proceedings of the Institution of Mechanical Engineers, Part A: Journal of Power and Energy 1990-1996 (vols 204-210)*, 1996, 210 (11), pp. 55–63.

[46] Narasimhan, T. N.: Fourier's heat conduction equation: History, influence, and connections. *Proceedings of the Indian Academy of Sciences - Earth and Planetary Sciences*, 1999, 108 (3), pp. 117–148. DOI: 10.1007/BF02842327.

[47] Pagnacco, F., Furlani, L., Armellini, A., Casarsa, L., and Davis, A.: Rotating Heat Transfer Measurements on a Multi-Pass Internal Cooling Channel: I — Rig Development. *Proceedings of the ASME Turbo Expo: Turbine Technical Conference and Exposition - 2016*. New York, N.Y.: The American Society of Mechanical Engineers, 2016, V05BT16A005. DOI: 10.1115/GT2016-56308.

[48] Pagnacco, F., Furlani, L., Armellini, A., Casarsa, L., and Davis, A.: Rotating Heat Transfer Measurements on a Multi-Pass Internal Cooling Channel: II — Experimental Tests. *Proceedings of the ASME Turbo Expo: Turbine Technical Conference and Exposition - 2016*. New York, N.Y.: The American Society of Mechanical Engineers, 2016, V05BT16A004. DOI: 10.1115/GT2016-56307.

[49] Pagnacco, F., Furlani, L., Armellini, A., Casarsa, L., and Davis, A.: Rotating Heat Transfer Measurements on Realistic Multi-pass Geometry. *Energy Procedia*, 2016, 101, pp. 758–765. DOI: 10.1016/j.egypro.2016.11.096.

[50] Pearce, R., Ireland, P., He, L., McGilvray, M., and Romero, E.: Computational and Experimental Study of Heat Transfer in Rotating Ribbed Radial Turbine Cooling Passages. *Proceedings of the ASME Turbo Expo: Turbine Technical Conference and Exposition - 2015*. New York, NY: ASME, 2015, V05AT11A026. DOI: 10.1115/GT2015-43158.

[51] Poser, R., von Wolfersdorf, J., and Semmler, K.: Transient Heat Transfer Experiments in Complex Passages: HT2005-72260. *Proceedings of HT2005 ASME Summer Heat Transfer Conference, July 17-22, 2005, San Francisco, California, USA*, 2005.

[52] Poser, R., Ferguson, J. R., and von Wolfersdorf, J.: Temporal Signal Preprocessing and Evaluation of Thermochromic Liquid Crystal Indications in Transient Heat Transfer Experiments. *8th European Conference on Turbomachinery Fluid Dynamics and Thermodynamics*, 2009, pp. 785–795.

[53] Poser, R. and von Wolfersdorf, J.: Transient liquid crystal thermography in complex internal cooling systems. *VKI Lecture Series - Internal Cooling in Turbomachinery, von Karman Institute for Fluid Dynamics*, 2010, (VKI LS 2010-05).

[54] Poser, R.: Transient heat transfer experiments in complex geometries using liquid crystal thermography: Dissertation. 1st ed. München: Verl. Dr. Hut, 2010.

[55] Rathjen, L., Hennecke, D. K., Sivade, C., and Semmler, K.: Detailed experimental and numerical heat/mass transfer investigations in a rotating two-pass coolant channel with staggered 45° ribs. *ISROMAC 9, International Symposium on Transport Phenomena and Dynamics of Rotating Machinery, Honolulu, Hawaii, USA, Feb. 10-14*.

[56] Rathjen, L.: Experimentelle Wärme-, Stoffübergangsuntersuchungen an einem rotierenden Kühlkanalmodell mit Rippen: Dissertation,Technische Universität Darmstadt. 2003.

[57] Ristori, A., Da Costa, I., Chedevergne, F., Roux, P., and Carru, D.: P.I.V. Flow Characterization Inside a Large-Scale U-Shaped Smooth and Ribbed Rotating Channel. *5th European Conference for Aeronautics and Space Sciences (EUCASS)*, 2013.

[58] Rowbury, D. A., Parneix, S., Chanteloup, D. L. A., and Lees, A.: Research into the Influence of Rotation on the Internal Cooling of Turbine Blades. *NATO/AGARD Symposium on Advanced Flow Management - Heat Transfer and Cooling in Propulsion and Power Systems, Norway*, 2001.

[59] Ryley, J. C., McGilvray, M., and Gillespie, D. R. H.: Calculation of Heat Transfer Coefficient Distribution on 3D Geometries From Transient Liquid Crystal Experiments. *ASME Turbo Expo 2014: Turbine Technical Conference and Exposition*. Monday 16 June 2014, V05BT14A019. DOI: 10.1115/GT2014-26973.

[60] Ryley, J. R., McGilvray, M., and Gillespie, D.: Local Heat Transfer Coefficient Measurements on an Engine-Representative Internal Cooling Passage. *Journal of Thermophysics and Heat Transfer*, 2018, 33 (1), pp. 189–198. DOI: 10.2514/1.T5206.

[61] Schindelin, J. et al.: Fiji: an open-source platform for biological-image analysis. *Nature Methods*, 2012, 9 (7), pp. 676–682. DOI: 10.1038/nmeth.2019.

[62] Servouze, Y.: 3D Laser Anemometry in a Rotating Cooling Channel. *ASME 1998 International Gas Turbine and Aeroengine Congress and Exhibition*. New York, N.Y.: ASME, 1998. DOI: 10.1115/98-GT-123.

[63] Stasiek, J. A. and Kowalewski, T. A.: Thermochromic liquid crystals in heat transfer research. *XIV Conference on Liquid Crystals: Chemistry, Physics, and Applications*. SPIE Proceedings. SPIE, 2001, p. 374. DOI: 10.1117/12.472179.

[64] Sutherland, W.: LII. The viscosity of gases and molecular force. *The London, Edinburgh, and Dublin Philosophical Magazine and Journal of Science*, 1893, 36 (223), pp. 507–531. DOI: 10.1080/14786449308620508.

[65] Szirtes, T. and Rózsa, P.: Applied dimensional analysis and modeling. 2. ed. Amsterdam: Elsevier/Butterworth-Heinemann, 2007.

[66] Taler, J. and Duda, P.: Solving Direct and Inverse Heat Conduction Problems. Berlin, Heidelberg: Springer Berlin Heidelberg, 2006. DOI: 10.1007/978-3-540-33471-2.

[67] Talib, A. R. A., Neely, A. J., Ireland, P. T., and Mullender, A. J.: A Novel Liquid Crystal Image Processing Technique Using Multiple Gas Temperature Steps to Determine Heat Transfer Coefficient Distribution and Adiabatic Wall Temperature. *Journal of Turbomachinery*, 2004, 126 (4), pp. 587–596.

[68] Taslim, M. E., Rahman, A., and Spring, S. D.: An Experimental Investigation of Heat Transfer Coefficients in a Spanwise Rotating Channel With Two Opposite Rib-Roughened Walls. *J. Turbomach.* 1991/01/00/, 113 (1), pp. 75–82.

[69] Vogel, G. and Weigand, B.: A new evaluation method for transient liquid crystal experiments: NHTC2001-20250. *Proceedings of ASME NHTC'01 35th National Heat Transfer Conference*, 2001.

[70] von Wolfersdorf, J. and Weigand, B.: Turbine blade internal cooling - selected experimental approaches: May 3-6, 2010 / edited by F. Coletti & T. Arts. Vol. VKI LS 2010-05. Internal cooling in turbomachinery. Rhode Saint Genèse and Belgium: Von Karman Institute for Fluid Dynamics, 2010.

[71] Wagner, J. H., Johnson, B. V., and Hajek, T. J.: Heat Transfer in Rotating Passages With Smooth Walls and Radial Outward Flow. *J. Turbomach.* 1991, 113 (1), pp. 42–51.

[72] Wagner, J. H., Johnson, B. V., and Kopper, F. C.: Heat Transfer in Rotating Serpentine Passages With Smooth Walls. *J. Turbomach.* 1991, 113 (3), pp. 321–330.

[73] Wagner, J. H., Johnson, B. V., Graziani, R. A., and Yeh, F. C.: Heat Transfer in Rotating Serpentine Passages With Trips Normal to the Flow. *Journal of Turbomachinery*, 1992, 114 (4), pp. 847–857. DOI: 10.1115/1.2928038.

[74] Waidmann, C., Poser, R., Göhring, M., and von Wolfersdorf, J.: First operation of a rotating test rig for transient thermochromic liquid crystal heat transfer experiments: MTT2418A11. *The 24th Symposium on Measuring Techniques in Turbomachinery. Transonic and Supersonic Flow in Cascades and Turbomachines held on Aug. 30-31, 2018, IT-CAS, Prague, Czech Republic*.

[75] Waidmann, C., Poser, R., Nieland, S., and von Wolfersdorf, J.: Design of a Rotating Test Rig for Transient Thermochromic Liquid Crystal Heat Transfer Experiments. *ISROMAC 2016, International Symposium on Transport Phenomena and Dynamics of Rotating Machinery, Hawaii, Honolulu, April 10-15, 2016*.

[76] Waidmann, C., Poser, R., and von Wolfersdorf, J.: Application of Thermochromic Liquid Crystal Mixtures for Transient Heat Transfer Measurements. *10th European Conference on Turbomachinery Fluid Dynamics and Thermodynamics, Lappeenranta, Finland*, 2013, pp. 685–696.

[77] Weigand, B., Semmler, K., and Wolfersdorf, J. von: Heat transfer technology for internal passages of air-cooled blades for heavy-duty gas turbines. *Annals of the New York Academy of Sciences*, 2001, 934, pp. 179–193. DOI: 10.1111/j.1749-6632.2001.tb05851.x.

[78] White, F. M.: Viscous fluid flow. 3. ed., internat. ed. McGraw-Hill series in mechanical engineering. 2006.

[79] Williams, W. C.: If the Dittus and Boelter equation is really the McAdams equation, then should not the McAdams equation really be the Koo equation? *International Journal of Heat and Mass Transfer*, 2011, 54 (7-8), pp. 1682–1683. DOI: 10.1016/j.ijheatmasstransfer.2010.11.047.

[80] Yan, Y. and Owen, J. M.: Uncertainties in transient heat transfer measurements with liquid crystal. *International Journal of Heat and Fluid Flow*, 2002, 23 (1), pp. 29–35. DOI: 10.1016/S0142-727X(01)00125-4.

APPENDIX A

Uncertainty Analysis

An uncertainty analysis was carried out based on Poser et al. [51], Poser [54], and Waidmann et al. [76]. The uncertainties of the evaluated heat transfer coefficients depend on uncertainties of temperature and time measurements, on uncertainties regarding the material properties of the model, as well as on the magnitude of the evaluated heat transfer coefficients themselves. The assumed variances of the influencing parameters are listed in table A.1.

Table A.1: Parameters for uncertainty analysis

Symbol	Value	Variance	Unit	Description
T_0	varies	0.2	K	initial temperature
T_f	varies	0.2	K	fluid temperature
T_{TLC}	varies	0.2	K	calibr. TLC indication temp.
t_{TLC}	varies	0.2	s	indication time
ρ_w	1190	10	$\mathrm{kg/m^3}$	density of Perspex at 20 °C
c_w	1470	10	$\mathrm{J/(kg\,K)}$	specific heat capacity of Perspex
k_w	0.19	0.01	$\mathrm{W/(m\,K)}$	thermal conductivity of Perspex at 20 °C

In order to assess local uncertainties, time-invariant local equivalent fluid temperatures $T_{f,eq}(x,y)$ are determined during the heat transfer analysis. They represent hypothetical ideal fluid temperature steps, that would result in the same indication times as the actual measured fluid temperature histories $T_f(x,y,t)$. With this simplification local dimensionless equivalent temperature ratios are determined

$$\Theta_{eq}(x,y) = \frac{T_{TLC} - T_0}{T_{f,eq}(x,y) - T_0} \tag{A.1}$$

Yan and Owen [80] investigated the influence of temperature measurement uncertainties on the uncertainties of the evaluated heat transfer coefficients. They recommended a range of $0.3 < \Theta < 0.7$ with an optimal value of $\Theta_{opt} \approx 0.52$ for the dimensionless temperature ratio. At these temperature conditions the uncertainties for the evaluated heat transfer can be expected to be reasonably low.

Figure A.1 shows contour plots of the dimensionless equivalent temperature distributions for two exemplary experiments: experiment V0120 with a target Reynolds number of $Re_{targ} = 7500$ (figure A.1a) and experiment V0126 with $Re_{targ} = 60000$ (figure A.1b). For V0120, equivalent temperature values were obtained mainly in the range $0.3 < \Theta_{eq} < 0.6$. They thus meet the Θ-criterion of Yan and Owen [80]. However, at areas with high heat transfer the dimensionless equivalent temperature ratio reached values of up to $\Theta_{eq} = 0.8$. Here higher uncertainties must be expected.

For V0126, all dimensionless equivalent temperature values are in the range of $0.9 < \Theta_{eq} < 1.0$. This means the equivalent fluid temperature $T_{f,eq}$ deviated only slightly from the indication temperature T_{TLC}. Thus, for this experiment high uncertainties for the evaluated heat transfer coefficients must be expected for the complete channel.

The relative uncertainties for the heat transfer coefficient s_h/h can then be determined from the dimensionless equivalent temperature ratios Θ_{eq}, the evaluated local heat transfer coefficients h, and the variances of the influencing parameters listed in table A.1.

Figure A.2 shows the contour plots of the relative uncertainty distribution for the two experiments V0120 and V0126. For V0120 the values are mainly below $s_h/h = 0.05$ and only slightly elevated at areas with high heat transfer, see figure A.2a. As expected, the relative uncertainties are significantly higher for experiment V0126, see figure A.2b. They are mainly in the order of $s_h/h = 0.25$, but also reach values of $s_h/h = 0.5$ and above at areas with high heat transfer.

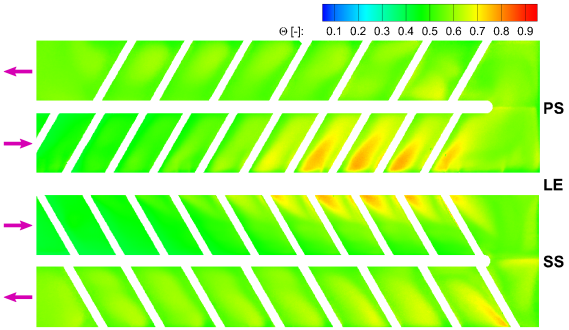

(a) V0120, $Re_{targ} = 7500$

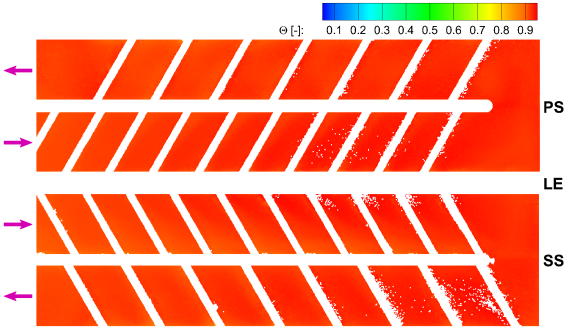

(b) V0126, $Re_{targ} = 60000$

Figure A.1: Dimensionless equivalent temperature distribution Θ_{eq}

A quick assessment of the obtained relative uncertainties can be achieved by evaluating histograms of the uncertainty distributions. Stacked histograms for the relative uncertainties of PS and SS are given in figure A.3. While the uncertainty distribution for experiment V0120 is very narrow and all values are well below 0.1 (see figure A.3a), experiment V0126 shows a much wider uncertainty distribution (see figure A.3b). The lowest values are just above $s_h/h = 0.1$ and reach values up to $s_h/h = 1.0$. These high uncertainties must be mainly attributed to unfavorable fluid temperature settings with respect to the given start temperature T_0 and given indication temperature T_{TLC} of the TLC type in use. Therefore, the uncertainties of experiment V0126 were considered too high and the results of this experiment were rejected.

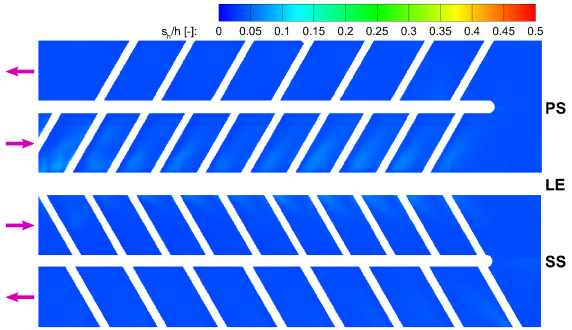

(a) V0120, $Re_{targ} = 7500$

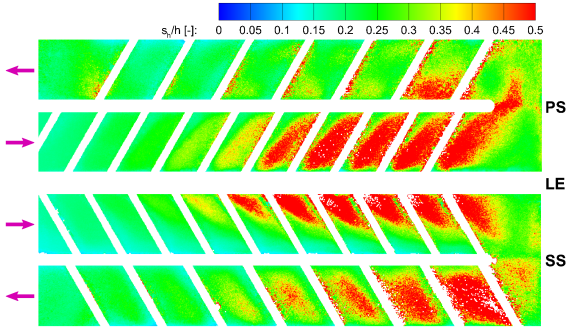

(b) V0126, $Re_{targ} = 60000$

Figure A.2: Relative uncertainty of the heat transfer coefficient s_h/h

The temperature settings must be adjusted for each experiment individually with regards to the other test parameters and current boundary conditions. The fluid temperature must be chosen to achieve a suitable range for Θ_{eq} in order to reduce the influence of temperature uncertainties. On the other hand it must be adjusted to the estimated heat transfer level to achieve a suitable range for the indication times t_{Gmax} and this way reduce the influence of time measurement uncertainties on the heat transfer evaluation.

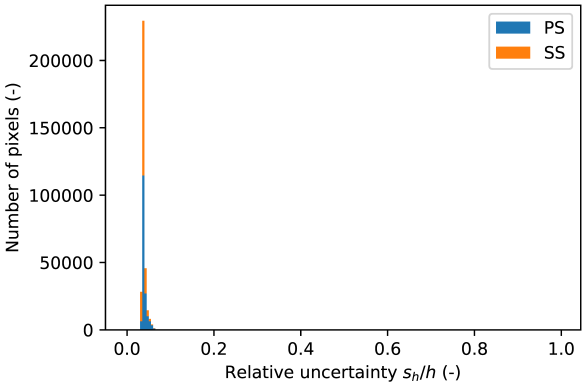

(a) V0120, $Re_{targ} = 7500$

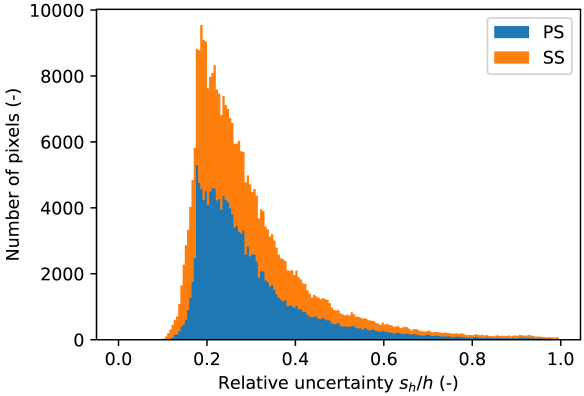

(b) V0126, $Re_{targ} = 60000$

Figure A.3: Histograms of s_h/h

APPENDIX B

Similarity Parameters

In this chapter, the relevant dimensionless quantities for a rotating cooling channel are derived (compare von Wolfersdorf and Weigand [70]). Considering this channel as part of an internal cooling system of a gas turbine blade, some simplifications and assumptions can be made. The cooling fluid can be treated as ideal gas with constant properties. The flow velocities are generally in the lower Mach number ($Ma < 0.3$) to avoid large pressure losses due to compressibility effects. Therefore, the fluid can be considered incompressible for most parts of the internal cooling system. Furthermore, chemical reactions within the fluid and radiation effects can be neglected.

B.0.1 Conservation Equations

For the following compilation of the conservation equations for a rotating frame of reference, we assume that the axis of rotation is parallel to the z-axis, as illustrated in figure B.1. We furthermore apply the Boussinesq approximation, where the density is treated as constant except in the centrifugal buoyancy term of the momentum equations.

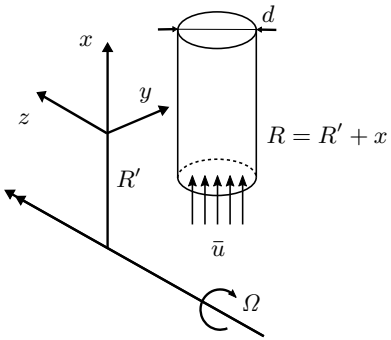

Figure B.1: Cooling channel under system rotation

Continuity Equation

$$\frac{\partial u}{\partial x} + \frac{\partial v}{\partial y} + \frac{\partial w}{\partial z} = 0 \tag{B.1}$$

Momentum Equations (Navier-Stokes Equations)

$$\rho\left(\frac{\partial u}{\partial t} + u\frac{\partial u}{\partial x} + v\frac{\partial u}{\partial y} + w\frac{\partial u}{\partial z}\right) = - \frac{\partial p}{\partial x} + \mu\Delta u \underbrace{+2\rho\Omega v}_{\text{Coriolis}} \underbrace{+ (\rho - \rho_i)\,\Omega^2 R + \rho_i \Omega^2 R}_{\text{centrifugal}} \tag{B.2}$$

$$\rho\left(\frac{\partial v}{\partial t} + u\frac{\partial v}{\partial x} + v\frac{\partial v}{\partial y} + w\frac{\partial v}{\partial z}\right) = -\frac{\partial p}{\partial y} + \mu\Delta v \underbrace{-2\rho\Omega u}_{\text{Coriolis}} \tag{B.3}$$

$$\rho\left(\frac{\partial w}{\partial t} + u\frac{\partial w}{\partial x} + v\frac{\partial w}{\partial y} + w\frac{\partial w}{\partial z}\right) = -\frac{\partial p}{\partial z} + \mu\Delta w \tag{B.4}$$

where a reference bulk density ρ_i at the inlet of the channel has been introduced into equation (B.2).

Energy Equation

$$\rho c_p \left(\frac{\partial T}{\partial t} + u \frac{\partial T}{\partial x} + v \frac{\partial T}{\partial y} + w \frac{\partial T}{\partial z} \right) = k \Delta T + \mu \Phi \tag{B.5}$$

where Φ is the dissipation term.

B.0.2 Nondimensionalization

Introducing the following dimensionless quantities into the above given set of equations yields a set of dimensionless equations (B.7) to (B.11).

$$\begin{aligned}
\tilde{x} &= \frac{x}{d}, & \tilde{y} &= \frac{y}{d}, & \tilde{z} &= \frac{z}{d} \\
\tilde{u} &= \frac{u}{\bar{u}}, & \tilde{v} &= \frac{v}{\bar{u}}, & \tilde{w} &= \frac{w}{\bar{u}} \\
\tilde{R} &= \frac{R}{d}, & \tilde{t} &= \frac{t\bar{u}}{d}, & \tilde{p} &= \frac{p}{\rho_i \bar{u}^2} \\
\Theta &= \frac{T - T_w}{T_i - T_w}, & \Gamma &= \frac{\rho - \rho_i}{\rho_w - \rho_i}
\end{aligned} \tag{B.6}$$

Here, the geometry values are normalized with the channel diameter d. The flow velocity components are scaled by the area averaged inlet velocity $\bar{u}$. Density and temperature values are scaled by their respective inlet and boundary parameters.

Dimensionless Continuity Equation

$$\frac{\partial \tilde{u}}{\partial \tilde{x}} + \frac{\partial \tilde{v}}{\partial \tilde{y}} + \frac{\partial \tilde{w}}{\partial \tilde{z}} = 0 \tag{B.7}$$

Dimensionless Momentum Equations

$$\begin{aligned}
\frac{\partial \tilde{u}}{\partial \tilde{t}} + \tilde{u} \frac{\partial \tilde{u}}{\partial \tilde{x}} + \tilde{v} \frac{\partial \tilde{u}}{\partial \tilde{y}} + \tilde{w} \frac{\partial \tilde{u}}{\partial \tilde{z}} = \\
- \frac{\partial \tilde{p}}{\partial \tilde{x}} + \frac{1}{Re} \Delta \tilde{u} + 2Ro\, \tilde{v} + Ro^2 \tilde{R} + \frac{Gr}{Re^2} \Gamma
\end{aligned} \tag{B.8}$$

$$\frac{\partial \tilde{v}}{\partial \tilde{t}} + \tilde{u}\frac{\partial \tilde{v}}{\partial \tilde{x}} + \tilde{v}\frac{\partial \tilde{v}}{\partial \tilde{y}} + \tilde{w}\frac{\partial \tilde{v}}{\partial \tilde{z}} = -\frac{\partial \tilde{p}}{\partial \tilde{y}} + \frac{1}{Re}\Delta\tilde{v} - 2Ro\,\tilde{u} \tag{B.9}$$

$$\frac{\partial \tilde{w}}{\partial \tilde{t}} + \tilde{u}\frac{\partial \tilde{w}}{\partial \tilde{x}} + \tilde{v}\frac{\partial \tilde{w}}{\partial \tilde{y}} + \tilde{w}\frac{\partial \tilde{w}}{\partial \tilde{z}} = -\frac{\partial \tilde{p}}{\partial \tilde{z}} + \frac{1}{Re}\Delta\tilde{w} \tag{B.10}$$

Dimensionless Energy Equation

$$\frac{\partial \Theta}{\partial \tilde{t}} + \tilde{u}\frac{\partial \Theta}{\partial \tilde{x}} + \tilde{v}\frac{\partial \Theta}{\partial \tilde{y}} + \tilde{w}\frac{\partial \Theta}{\partial \tilde{z}} = \frac{1}{PrRe}\Delta\Theta + \frac{Ec}{Re}\tilde{\Phi} \tag{B.11}$$

B.0.3 Dimensionless Numbers

In the above given dimensionless equations some dimensionless products emerged that can be identified as familiar dimensionless numbers.

Reynolds Number

The Reynolds number can be regarded as the ratio of inertia forces to viscous forces.

$$Re = \frac{\bar{u}d}{\nu} \tag{B.12}$$

Prandtl Number

The Prandtl number is defined as the ratio of kinematic viscosity to thermal diffusivity and can also be regarded as the ratio of the thicknesses of flow boundary layer to thermal boundary layer.

$$Pr = \frac{\nu\rho c_p}{k} = \frac{\nu}{a} \tag{B.13}$$

Rotation Number

The rotation number is the ratio of Coriolis forces to inertial forces.

$$Ro = \frac{\Omega d}{\bar{u}} \tag{B.14}$$

Grashof Number of Rotation

The Grashof number of rotation accounts for the effect of density changes.

$$Gr = \frac{\rho_w - \rho_i}{\rho_w} \frac{\Omega^2 R d^3}{\nu^2} \tag{B.15}$$

Buoyancy Number

The Grashof number of rotation appears only in combination with the square of the Reynolds number, see equation (B.8). This combination can therefore be regarded as a dimensionless number on its own, the buoyancy number. It describes the ratio of buoyancy forces to inertial forces.

$$Bo = \frac{Gr}{Re^2} = \frac{\rho_w - \rho_i}{\rho_i} \frac{\Omega^2 d^2}{\bar{u}^2} \frac{R}{d} = \frac{\rho_w - \rho_i}{\rho_i} Ro^2 \frac{R}{d} \tag{B.16}$$

Eckert Number

The Eckert number can be regarded as the ratio between the flow's kinetic energy and the boundary layer enthalpy difference. It accounts for the effect of viscous heating and appears only in the dissipation term of the energy equation.

$$Ec = \frac{\bar{u}^2}{c_p \left(T_w - T_i \right)} \tag{B.17}$$

For the current investigation the Eckert number has been neglected.

Curriculum Vitae

Name:	Christian Tobias Waidmann
Date of birth:	01.09.1979
Place of birth:	Mutlangen
Nationality:	German

Work Experience

since 06/2007 — **Institute of Aerospace Thermodynamics**
University of Stuttgart, Germany
Research Assistant

Studies

10/2000-10/2006 — **University of Stuttgart, Germany**
Aerospace Engineering (Dipl.-Ing.)
Majors: Thermodynamics, Space Systems

Internship

10/2002-03/2003 — **Rolls-Royce Deutschland Ltd & Co KG**
Dahlewitz
Subject: Secondary Air System

Education

09/1990-06/1999 — **Hans-Baldung-Gymnasium**
Schwäbisch Gmünd
Abitur